Optical Diagnostics of Colliding Laser Produced Plasmas: Towards Next Generation Plasma Light Sources

A thesis submitted for the degree of:

DOCTOR OF PHILOSOPHY

Presented To:

The School of Physical Sciences, Faculty of Science & Health,
Dublin City University

Submitted by

Colm Fallon

B. Sc. Hons.

Dublin City University

July 2013

Research Supervisor

Prof. John T Costello

Co - Supervisor

Prof. Eugene Kennedy

Declaration

I hereby certify that this material, which I now submit for assessment on the programme of study leading to the award of Doctor of Philosophy is entirely my own work, that I have exercised reasonable care to ensure that the work is original, and does not to the best of my knowledge breach any law of copyright, and has not been taken from the work of others save and to the extent that such work has been cited and acknowledged within the text of my work.

Signed: ____________________________

ID No.: 54818351

Date: ________________________

This thesis is dedicated to my family.

Acknowledgements

I would like to express the deepest appreciation to my supervisor Prof John Costello, whose round-the-clock willingness to drop everything in order to help in any way has made this work possible. He has shown patience, trust and loyalty whenever difficulties have been encountered and has provided the guidance, freedom and intellectual and financial support necessary for me to find my path in science. John is always light hearted and approachable, despite his busy schedule.

I would like to thank my co-supervisor Prof Eugene Kennedy. After any conversation with Eugene I always walk away with a better focus and understanding, and usually with the realisation that I already knew the answer I was looking for. I would also like to thank Dr Paddy Hayden, who contributed a huge amount to all areas of this work. I learnt a lot working with Paddy, who always had the time to help, and had the knowledge, understanding and patience to ensure the highest of standards were maintained at all times.

I've been fortunate enough to work with many other fine scientists during my time as a postgrad student, in particular Padraig, Nadia and Pat Yeates, each of whose individual approach to labwork helped me to find my own. Along with them, I'd like to thank other past members of the group including Caroline, John Dardis, Vincent and Jiang Xi who were always eager to pass on their knowledge. To present members Nicky and Stephen, I hope all goes well in the future. A special mention is deserved for Mossy, whom I've travelled this journey in physics with for the past nine years. I've had the pleasure of watching him develop into a top quality scientist over that time, and I wish him the best in his future career. Many other members of the physics department contributed, staff and students alike, in particular Des, Pat Wogan, Lisa and Sheila. I'd also like to thank Prof Roger Hutton, Prof Yaming Zou and Dr Martin Andersson in Fudan University for ensuring my time spent there was highly enjoyable.

Finally, I'd like to thank Martha and Ger. There were times during the writing of this thesis when I needed to pull my head out of physics and both were always great friends and listeners.

Contents

1 Fundamentals of Colliding Laser Produced Plasmas **1**

1.1 Orientation 1
1.2 Plasma Definition 2
1.3 Laser Produced Plasma Formation 4
1.3.1 Laser-Matter Interaction 4
1.3.2 Laser-Plasma Interaction 6
1.3.3 Plasma Expansion 8
1.4 Atomic Processes in Plasmas 9
1.4.1 Bound-Bound Processes 10
1.4.2 Bound-Free Processes 11
1.4.3 Free-Free Processes 13
1.4.4 Special Case Bound-Free Processes 13
1.5 Equilibrium in Plasmas 14
1.5.1 Coronal Equilibrium 15
1.5.2 Collisional Radiative Equilibrium 16
1.5.3 Local Thermodynamic Equilibrium 17
1.6 Colliding Plasma Systems 19
1.7 Summary 21

References **22**

2 Experimental Systems and Analysis Techniques **28**

2.1 Introduction 28
2.2 Experimental Systems 29
2.2.1 Plasma Generation 29
2.2.1.1 Surelite Laser Systems 29
2.2.1.2 Colliding Plasma Optical System 31
2.2.1.3 Fixed Wedge Target System 32

2.2.1.4 Reheating System . . . 33
2.2.2 Fast Imaging Setup . . . 35
2.2.3 Andor^{TM} iStar DH334T High Resolution Sensor . . . 36
2.2.4 Emission Imaging Spectroscopy Setup . . . 37
2.3 Plasma Diagnostic Techniques . . . 41
2.3.1 Line Broadening . . . 41
2.3.1.1 Natural Broadening . . . 42
2.3.1.2 Doppler Broadening . . . 42
2.3.1.3 Pressure (Stark) Broadening: Density Calculations . . . 42
2.3.2 Line Profiles: The Boltzmann Plot Method . . . 43
2.4 Programming Techniques . . . 44
2.5 Summary . . . 47

References 48

3 Target Geometrical Effects on a Stagnation Layer 50
3.1 Introduction . . . 50
3.2 Distribution of Atoms and Ions Throughout the Plume . . . 54
3.2.1 Target Geometries . . . 56
3.2.1.1 Seed Plasma Orientation . . . 56
3.2.1.2 Distance Variation . . . 58
3.2.2 Laser Pulse Energy Variation . . . 58
3.2.3 Comparison of Distribution Analysis Results . . . 60
3.3 Spatio-Temporal Electron Density Distributions . . . 61
3.3.1 Target Geometries . . . 62
3.3.1.1 Seed Plasma Orientation . . . 62
3.3.1.2 Distance Variation . . . 64
3.3.2 Laser Pulse Energy Variation . . . 65
3.4 Spatio-Temporal Excitation Temperature Distributions . . . 67
3.4.1 Target Geometries . . . 70
3.4.1.1 Seed Plasma Orientation . . . 70
3.4.1.2 Distance Variation . . . 71
3.4.2 Laser Pulse Energy Variation . . . 73
3.5 Comparison of Emission Results . . . 74
3.6 Comparison of a Stagnation Layer with a Single Seed Plasma . . . 77
3.7 Summary . . . 79

References **80**

4 Emission Characteristics of Ionic Species in a Tin Plasma **83**
4.1 Introduction . . . 83
4.2 Stagnation Layer Optimisation . . . 86
4.2.1 Optical Time of Flight Studies . . . 91
4.2.2 Spatio-Temporal Electron Density Distributions . . . 96
4.2.2.1 Electron Density Distributions as a Function of Laser Wavelength . . . 96
4.2.2.2 Electron Density Distributions as a Function of Wedge Angle . . . 98
4.2.3 Opacity . . . 100
4.3 Reheating the Stagnation Layer . . . 101
4.3.1 Reheating the Stagnation Layer generated using Differing Seed Laser Wavelengths . . . 104
4.3.2 Reheating the Stagnation Layer Generated using a Range of Target Wedge Angles . . . 109
4.3.3 Background Reductions . . . 115
4.4 Summary . . . 117

References **119**

5 Conclusions & Outlook **121**
5.1 Conclusions . . . 121
5.2 Outlook . . . 123

References **125**

List of Tables **126**

List of Figures **126**

List of Publications **135**

Nomenclature **138**

Conferences Attended **138**

Abstract

Recently prepulse techniques such as dual-pulse laser-induced breakdown spectroscopy (DP-LIBS) have emerged as commonly used analytical techniques for qualitative and quantitative elemental investigations in various research fields and disciplines such as industrial, defense and medical applications.

The performance of the DP-LIBS technique is strongly dependent on the choice of the experimental conditions. The key parameters that affect its performance are the target properties, laser wavelength, pulse duration, energy and spot-size, interpulse delay times, delay time of observations, ambient background gas pressure and geometrical setup of the optics. The DP-LIBS approach provides significant enhancement in the intensities of emission lines and their lifetimes, up to two orders of magnitude greater than conventional single pulse laser induced breakdown spectroscopy.

The aim of the work presented here is to further advance prepulse techniques, as well as other methods to control species density, with a view to optimise emission in the visible wavelength range. In particular, a new technique involving reheating the stagnation layer formed at the collision front between two (or more) colliding plasmas is explored. Spatially and temporally resolved imaging and spectroscopy of the interaction region between two colliding plasmas are employed to demonstrate for the first time that pumping of an optimised stagnation layer significantly increases the intensity emission and duration of selected spectral lines. This technique offers the promise of tunable density and tunable energy (temperature) plasmas. It will potentially increase both the lifetimes and intensities of spectral lines in

laser produced plasmas by creating relatively low density - high energy plasmas which can overcome the problem of flux loss due to opacity, which leads to the attenuation of discrete emission lines with a concomitant reduction in line contrast, signal-to-noise ratio (SNR) and signal-to-background ratio (SBR). The latter is a key parameter in determining the limit-of-detection (LOD) of the LIBS technique. Other applications of stagnation layers include the development of 'target fuel' for Extreme UltraViolet (EUV) and X-ray light sources with an especial emphasis on generating high repetition rate, preheated droplet-like targets that can compete with the current liquid drop targets. The latter suffer from clogging at the jet nozzle due to adiabatic expansion freezing. Also, unlike stagnation layers the basic parameters of the droplet fuel cannot be easily varied in the way that stagnation layers allow.

Chapter 1

Fundamentals of Colliding Laser Produced Plasmas

1.1 Orientation

Since the development of high power lasers in the 1960s, the plasmas produced by focussing a laser beam onto a solid target have been the subject of intense research [1]. This research is fuelled both by the fundamental physics interest in laser-solid/laser-plasma/plasma-plasma interactions, and also by more recent applied requirements including the quantitative elemental analysis of samples [2].

A further development in the field is the interaction of plasmas expanding into other plasmas, of which there has been renewed interest in recent years. Fundamental research in the area is active. For example, Harilal et al. [3] have studied the spatial and temporal expansion dynamics of colliding laser produced magnesium plasmas and later Atwee and Kunze [4] studied the collision of boron nitride laser-produced plasmas. Yeates et. al. [5] performed a charge resolved electrostatic study of colliding copper plasmas, Dardis [6] performed time resolved imaging and spectroscopy studies, and Ross et. al. [7] measured the plasma ion and electron temperatures of the interaction region, and compared the results with various simulations. These simulations generally use either particle-in-cell (PIC) [8] simulations for weakly interacting plasmas, or treat the system as fluids [9] for more collision dominated interactions. When plasmas collide, they do not merge and decay in a simple manner; instead the interaction can vary from interpenetration to full stagnation, i.e. a rapid deceleration of plume material at the collision plane that lies between the two plasmas.

Apart from the obvious astrophysical interest [10], colliding plasmas have been shown to have useful applications in areas such as pulsed laser deposition (PLD) [11], indirect drive inertial confinement fusion hohlraums [12], X-ray lasers [13], Extreme Ultraviolet (EUV) / X-ray sources for lithography [14], [15], microscopy and radiography [16], [17], thin film deposition, analytical spectroscopy and electron/ion beam generation [18].

A further potential application is in the quantitative elemental analysis of samples. Much work has been done to improve the sensitivity of the laser induced breakdown spectrosocopy (LIBS) technique; in particular the introduction of a second pulse to overcome the sensitivity shortcomings of the conventional single pulse technique [19]. The dual pulse (also known as double-pulse, the terms will henceforth be used interchangeably) technique offers better coupling of the laser pulse to the target and to ablated material leading to more efficient production of plasma species in an excited state, resulting in enhanced line intensities [20].

The aim of the work reported herein is to introduce an enhancement of the dual pulse technique to further increase line intensity emissions by use of the stagnation layer (SL) between two colliding plasmas as the initial plasma, or "fuel" to be reheated by a second, time synchronised laser pulse. Key initialisation parameters of the SL were studied to optimise conditions in the fuel plasma, so that coupling of the laser energy could be increased and emission intensities optimised.

1.2 Plasma Definition

Plasma is matter in a state of partial or complete ionisation. It is a gas-like assembly of electrons, ions and (usually, but not necessarily) neutral atoms with overall electrical neutrality throughout the lifetime of the plasma, i.e.

$$n_e = \sum_z n_z z \tag{1.1}$$

where n_e is the electron density and n_z is the density of ions of charge z [21]. This assembly of particles must have a "collective response" to perturbing agents in order to be defined as plasma. A collective response will occur when a perturbed charge carrier (e.g. ion) has an effect on its near neighbours which will in turn affect their near neighbours resulting in a response from a considerable number of Coulombically coupled particles. However, the strong and long-range Coulombic forces between individual charge carriers must be screened by surrounding charged particles so that a localised charge does not play a significant role ensuring that collective influences dominate. A range must be defined, and it is normally taken to be the distance beyond which the electric field of a charged particle is shielded by particles having charges of the opposite sign and is known as the Debye length λ_D

$$\lambda_D = \sqrt{\frac{\epsilon_0 k_b T}{n_e e^2}} \tag{1.2}$$

where ϵ_0 is the permitivity of free space, k_B is Boltzmann's constant, T is the plasma temperature and e is the electron charge. The "collective response" requires a substantial amount of plasma respondents, defined by the geometrical size of the plasma, i.e. the length $L \gg \lambda_D$ [21]. Furthermore there must be at least one single charged particle closer than the Debye length to every other charged particle, i.e. the number of particles within the "Debye sphere" must be greater than unity:

$$N_D = \frac{4\pi n_e}{3}\lambda_D^3 \gg 1 \tag{1.3}$$

The most important collective response of plasmas is the wavelike motions which are superimposed onto the random motions of individual particles. The electron wave plays a fundamental role in many plasma interactions (including laser-plasma interactions) and oscillates at the plasma frequency ω_p

$$\omega_p = \left(\frac{n_e e^2}{m_e \epsilon_0}\right)^{1/2} \tag{1.4}$$

where m_e is the electron mass. The plasma frequency plays a critical role in the laser-plasma interaction, which will be discussed in subsection 1.3.2.

1.3 Laser Produced Plasma Formation

Laser produced plasmas (LPPs) are formed when high intensity laser light is tightly focused onto a solid (or any other state of matter) target. The properties of the plasmas produced depend on array of factors including laser pulse duration, wavelength and energy, as well as focused spot size and pulse shape. Equally important are the properties of the target material such as target geometry, atomic weight of the constituent elements, density, surface reflectivity, conductivity, melting and boiling points. In the current context high intensity laser light is defined as laser pulses delivered in a few nanoseconds (typically $\approx 10\ ns$) with energies between 0.1 and 1 Joules focused to a spot size of diameter of $\approx 100\ \mu$m. The irradiance achieved typically lies in the range of $10^{10} - 10^{12}\ Wcm^{-2}$. The laser produced plasmas so formed typically have:

- High expansion velocities (ion velocities of $\approx 10^6 - 10^7\ cms^{-1}$).
- High temperature (electron temperature T_e up to $100\ eV$).
- High density (electron densities n_e of $\approx 10^{18} - 10^{21}\ cm^{-3}$).
- Relatively high degree of ionisation, up to 20 times ionised (depending on factors mentioned above).

The formation of these plasmas can be divided into three distinct regimes:

1. The initial interaction of laser light with the target material, causing heating, melting and evaporation.
2. The interaction of laser light with the evaporated material as well as an isothermal expansion, perpendicular to the surface of the target.
3. An expansion of the plume which can be described using various models, e.g. adiabatic or isothermal, shockwave, drag etc. [22].

1.3.1 Laser-Matter Interaction

As stated above, the properties of plasmas created by the interaction of laser light with a solid target vary with laser intensity, pulse duration, laser wavelength, focussing conditions and the material in question. Figure 1.1 shows a schematic of the interaction; the blowoff plasma produced will exhibit a high temperature and relatively low density, while the shock generated by the ablation pressure moves inward leaving material behind the shock front at a relatively low temperature and higher than solid density [23].

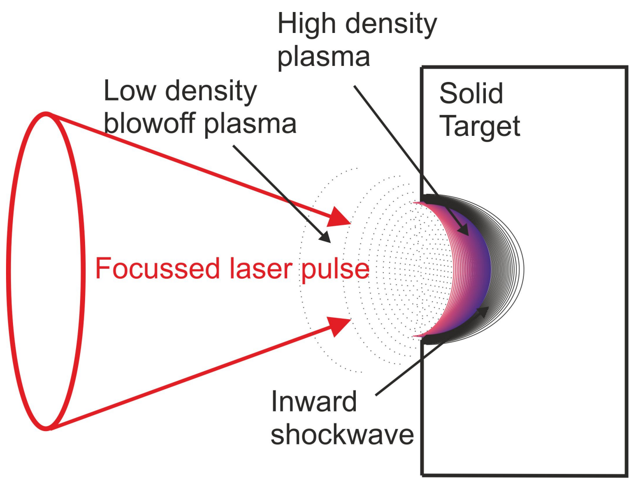

Figure 1.1: **Schematic representation of the interaction of a high power laser pulse with a solid target [23].**

The first stage of the interaction to be considered is the heating of the solid surface of the material. The phase transition of the surface from solid to liquid is important as there is a change in the refractive index of the material, which, for metals, leads to an increase in the rate of heating by the laser pulse. When the boiling point of the material is reached evaporation occurs, causing a vapour to form in front of the surface of the material. The vapour continues to grow and its density and size become sufficient to further increase the rate of absorption of the incident laser light. When evaporation occurs the ablation pressure increases, due to the recoil on the surface from the departing particles. The shock front due to this ablation pressure travels into the material compressing and heating it further. As the temperature of the material continues to increase a significant number of atoms will be ionised due to collisions, producing free electrons which increase the laser energy absorption rate, via inverse bremsstrahlung (IB, subsection 1.4.3) absorption [21]. The ablated vapour density and ablation depth remain low.

At higher pulse intensities multi-photon ionisation (MPI) of the vapour will produce seed electrons to form a weakly ionised low density plasma - it is these electrons that seed the IB process and it is IB that is then the main driver for the laser plasma formation phase discussed in the next sub-section.

1.3.2 Laser-Plasma Interaction

Once a plasma is present, the dominant form of absorption of the laser energy is by inverse bremsstrahlung within the plasma. The absorption coefficient K is given by [23]:

$$K = 2^5 e^4 \left(\frac{2c^2\pi}{k_b m_e}\right)^{3/2} \frac{z^2 n_e^2 n_c ln\Lambda}{\omega_L} \left(\omega_L^2 - \omega_p^2\right)^{-1/2} \tag{1.5}$$

where e is the charge of the electron, c is the speed of light in vacuum, k_b is Boltzmanns constant, m_e is the mass of the electron, n_c is the critical density for the laser pulse wavelength (see equation 1.10), n_e is the electron number density, z the degree of ionisation of the ions in the plasma, ω_L is the frequency of the incoming laser pulse radiation, $\ln\Lambda$ is the Coulomb logarithm (equation 1.6) and ω_p is the plasma frequency. The Coulomb logarithm is given by:

$$ln\Lambda = ln\left(\frac{\lambda_D}{\ell_{min}}\right) \tag{1.6}$$

where λ_D is the Debye length and ℓ_{min} is the minimum impact parameter (equation 1.7, or equation 1.8 if ℓ_{min} is less than the deBroglie wavelength of the electron), defined as the classical distance of closest approach between an electron and an ion. This is unitless and generally between 5 and 10 for LPPs [21].

$$\ell_{min} = \frac{k_b T_e}{Ze^2} \tag{1.7}$$

$$\ell_{min} = \frac{\hbar}{(2m_e k_b T_e)^{1/2}} \tag{1.8}$$

Electrons absorbs photons by inverse bremsstrahlung very efficiently in a plasma (especially in the infrared), even with a relatively low density of free electrons, making it difficult to effectively couple energy to the target surface [24]. However, as the plasma expands and density decreases, the laser field can once again penetrate through the plasma plume to reach the hot target surface so that further ablation occurs until the plasma again becomes the primary absorber of laser energy. The plasma continues to absorb laser light, increasing the plasma density until the plasma frequency is reached and once again the laser radiation is reflected. The plasma then expands, the density drops, the laser field can once again penetrate the plasma plume to reach the target surface and so the cycle begins again, resulting in a dynamic "self-regulation" of the ablation process.

The frequency of a laser propagating into a plasma is related to the plasma frequency by [21]:

$$\omega_L^2 = \omega_p^2 + c^2 k_p^2 \tag{1.9}$$

where ω_L and ω_p are the laser frequency and plasma frequency respectively, c is the speed of light and k_p ($= 2\pi/\lambda, \lambda =$ optical (laser) wavelength) is the laser optical propagation constant, which must be real (i.e. $\omega_L > \omega_p$) in order for the laser pulse to propagate into the plasma. When parity is reached, the value for the propagation constant becomes imaginary and the light is reflected away. An increase in density causes this limit to be reached, since $\omega_p^2 \propto n_e$ (see equation 1.4); the density limit is known as the critical density n_c. Combining equations 1.9 and 1.4 it can be seen that the critical density at which the propagation constant becomes imaginary and the wave is reflected away (i.e. shielded), is given by

$$n_c = \frac{4\pi^2 c^2 \epsilon_0 m_e}{e^2} \times \frac{1}{\lambda_L^2} \tag{1.10}$$

Looking again at the equation for the absorption coefficient K (equation 1.5) it can be seen that at low electron densities K is proportional to $\frac{1}{\omega_L^2}$. As $n_e \Rightarrow n_c$, $\omega_p \Rightarrow \omega_L$, leading to maximum absorption in the regions of the plasma where $n_e \approx n_c$. Apart from optimising the laser frequency and the density, the one other controllable parameter that can affect the absorption of laser energy is the degree of ionisation of the ions in the plasma, such that $K \propto z^2$.

1.3.3 Plasma Expansion

While the laser pulse is present, the plasma can be defined as being isothermal, i.e., the rate of thermal generation via IB and collisional excitation is greater than or equal to the rate at which heat is being lost to its surroundings (via radiative processes). During this short time period, the plume dimensions remain small and so the temperature is relatively uniform (isothermal) across the plasma. The change in dimensions of the plasma is well described by the equation for isothermal expansion [25],

$$X(t)\left(\frac{1}{t}\frac{d^2X}{dt^2}+\frac{d^2X}{dt^2}\right)=Y(t)\left(\frac{1}{t}\frac{d^2Y}{dt^2}+\frac{d^2Y}{dt^2}\right)=Z(t)\left(\frac{1}{t}\frac{d^2Z}{dt^2}+\frac{d^2Z}{dt^2}\right)=\frac{k_bT}{m} \quad (1.11)$$

where T is the plasma temperature, k_b is Boltzmanns constant, m is the mass of the particle, and X(t), Y(t) & Z(t) are the plume dimensions as a function of time. The equilibrium that pertains during this phase is described as collisional-radiative (section 1.5.2), i.e., energy gain by collisions is balanced by energy losses due to radiation.

When the laser pulse terminates, the plasma plume expands into the vacuum and cools. The plume can be described by the adiabatic expansion model of Singh and Narayan [25]. The model treats the laser-produced plasma as an ideal gas at high pressure and temperature which is initially confined to small dimensions and is suddenly allowed to expand into vacuum. The expansion velocities of the plasma are related to its initial dimensions, the initial temperature, and the atomic weight of the species and can be described by the following equation of motion [25],

$$X(t)\frac{d^2X}{dt^2}=Y(t)\frac{d^2Y}{dt^2}=Z(t)\frac{d^2Z}{dt^2}=\frac{k_bT_0}{m}\left[\frac{X_0Y_0Z_0}{X(t)Y(t)Z(t)}\right]^{\gamma}-1 \quad (1.12)$$

where X_0, Y_0, Z_0 are the initial values of X, Y and Z which are the plume dimensions at time t; T_0 is the temperature after the isothermal expansion phase and γ is the ratio of the specific heat capacities at constant pressure and constant volume, i.e. the adiabaticity parameter. The model of an adiabatic process (i.e. rapid expansion and no transfer of energy between the plasma and it's surroundings) fits nicely to the free-expansion of LPPs in vacuum. As the plasma begins to expand into vacuum the velocity of the electrons far exceeds that of the ions, due to the relative mass difference. The electrons travel at the front of the plume and begin to accelerate away from the bulk of the plasma leaving the ions behind. This causes a strong electric potential to be created between the two species fronts, a so-called ambipolar field. The Coulombic force due to the fast-electrons acting on the ions accelerate the heavy ions away from the target, while the ions tend to slow down the expansion of the electrons [26]. Plume front velocities in the order of 10^6 cm/s have been recorded [6] using initial laser and plasma parameters similar to the ones studied in this work.

1.4 Atomic Processes in Plasmas

There are various methods for the classification of atomic processes in a plasma. The major processes to be discussed in this section are listed in table 1.1 below; these are the processes which determine conditions of interest for the plasmas studied here. Note that stimulated emission is not included, since it is unlikely to occur in the plasmas of interest here, although laser plasmas are important UV and X-ray laser sources [27]. Of the twelve processes listed, six are excitation processes and the other six are their inverse de-excitation processes. They are divided into three distinct categories: bound-bound, bound-free and free-free. Each process has been further described to be either collisional or radiative, depending on the main method of energy transfer involved in the process. Each of the three classes of transitions along

Table 1.1: Classification of the main atomic processes in a laser-produced plasma ($B \rightleftharpoons B$: bound-bound, $B \rightleftharpoons F$: bound-free, and $F \rightleftharpoons F$: free-free)

Process	**Excitation**	**De-Excitation**	**Type**
$B \rightleftharpoons B$	(i) Impact Excitation	(ii) Impact De-Excitation	Collisional
$B \rightleftharpoons B$	(iii) Photoabsorption	(iv) Spontaneous Decay	Radiative
$B \rightleftharpoons F$	(v) Impact Ionisation	(vi) 3-Body Recombination	Collisional
$B \rightleftharpoons F$	(vii) Photoionisation	(viii) Radiative Recombination	Radiative
$F \rightleftharpoons F$	(ix) Bremsstrahlung	-	Collisional
$F \rightleftharpoons F$	-	(x) Inverse-Bremsstrahlung	Radiative
$B \rightleftharpoons F$	(xi) Autoionisation	(xii) Dielectronic Recombination	Special

with their relative importance will be discussed in the following sub-sections, and each of the processes will be listed and discussed individually according to their class.

1.4.1 Bound-Bound Processes

When an electron occupying a discrete energy level in an atom or ion is promoted or demoted to another discrete energy level during a collision with another electron or by the absorption or emission of a photon, the transition is known as a bound-bound process. Two of the four bound-bound processes mentioned in table 1.1 are excitations and two are de-excitations. Likewise two are collisional and two radiative.

(i) **Electron impact excitation** occurs when a free electron that moves near an ion loses energy by inducing a transition of a bound electron from a lower to a higher state. (ii) **Electron impact de-excitation** is the inverse

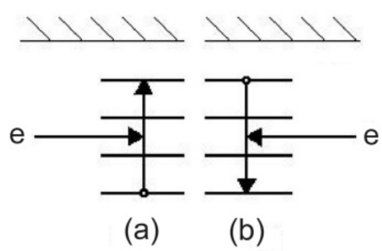

Figure 1.2: **(a) Electron impact excitation and (b) de-excitation**

of electron impact excitation. This process occurs when an electron moving near an excited ion induces a downward transition from an upper to a lower electronic state. The electron carries away the excess energy.

(iv) **Spontaneous decay** occurs when an excited ion decays to a lower (ground or excited) state, emitting a photon with energy equal to the difference in energy states. There is no interaction with any other particle or field.

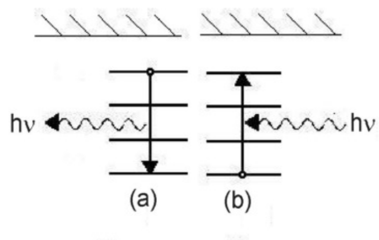

Figure 1.3: **(a) Spontaneous decay and (b) resonant photoabsorption**

(iii) **Resonant photoabsorption** is the inverse of spontaneous decay, and occurs when a photon having energy equal to the difference between two states is absorbed from the radiation field, inducing a transition from lower to higher state.

1.4.2 Bound-Free Processes

A bound-free process is said to have occurred when an ion absorbs enough energy to eject one of its bound electrons into the continuum and increment its ionisation state by one, or an electron in the continuum loses energy and falls into a discrete energy level of an ion thereby reducing its ionisation state by one. We will look at four bound-free atomic processes, three of these are collisional and three are radiative. Both autoionisation and dielectronic recombination are special cases, and will be addressed separately.

(v) **Electron impact ionisation** occurs when a free electron interacts with an ion, knocking out a bound electron into the continuum.

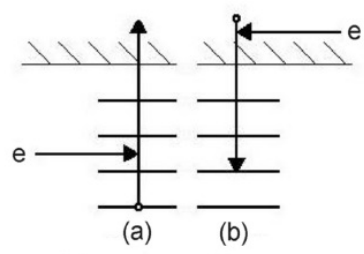

Figure 1.4: **(a) Electron impact ionisation and (b) three-body recombination**

(vi) **Three-body recombination**, also called *electron impact recombination* is the inverse of electron impact ionisation. This process occurs when two free electrons enter at the same time into the volume of an ion. One of the electrons is captured into an electronic state of the ion, and the second carries away the extra energy.

(vii) **Photoionisation** is a bound-free radiative excitation process, in which an absorbed photon moves a bound electron into the continuum, thereby ionising an atom, or increasing the ionisation state of an ion.

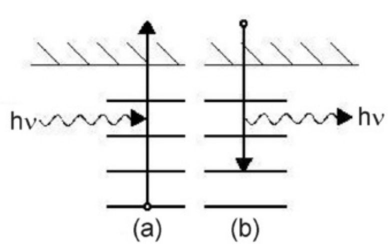

Figure 1.5: **(a) Photoionisation and (b) radiative recombination**

(viii) **Radiative Recombination** occurs when an electron is captured into an electronic state of an ion, with the extra energy emitted as a photon.

1.4.3 Free-Free Processes

There are two processes in this category; bremsstrahlung is collisional and inverse bremsstrahlung is radiative. Free-free transitions are associated with the loss or gain of energy by an electron in the field of an ion. Both are photon-electron interaction processes and are extremely important in laser-produced plasmas. Inverse-Bremsstrahlung is the most important method of plasma heating by radiation relevant to this work, and Bremsstrahlung is the main contributing factor to the continuum radiation observed in hot plasma spectra, one of the limiting factors in optimising the signal-to-background ratio (SBR) for an emission line and hence the limit-of-detection in LIBS.

(ix) **Bremsstrahlung**, which is German for braking radiation occurs when an electron in the vicinity of an ion is accelerated by the Coulomb field of the ion, emitting a photon.

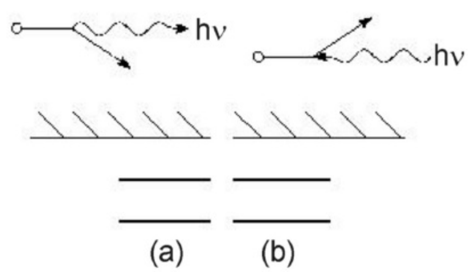

Figure 1.6: **(a) Bremsstrahlung and (b) inverse bremsstrahlung**

(ix) **Inverse bremsstrahlung**, is the inverse of the above process. An electron that moves near an ion absorbs a photon from the radiation field. Due to it's importance in laser plasmas in general and in the reheating process in particular, this process is discussed in greater detail in section 1.3.2.

1.4.4 Special Case Bound-Free Processes

The final two processes are bound-free, but are called special cases since the processes are slightly different from the other bound-free processes outlined so far. These differences will become apparent as the processes are introduced.

(xi) **Autoionisation** begins with a doubly excited ion in the initial state, in which two electrons are in excited shells. These states are formed when electrons or high energy photons are resonantly scattered by atoms or ions. These states are unstable against ionisation and so one of the electrons decays rapidly to a lower state, mostly the ground state, while the second takes its energy and is emitted into the continuum. Autoionisation can occur only if the resonant photon energy and hence the autoionising state energy is higher than the ionisation energy of the ion [28].

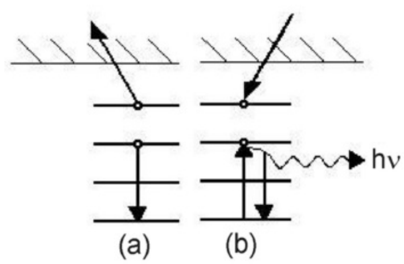

Figure 1.7: **Autoionisation (a) and (b) dielectronic recombination**

(xii) **Dielectronic Recombination** begins with the inverse of autoionisation. A free electron is captured into an ionic excited state, and the excess energy is used to promote a bound electron into an excited state, thereby resulting in a doubly excited ion. The second step in the process involves the doubly excited ion decaying either radiatively or by autoionisation, as represented in figure 1.7 above.

1.5 Equilibrium in Plasmas

A plasma can be said to be in *Complete Thermodynamic Equilibrium* (CT) if

1. The radiation intensity distribution as a function of frequency and temperature is given by the Planck formula.

2. All particles have a Maxwell velocity distribution.

3. The population distributions are given by the Boltzmann relation:

$$\frac{N_a}{N_b} = \frac{g_a}{g_b} \times exp\left(\frac{E_b - E_a}{k_b T_e}\right) \tag{1.13}$$

where N_a, N_b, g_a, g_b, E_a & E_b are the populations, statistical weights and energy levels of the states labelled a and b.

4. The ratio of ions of charge (Z) to those of charge (Z-1) is given by the Saha equation [29]. The Saha equation is given by:

$$\frac{N_z n_e}{N_{z-1}} = 2(\frac{2\pi m_e k_b T_e}{h^2})^{3/2} \times \exp\left(\frac{\chi_{z-1,a}}{k_b T_e}\right) \times \frac{g_z}{g_{z-1}} \tag{1.14}$$

where N_z and N_{z-1} are the ion stage populations, and g_z and g_{z-1} are the statistical weights associated with levels within these ion stages, and $\chi_{z-1,a}$ is the ionisation potential of the ion charge z-1 in its ground level a.

However, it is rare that a laboratory plasma approaches a state of CT equilibrium. CT requires the plasma to be *optically thick* such that radiation cannot escape from the plasma volume. The fact that most plasmas are radiating at a broad range of wavelengths means that the optically thick criterion cannot be fully met and so rigorous CT cannot be reached. Models with less stringent validity requirements have been developed, and the three most commonly used models in plasma physics are:

1. *Coronal Equilibrium* (CE)
2. *Collisional Radiative Equilibrium* (CRE)
3. *Local Thermodynamic Equilibrium* (LTE)

1.5.1 Coronal Equilibrium

Coronal equilibrium (CE) is used to describe low density ($n_e \leq 10^8 cm^{-3}$), optically thin plasmas. Most ions reside in the ground state, and collisional de-excitation can be completely ignored. The plasmas described by CE occur often in the extended low density portion of a laser produced plasma plume. Photoionisation and photoexcitation rates are very low, and hence spectroscopic techniques are not suited to these plasmas.

1.5.2 Collisional Radiative Equilibrium

Collisional radiative equilibrium is applicable to the intermediate density regime, which includes electron collision processes causing transitions between excited state levels. A Maxwellian electron velocity distribution is applied to CRE, and the plasma is assumed to be optically thin. In a LPP model developed by Colombant & Tonon [30] based on CRE theory the ionisation balance equation is given by the expression:

$$\frac{n_{z+1}}{n_z} = \frac{S(z, T_e)}{\alpha_r(z+1, T_e) + n_e \alpha_{3b}(z+1, T_e)} \tag{1.15}$$

where S(z,T$_e$) is the collisional ionisation coefficient, $\alpha_r(z+1, T_e)$ is the radiative recombination coefficient and $\alpha_{3b}(z+1, T_e)$ is the three-body recombination coefficient, each of which are functions of the charge state (z), electron temperature (T_e), ionisation potential (χ_z) and the number of open shell electrons.

The solution to this model can be determined for all charge states for a given electron density and temperature to give the ion fractions of a plasma as a function of T_e. Figure 1.8 shows the calculated ion fractions for a Sn (tin) plasma, as studied in chapter 4. A fixed electron density (n_e) was used, corresponding to 90% of the critical density (n_c) for a 1064 nm wavelength laser pulse (see equation 1.10), and the ionisation potentials were calculated using the Cowan code [15]. It can be seen at the extreme left of the graph (i.e. at low temperatures) that the fraction of neutral atoms is high, and as the temperature increases this fraction decreases sharply as the fraction of singly ionised tin increases sharply, and so on. Heavier elements initially have lower ionisation potentials, and so produce higher charge states in the plasma.
The model also relates laser pulse parameters to the electron temperature (T_e) and the average charge number (z) if high electron densities are present:

$$T_e \cong 5.2 \times 10^{-6} A^{1/5} [(\lambda^2 I(W/cm^2)]^{3/5} \tag{1.16}$$

If T_e>30 eV

$$z \cong \frac{2}{3}[zT_e]^{\frac{1}{3}} \tag{1.17}$$

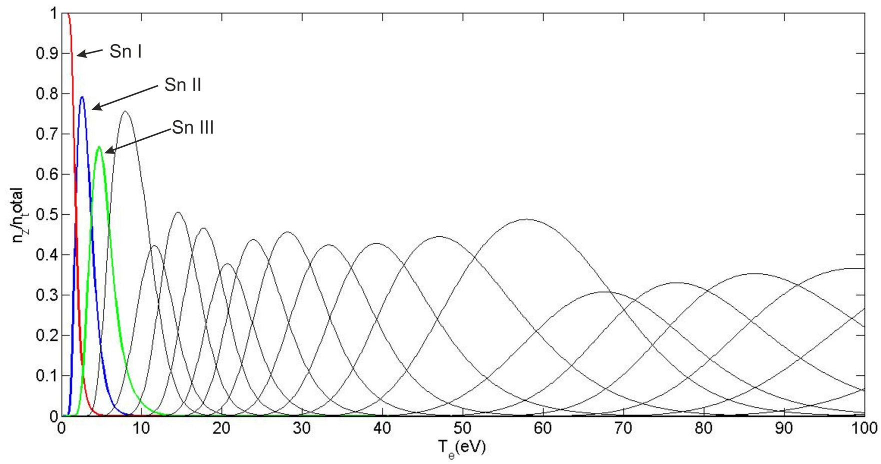

Figure 1.8: **Sn ion fractions as a function of electron temperature (T_e), using the Colombant & Tonon CR model**

where A is the atomic number of the element under consideration, λ is the incident wavelength in μm and I is the laser irradiance. The validity of the CRE model begins to fail as electron density increases, and a more general model is required.

1.5.3 Local Thermodynamic Equilibrium

Collisional processes dominate over radiative ones in a plasma in local thermodynamic equilibrium (LTE) [28], and so the plasma must have a high electron density so that the collision frequency is high. In complete thermodynamic equilibrium all particles and fields are in mutual equilibrium; however in LTE the electrons and ions are in equilibrium with each other but the photons are not. A large proportion of radiative emission occurs in comparison with photoabsorption, leading to energy losses to the surroundings. Therefore, the radiation spectrum is no longer described by Plancks Law. In order for LTE to hold, the rate of collisional processes must be much higher than the rate of radiative processes, minimising the amount of energy lost to the surroundings. All particles in LTE can be described by a Maxwellian velocity distribution, a Boltzmann population distribution within each ion stage and a Saha ionisation balance.

McWhirter [31] derived the relationship between electron temperature and electron density for which LTE is said to hold:

$$n_e \geq 1.6 \times 10^{12} T_e^{1/2} (E_b - E_a)^3 cm^{-3} \tag{1.18}$$

where E_a and E_b refer to the states of interest and are measured in electron volts.

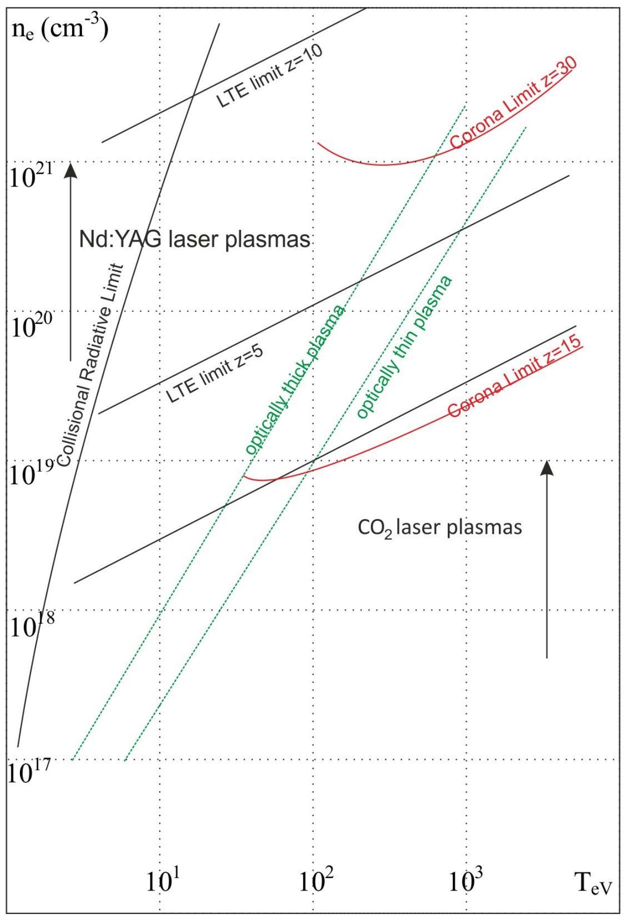

Figure 1.9: **Electron density and temperature ranges for applicability of LTE, CE and CR models** [30]

Each model and its region of validity in terms of electron densities and temperatures is displayed in figure 1.9. Approximate conditions of plasmas generated by Nd:YAG and CO_2 lasers are also illustrated here. For a Nd:YAG laser plasma the following approximations can be stated:

1. The LTE model applies to ionisation stages z<10.
2. The CE model applies for high z stages (z>30).
3. The CRE model generally applies to z stages between both of the above.

1.6 Colliding Plasma Systems

When two counter propagating laser-produced plasmas collide there are two extremes of interaction. If these so-called seed plasmas have a large relative velocity and low density at the collision plane the plasma plumes will tend to interpenetrate. On the other hand, when the relative velocities between the plasmas is small, plasma constituents will tend to decelerate abruptly at the collision plane, forming a so-called stagnation layer. As time progresses, compression of the material within the stagnation layer will yield a significant increase in the local temperature and density [6].

When there is a moderate degree of interpenetration, i.e., when the ion -ion mean-free path (MFP) is larger than the typical dimensions of the system [32] (usually taken as the separation of the seed plasma plumes), the heating process is mainly driven by the internal collisions between ions in each of the individual seed plasmas. This regime is known as soft stagnation; on the other hand, hard stagnation occurs when the ion-ion mfp is small compared to the distance between the two seed plasmas. The two plumes decelerate rapidly, little or no interpenetration occurs, and the interaction is dominated by collisions between ionic species from each of the opposing seed plasmas.

To help determine which stagnation regime to expect, the collisionality parameter [33, 34, 32]

$$\zeta = D/\lambda_{ii} \tag{1.19}$$

is used, where D is the separation between the two seed plasmas and λ_{ii} is the ion-ion mean free path (MFP) given by [34],

$$\lambda_{ii}(1 \to 2) = \frac{m_i^2 v_{12}^4}{4\pi q^4 z^4 n_i ln\Lambda_{1\to 2}} \tag{1.20}$$

where m_i is the ion mass, v_{12} is the relative plasma flow velocity, q is the elementary charge, z is the average ionisation state of the plasma, n_i is the plasma density at the collision plane and $ln\Lambda_{1\rightarrow 2}$ (see equation 1.6) is the so-called Coulomb logarithm (all in SI units). The contribution from ion-electron collisions is ignored because the ion-electron MFP is usually much larger than ion-ion MFP for medium z plasmas (due to the high dependence on charge state z), especially for laser produced plasmas (LPPs) of density $10^{16} - 10^{19}$ cm^3, as is the case in the stagnation layers of interest here [33]. Hough et. al. [35] noticed the relatively early stagnation of high densities of electrons, attributable to the effects of space-charge separation; hence the effects of electron stagnation would need to be accounted for in any more complete model of stagnation layer formation.

Early attempts to model the collision of two counter-streaming plasmas were mainly focussed on fusion codes based on the single fluid model. However, these codes do not allow for plume interpenetration and so when the two seed plasmas collided, they simply merged into a single fluid and always stagnated, resulting in the formation of excessively strong shockwaves and an unnatural temperature spike at the interface [36].

A one-dimensional multi-fluid code was developed by Rambo and Denavit [32] which could simulate both interpenetration and stagnation in colliding plasmas, and was capable of tracking the dynamics of each elemental species independently, hence the term multi-fluid. The model makes use of a particle-in-cell (PIC) [8] representation of the ions. The versatility of this particular multi-fluid code meant that Rambo and Denavit were able to simulate ion separation during the initial expansion of the seed plasmas. A computer model based on this code was developed by Doohan [37], although both electric field considerations and electron fluids were omitted. Various other approaches exist for colliding plasma simulations, e.g., one-dimensional Monte Carlo and Lagrangian multifluid codes, one- and two-dimensional hybrid (particle ions, fluid electrons) codes and single-fluid Lagrangian codes. The multifluid codes generally predict a much softer stagnation than the single fluid codes which seem to be more in line with observation [9]. Finally, the plasma computer model known as HEIGHTS [38] was recently used by Harilal [39] to simulate two colliding plasmas.

1.7 Summary

In this chapter the applications of colliding plasmas have been introduced and the basic theoretical foundations used during the remainder of this work has been discussed. The fundamental plasma processes were described as well as plasma formation and expansion due to the interaction of laser radiation with matter. Thermodynamic equilibrium models have been discussed as well as colliding plasma fundamentals.

References

[1] A. Dwivedi. Recent advances in pulsed laser ablated plasma plumes: A review. *Surface Review And Letters*, 14(1):57–69, FEB 2007. ISSN 0218-625X. doi: {10.1142/S0218625X07009074}.

[2] E. Tognoni, V. Palleschi, M. Corsi, and G. Cristoforetti. Quantitative micro-analysis by laser-induced breakdown spectroscopy: a review of the experimental approaches. *Spectrochimica Acta Part B-Atomic Spectroscopy*, 57(7):1115–1130, JUL 31 2002. ISSN 0584-8547. doi: {10.1016/S0584-8547(02)00053-8}. 1st Euro-Mediterranean Symposium on Laser-Induced Breakdown Spectroscopy, Cairo, Egypt, NOV 02-06, 2001.

[3] S.S. Harilal, C.V. Bindhu, and H.J. Kunze. Time evolution of colliding laser produced magnesium plasmas investigated using a pinhole camera. *Journal Of Applied Physics*, 89(9):4737–4740, MAY 1 2001. ISSN 0021-8979.

[4] T. Atwee and H.J. Kunze. Spectroscopic investigation of two equal colliding plasma plumes of boron nitride. *Journal Of Physics D-Applied Physics*, 35(6):524–528, MAR 21 2002. ISSN 0022-3727. doi: {10.1088/0022-3727/35/6/306}.

[5] P. Yeates, C. Fallon, E. T. Kennedy, and J. T. Costello. Charge resolved electrostatic diagnostic of colliding copper laser plasma plumes. *Physics Of Plasmas*, 18(10), OCT 2011. ISSN 1070-664X. doi: {10.1063/1.3633486}.

[6] J. Dardis and J. T. Costello. Stagnation layers at the collision front between two laser-induced plasmas: A study using time-resolved imaging and spectroscopy. *Spectrochimica Acta Part B-Atomic Spectroscopy*, 65(8, SI):627–635, AUG 2010. ISSN 0584-8547. doi: {10.1016/j.sab.2010.03.005}. 5th Euro-Mediterranean Sympsoium on Laser Induced Breakdown Spectroscopy, Rome, Italy, Sep 28-Oct 01, 2009.

[7] J. S. Ross, H-S. Park, R. Berger, L. Divol, N. L. Kugland, W. Rozmus, D. Ryutov, and S. H. Glenzer. Collisionless Coupling of Ion and

Electron Temperatures in Counterstreaming Plasma Flows. *PHYSICAL REVIEW LETTERS*, 110(14), APR 2 2013. ISSN 0031-9007. doi: {10.1103/PhysRevLett.110.145005}.

[8] M.M. Turner. Kinetic properties of particle-in-cell simulations compromised by Monte Carlo collisions. *Physics Of Plasmas*, 13(3), MAR 2006. ISSN 1070-664X. doi: {10.1063/1.2169752}.

[9] P.W. Rambo and R.J. Procassini. A Comparison Of Kinetic And Multifluid Simulations Of Laser-Produced Colliding Plasmas. *Physics Of Plasmas*, 2(8):3130–3145, AUG 1995. ISSN 1070-664X. doi: {10.1063/1.871145}.

[10] H-S. Park, D. D. Ryutov, J. S. Ross, N. L. Kugland, S. H. Glenzer, C. Plechaty, S. M. Pollaine, B. A. Remington, A. Spitkovsky, L. Gargate, G. Gregori, A. Bell, C. Murphy, Y. Sakawa, Y. Kuramitsu, T. Morita, H. Takabe, D. H. Froula, G. Fiksel, F. Miniati, M. Koenig, A. Ravasio, A. Pelka, E. Liang, N. Woolsey, C. C. Kuranz, R. P. Drake, and M. J. Grosskopf. Studying astrophysical collisionless shocks with counterstreaming plasmas from high power lasers. *High Energy Density Physics*, 8(1):38–45, MAR 2012. ISSN 1574-1818. doi: {10.1016/j.hedp.2011.11.001}.

[11] S. L. Gupta and R. K. Thareja. Photoluminescence of nanoparticles in vapor phase of colliding plasma. *Journal Of Applied Physics*, 113(14), APR 14 2013. ISSN 0021-8979. doi: {10.1063/1.4800919}.

[12] L. Masoudnia and D. Bleiner. Hohlraum target for overcoming refractive losses in plasma x-ray lasers. *Laser Physics*, 23(5), MAY 2013. ISSN 1054-660X. doi: {10.1088/1054-660X/23/5/056003}.

[13] R.W. Clark, J. Davis, A.L. Velikovich, and K.G. Whitney. X-ray lasing in colliding plasmas. *Physics Of Plasmas*, 4(10):3718–3724, OCT 1997. ISSN 1070-664X.

[14] F. Ruhl, L. Aschke, and H.J. Kunze. Selective population of the n=3 level of hydrogen-like carbon in two colliding laser-produced plasmas. *Physics Letters A*, 225(1-3):107–112, JAN 27 1997. ISSN 0375-9601.

[15] P. Hayden. *Extreme Ultraviolet Source Development Using Laser Plasmas Containing Tin*. PhD thesis, University College Dublin, (2007).

[16] J.S. Hirsch, K.D. Kavanagh, E.T. Kennedy, J.T. Costello, P. Nicolosi, and L. Poletto. Tracking ground state Ba+ ions in an expanding laser-plasma plume using time-resolved vacuum ultraviolet photoionization imaging. *Laser And Particle Beams*, 22(3):207–213, SEP 2004. ISSN 0263-0346. doi: {10.1017/S0263034604223035}. International Conference on Ultrashort High-Energy Radiation and Matter, Varenna, ITALY, OCT 07-10, 2003.

[17] M. J. Rosenberg, J. S. Ross, C. K. Li, R. P. J. Town, F. H. Seguin, J. A. Frenje, D. H. Froula, and R. D. Petrasso. Characterization of single and colliding laser-produced plasma bubbles using Thomson scattering and proton radiography. *Physical Review E*, 86(5, 2), NOV 27 2012. ISSN 1539-3755. doi: {10.1103/PhysRevE.86.056407}.

[18] J.B. Greenwood, G.F. Collins, J Pedregosa-Gutierrez, J .and McKenna, A Murphy, and JT Costello. Double ionization of atomic negative ions in an intense laser field. *Journal Of Physics B-atomic Molecular And Optical Physics*, 36(16):L235–L240, AUG 28 2003. ISSN 0953-4075. doi: {10.1088/0953-4075/36/16/101}.

[19] V. I. Babushok, F. C. DeLucia, Jr., J. L. Gottfried, C. A. Munson, and A. W. Miziolek. Double pulse laser ablation and plasma: Laser induced breakdown spectroscopy signal enhancement. *Spectrochimica Acta Part B-Atomic Spectroscopy*, 61(9):999–1014, SEP 2006. ISSN 0584-8547. doi: {10.1016/j.sab.2006.09.003}.

[20] X. Jiang, P. Hayden, R. Laasch, J. T. Costello, E. T. Kennedy. Inter-Pulse Delay Optimization in Dual-Pulse Laser Induced Breakdown Vacuum Ultraviolet Spectroscopy of a Steel Sample in Ambient Gases at Low Pressure. *Spectrochimica Acta Part B*, 2013, In Press.

[21] P.K. Carroll and E.T. Kennedy. Laser-Produced Plasmas. *Contemporary Physics*, 22(1):61–96, 1981. ISSN 0010-7514.

[22] S.S. Harilal, C.V. Bindhu, M.S. Tillack, F. Najmabadi, and A.C. Gaeris. Internal structure and expansion dynamics of laser ablation plumes into ambient gases. *Journal Of Applied Physics*, 93(5):2380–2388, MAR 1 2003. ISSN 0021-8979. doi: {10.1063/1.1544070}.

[23] S. Eliezer. *The interaction of high-power lasers with plasmas*. Series in plasma physics. Institute of Physics Publishing, Bristol, Philadelphia, 2002. ISBN 0-7503-0747-1. URL `http://opac.inria.fr/record=b1133708`.

[24] Y.F. Lu, M.H. Hong, and T.S. Low. Laser plasma interaction at an early stage of laser ablation. *Journal Of Applied Physics*, 85(5):2899–2903, MAR 1 1999. ISSN 0021-8979. doi: {10.1063/1.369054}.

[25] R.K. Singh and J. Narayan. Pulsed-laser evaporation technique for deposition of thin films: Physics and theoretical model. *Phys. Rev. B*, 41:8843–8859, May 1990. doi: 10.1103/PhysRevB.41.8843. URL `http://link.aps.org/doi/10.1103/PhysRevB.41.8843`.

[26] Y. Okano, Y. Hironaka, K.G. Nakamura, and K. Kondo. Time-resolved electron shadowgraphy for 300 ps laser ablation of a copper film. *Applied Physics Letters*, 83(8):1536–1538, AUG 25 2003. ISSN 0003-6951. doi: {10.1063/1.1604946}.

[27] H. Daido, I. Turcu, I.N. Ross, J.G. Watson, M. Steyer, R. Kaur, M.S. Sschulz, and M Amit. Spatial Coherence Of A Repetitive Laser-Plasma Point X-ray Source In The Water Window Spectral Region. *Applied Physics Letters*, 60(10):1155–1157, MAR 9 1992. ISSN 0003-6951. doi: {10.1063/1.107389}.

[28] D. Salzmann. *Atomic Physics in Hot Plasmas*. Oxford University Press, New York, 1998.

[29] M.R. Zaghloul, M.A. Bourham, and J.M. Doster. A simple formulation and solution strategy of the Saha equation for ideal and nonideal plasmas. *Journal Of Physics D-Applied Physics*, 33(8):977–984, APR 21 2000. ISSN 0022-3727. doi: {10.1088/0022-3727/33/8/314}.

[30] D. Colombant and G.F. Tonon. X-Ray-Emission in Laser-Produced Plasmas. *Journal OF Applied Physics*, 44(8):3524–3537, 1973. ISSN 0021-8979.

[31] R.H. Huddlestone and S.L. Leonard. *Plasma diagnostic techniques*. Academic Press, New York, 1965.

[32] P.W. Rambo and J. Denavit. Interpenetration And Ion Separation In Colliding Plasmas. *Physics Of Plasmas*, 1(12):4050–4060, DEC 1994. ISSN 1070-664X.

[33] C. ChenaisPopovics, P. Renaudin, O. Rancu, F. Gilleron, J.C. Gauthier, O. Larroche, O. Peyrusse, M. Dirksmoller, P. Sondhauss, T. Missalla, I. Uschmann, E. Forster, O. Renner, and E. Krousky. Kinetic to thermal energy transfer and interpenetration in the collision of laser-produced plasmas. *Physics Of Plasmas*, 4(1):190–208, JAN 1997. ISSN 1070-664X. doi: {10.1063/1.872132}.

[34] O. Rancu, P. Renaudin, C. Chenaispopovics, H. Kawagashi, JC Gauthier, M Dirksmoller, T Missala, L Uschmann, E Forster, O Larroche, O Peyrusse, O Renner, E Krousky, H Pepin, and T Shepard. Experimental-Evidence Of Interpenetration And High Ion Temperature In Colliding Plasmas. *Physical Review Letters*, 75(21):3854–3857, NOV 20 1995. ISSN 0031-9007.

[35] P. Hough, C. McLoughin, T. J. Kelly, P. Hayden, S. S. Harilal, J. P. Mosnier, and J. T. Costello. Electron and ion stagnation at the collision front between two laser produced plasmas. *Journal Of Physics D-Applied Physics*, 42(5), MAR 7 2009. ISSN 0022-3727. doi: {10.1088/0022-3727/42/5/055211}.

[36] P.W. Rambo and J. Denavit. Time-implicit Fluid Simulation Of Collisional Plasmas. *Journal Of Computational Physics*, 98(2):317–331, FEB 1992. ISSN 0021-9991. doi: {10.1016/0021-9991(92)90145-O}.

[37] B. Doohan. *A one dimensional hydrodynamic simulation of colliding quasi neutral plasma systems*. Master's thesis, Dublin City University, (2011).

[38] A. Hassanein and I. Konkashbaev. Comprehensive physical models and simulation package for plasma/material interactions during plasma instabilities. *Journal Of Nuclear Materials*, 273(3):326–333, AUG 1 1999. ISSN 0022-3115. doi: {10.1016/S0022-3115(99)00052-5}. 13th International Conference on Plasma-Surface Interactions in Controlled Fusion Devices, San Diego, California, MAY 18-22, 1998.

[39] S. S. Harilal, M. P. Polek, and A. Hassanein. Jetlike Emission From Colliding Laser-Produced Plasmas. *IEEE Transactions On Plasma Science*, 39(11, Part 1, SI):2780–2781, NOV 2011. ISSN 0093-3813. doi: {10.1109/TPS.2011.2148722}.

Chapter 2

Experimental Systems and Analysis Techniques

2.1 Introduction

Considerable demands are placed on experimental equipment in order to both generate and measure the properties of the interaction region of two colliding plasmas. Significant alterations can be made to the stagnation layer by altering one or more of the initialisation properties, categorised as follows: (i) Laser pulse properties including the wavelength, intensity, duration, and focal spot-size. (ii) Target geometry and the composite material, and (iii) ambient background.

The parameters that can be studied, the methods to measure them, and the various analysis techniques used to extract useful information from these measurements that can aid in the quantitative description of the plasma are also numerous. There is no specific plasma diagnostic to measure all parameters at all times and positions, for all possible values, and to an acceptable degree of accuracy. However, if certain theoretical assumptions are made, a plasma can be justifiably placed into the parameter space applicable to one of the thermodynamic models described in section 1.5, and properties of the plasma such as population and temperature distributions can be inferred by analysis of the results of diagnostic methods.

Electron density n_e and temperature T_e distributions are very important characteristic properties of a laser produced plasma. Electrons are by far the most active plasma constituent; they affect every aspect of the plasma's evolution, and all radiative emissions are due to atomic processes governed by changes in electron energies (as discussed in section 1.4). There are various techniques for determining both the temperatures and densities of electrons in a plasma, with emission spectroscopy being one of the most commonly used diagnostic techniques. Emission spectroscopy is non-invasive, simple and easy to use. Analysis of the resulting spectra can be used to extract density and temperature distributions, as well as information about the shape and evolution of the stagnation layer. This knowledge can be supplemented by imaging techniques in order to gain a cogent understanding of the plasma.

In this work time resolved emission imaging and spectroscopy was used to study the interaction of two laser-produced plasmas. The following two sections will deal with the experimental details required to generate these plasmas, and the principles behind the diagnostic methods to extract useful information from them.

2.2 Experimental Systems

The laboratory setup used to undertake all experiments is shown in figure 2.1. The upper part of the photograph shows the laser systems (described in sub-subsection 2.2.1.1), which create a plasma in the vacuum chamber in the centre of the photograph. The optical diagnostics setup (subsection 2.2.2 & 2.2.4) including the fast imaging camera and spectrometer with fast gated camera attached, is pictured below the vacuum chamber. The following sections explain each system and subsystem in detail.

2.2.1 Plasma Generation

2.2.1.1 Surelite Laser Systems

Two Continuum Surelite Q-switched laser systems (series I and III) were used during the course of this work. The lasing medium in each laser is a rod of crystalline yttrium aluminium garnet ($Y_2Al_{12}O_{12}$) which has been doped with neodymium ions (Nd^{3+}), leading to the abbreviation Nd:YAG. A schematic diagram representing each is shown in figure 2.2 (a).

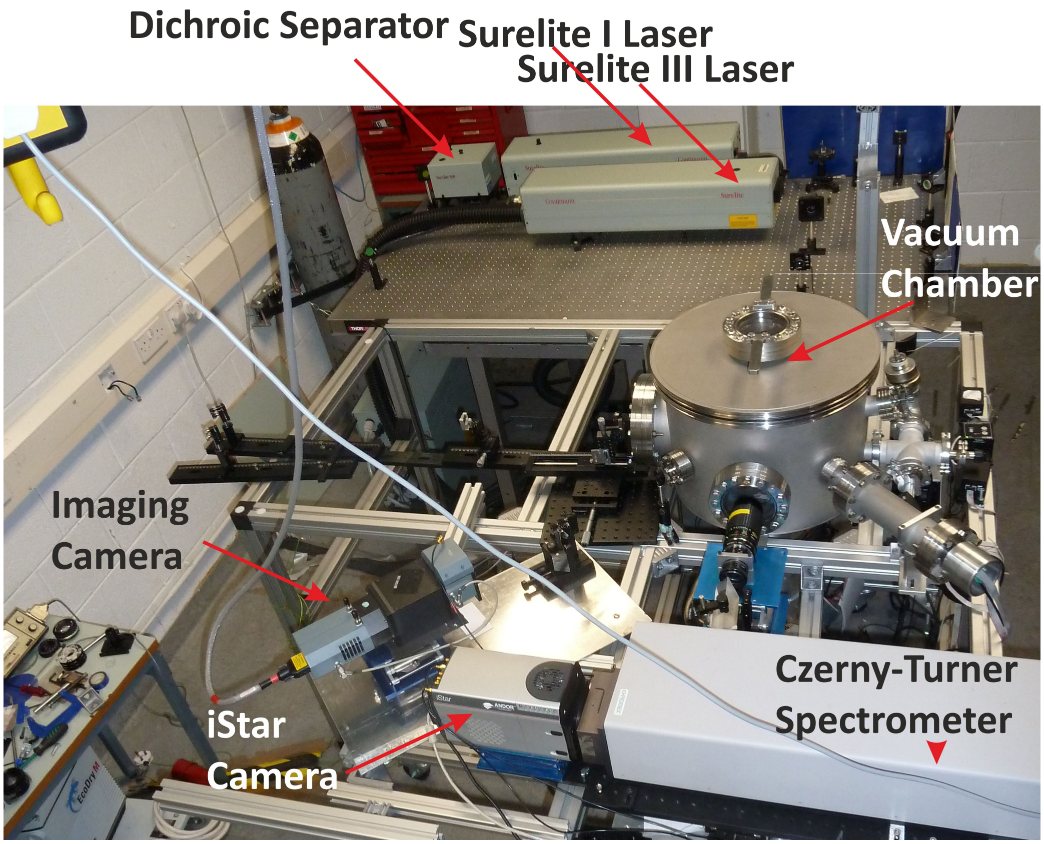

Figure 2.1: **Photograph of the experimental system used for generation and optical diagnostics of colliding plasmas.**

For the experimental studies presented in this work, the triggering of both Surelites (flashlamps and Pockels cell) was controlled using Stanford DG535 delay generators in single shot mode allowing the outputs from each laser to be synchronised with a maximum temporal jitter of 1 ns. By fitting the relevant harmonic generators, the Surelite I-10 laser could be operated at 1064 nm, 532 nm, 355 nm, and 266nm producing maximum pulse energies of 450 mJ, 220 mJ, 130 mJ and 60 mJ respectively. In the course of this work, the first and second harmonic wavelengths (1064 nm and 532 nm) were used, and maximum pulse energies were achievable. The Full Width at Half Maximum (FWHM) of the pulse obtained from the Surelite I, operating at its fundamental wavelength, was measured (figure 2.2 (b))to be 6 ns and

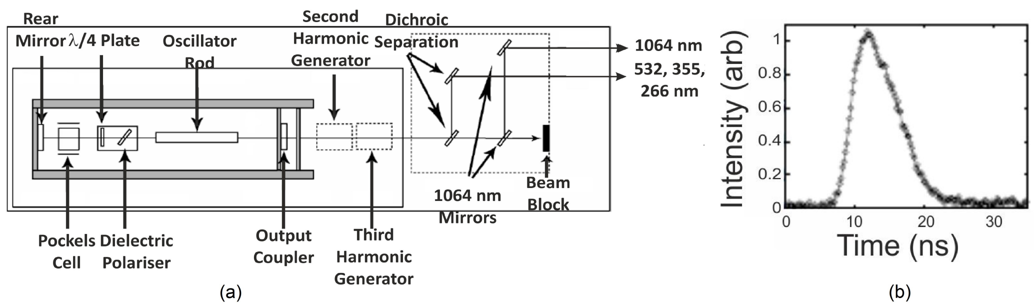

Figure 2.2: **(a) Schematic drawing of the Surelite laser system. The harmonic generating optics shown as dashed lines are absent in the Surelite III but present in the Surelite I. (b) Photodiode trace of the 1064 nm pulse output. The full width at half maximum is 6 ns.**

was ca. 2 ns shorter when operating at the second harmonic.

The Surelite III-10 laser only operated at its fundamental wavelength of 1064 nm and produced a pulse carrying an energy of 800 mJ with a FWHM of 6 ns. The output from each laser was linearly polarised with a Gaussian beam profile and a divergence of 0.6 mrad. The important characteristics of each laser have been summarised in table 2.1.

Table 2.1: Specifications of the Surelite laser systems

	Surelite I	Surelite III
Wavelength	1064, 532, 355 & 266 nm	1064 nm
Energy	450, 220, 130 & 60 mJ	800 mJ
Pulse Width (FWHM)	6 ns (4 ns for harmonics)	6 ns
Repetition Rate	10 Hz or Single Shot	10 Hz or Single Shot
External Trigger Jitter	<1 ns	<1 ns

2.2.1.2 Colliding Plasma Optical System

The optical system used to split the beam is similar to that used by Harilal *et al.* [1], a schematic of which is shown in figure 2.3. A mirror directs the laser beam towards the wedge prism, which splits the laser beam into two separate beams which are subsequently focused onto the target surface by means of a 300 mm focal length plano-convex lens. The distance between the two foci is related to the lens and wedge prism by the relation

$$d = f\gamma(n-1) \tag{2.1}$$

where n is the refractive index of the wedge prism (comprised of glass, n=1.5), γ is the acute angle of the wedge in radians, and f is the focal length of the lens. Thus a 0.5^0 wedge prism will give a separation of 1.3 mm. The spot size achieved using this setup is ≈ 100 μm giving a peak irradiance of $\approx 1 \times 10^{11}$ Wcm^{-2} on each target when using the 400 mJ output from the Surelite I laser. Using the simple collisional-radiative model of Colombant and Tonon [2], an initial temperature of ~ 20 eV is obtained for such a single laser produced plasma using a copper target.

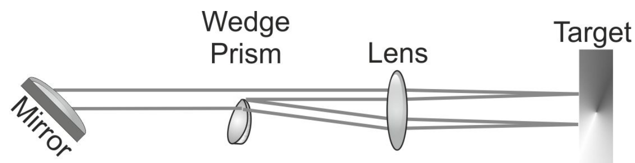

Figure 2.3: **Schematic of the optical setup for creation of two colliding plasmas.**

The colliding plasmas were generated under vacuum in the target chamber pictured in figure 2.1 using the same setup as described by Hough [3].

2.2.1.3 Fixed Wedge Target System

In order to realise a fully replenishable wedge target system a new configuration was designed and built. Two disks were cut to half the required angle (e.g. 140^0 wedge target uses two disks cut to 70^0) and pressed together to form a single cylinder with a full angle wedge (i.e. a 'V' shape) onto which the two laser beams could be focussed.
Figure 2.4 shows a picture of the target system. The cylinders were placed on an axle fixed to a rotation stage accompanied by two translation stages, required for complete alignment. By rotating the wedge a smooth target becomes available after each experimental measurement. When a full rotation has been completed, the wedges can be cut slightly deeper to remove craters and smooth the surface, or to a different angle depending on experimental requirements.

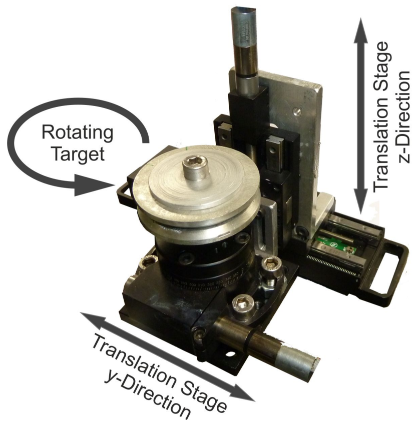

Figure 2.4: **Fixed angle wedge target system for variation of seed plasma collision angles. A disc cut to the desired angle may be loaded for over 150 separate shots on a fresh target position each time. The alignment jig provides X, Y and θ movements.**

2.2.1.4 Reheating System

Figure 2.5 shows a schematic diagram of the reheating setup, including the combination of a half-wave plate with a Brewster's window to allow the energy of the beam to be varied without affecting the pulsewidth. The half-wave plate can be rotated to change the angle of polarisation of the plane polarised light emitted from the laser system, thus varying the magnitude of the components of the electromagnetic wave. The Brewster's window only allows one component to pass through, while the orthogonal component is sent to the beam dump. Using mirrors the beam is split in two by a wedge prism which directs the lower portion of the beam downwards. Both beams are then focussed onto the target system described in sub-subsection 2.2.1.3 above. Also shown is the fast imaging system, as described in section 2.2.2.
For the case of reheating, the target wedges are split so that the reheating laser doesn't create a third seed plasma which would interfere with the experimental results. The reheating laser is focussed close to the centre of the stagnation layer (figure 2.6) using a 300 mm plano-convex lens mounted on a translation stage.
The wedge target is shifted slightly as in figure 2.7 for a number of reasons. As figure 2.5 shows, the reheat laser pulse needs to propagate along a different path to the seed laser pulse so that splitting by the wedge prism does not

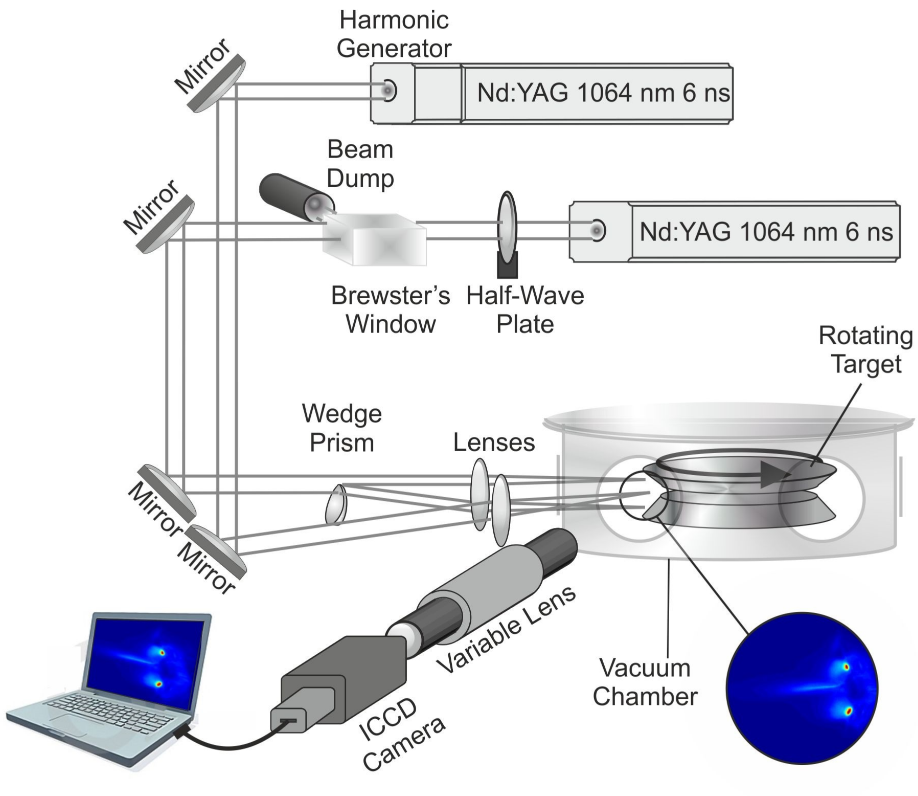

Figure 2.5: **Schematic drawing of the experimental system used for generation and reheating of colliding plasmas (not to scale).**

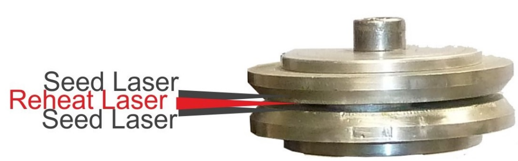

Figure 2.6: **The modified target setup to allow for propagation of the reheat laser pulse without the creation of a third seed plasma**

occur, as well as for other optical considerations, e.g. the position of the mirrors. A collinear reheating configuration is desired since maximum laser energy absorption will be achieved using this setup, i.e. the reheat pulse should propagate along the expansion direction of the stagnation layer. This is achieved by utilising the fact that the seeds and thus the stagnation layer will expand normal to the target surface, a well known property of laser-produced plasmas. By shifting the cylindrical target by the required distance, the surface angle can be changed so as to direct the stagnation layer along the axis of the reheating pulse as shown in figure 2.7.

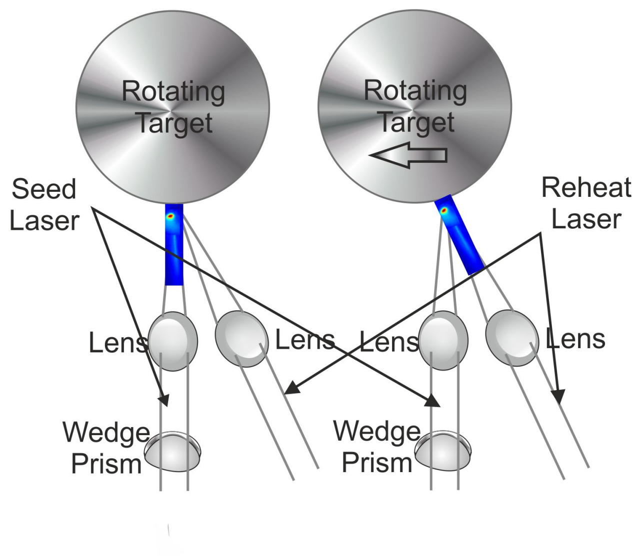

Figure 2.7: **The seed plasmas propagate normal to the target surface. If the target is shifted slightly, the plasmas will propagate towards the reheating laser, for maximum absorption.**

2.2.2 Fast Imaging Setup

Broadband imaging is a useful tool for tracking the whole plasma motion to gain an intuitive understanding of the temporal evolution of the plasma as well as for velocity calculations and for comparison with the results of single fluid codes such as Medusa [4]. The system used provides spatial and temporal resolution by using a zoom lens assembly to image the plasma onto a 2-dimensional Intensified Charge Coupled Device (ICCD) camera. The zoom lens is placed outside the vacuum chamber at a distance of $\approx$ 250mm from the plasma. In order to achieve high magnification an extension tube

(≈300 mm in length) is used to increase the distance between the zoom lens and the camera. This allows for manipulation of the distance from the lens to the image and to the object, and so variation of the magnification by modifying the ratio of image distance to object distance. The Andor DH534 model camera comprises a CCD chip with 1024 × 1024 pixels of pixel area 13 μm × 13 μm yielding an active area of 13.3 × 13.3 mm^2. The CCD chip is lens coupled (i.e. a lens is placed between the output of the image intensifier and the CCD) to the MCP which provides a minimum exposure time of 3 ns. A schematic diagram of the fast imaging setup is shown in figure 2.8. The maximum magnification provided by the system was 3.2X.

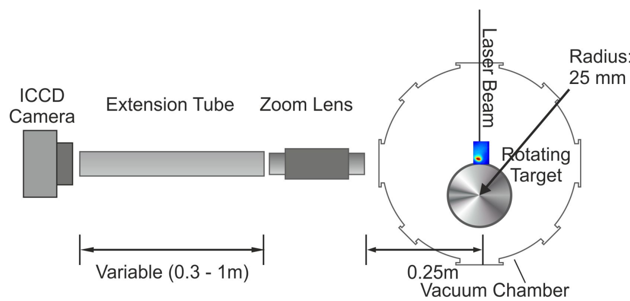

Figure 2.8: **Schematic drawing of the experimental setup for fast imaging of laser produced plasmas (not to scale).**

2.2.3 Andor^{TM} iStar DH334T High Resolution Sensor

During the course of this work there was an upgrade to the imaging system. The new iStar DH334T camera features USB connectivity, a CCD chip with 1024 × 1024 pixels of pixel size 13 μm yielding an active area of 13.3 × 13.3 mm^2, true optical shuttering of 1.2 ns and an on-board digital delay generator. The option of a second camera meant that imaging and spectroscopy could be undertaken simultaneously. The MCP is a honeycomb glass microstructure array and provides adjustable photo-electron multiplication (i.e. gain) through impact ionisation, as shown in figure 2.9.

A tungsten lamp with a stable continuous emission was used to calibrate the gain on the iStar camera. Emission from the lamp was focussed on the ICCD and the software set to full vertical binning mode. Each frame was fully vertically binned first so that the 1024 × 1024 frame was transformed

Figure 2.9: **Schematic drawing of the micro-channel plate of the iStar camera, from ref. [5].**

to a 1 $\times$ 1024 line of 1024 pixels and the readout as a 1D trace was averaged 10 times for 10 differing gain settings. A graph was plotted, as in figure 2.10. The slope of the graph (7.53×10^4) is used for gain calibrations.

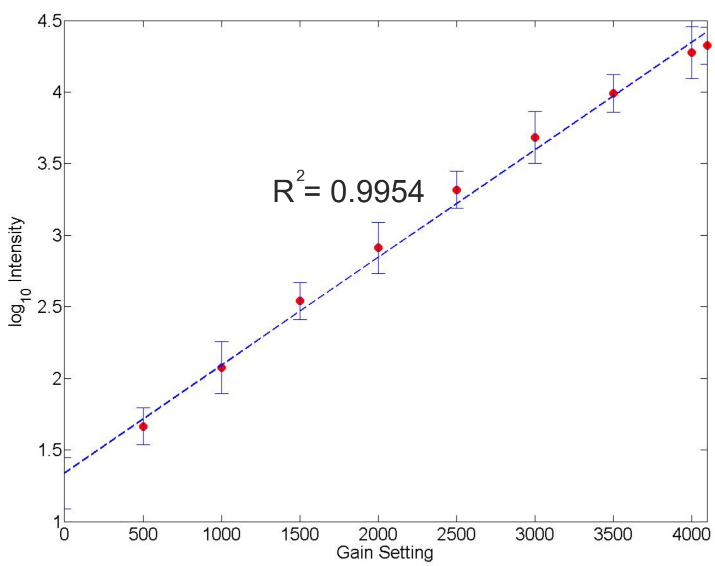

Figure 2.10: **Plot of the $\log_{10}$ of averaged intensity versus gain setting for the iStar DH334T camera.**

2.2.4 Emission Imaging Spectroscopy Setup

Optical diagnostic techniques have the advantage over other more invasive methods, e.g. wire probes, in that they do not interfere in any way with the plasma itself, and they may be used to determine electron densities and temperatures. Techniques involving lasers (such as Thomson Scattering and Interferometry) are often employed, but the ease of use of emission spectroscopy ensures that it is the most widely used method available, and is the method of choice here. An ICCD spectroscopy setup is implemented by coupling a 0.5 m Chromex visible imaging spectrometer to the Andor ICCD camera described in section 2.2.3. A schematic of the spectrometer system is shown in figure 2.11.

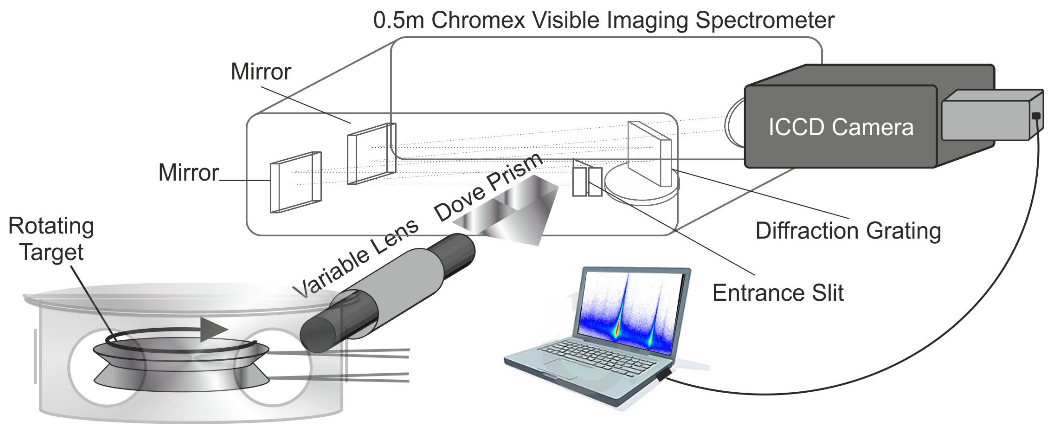

Figure 2.11: **Schematic diagram of the emission imaging spectroscopy setup including imaging optics and dove prism.**

The instrument function of the spectrometer (i.e. the measure of the intensity distribution in the output plane assuming the input to be an ideal sharp isolated spectral line) was determined using a method outlined by Kavanagh [6] using a narrow emission line from a cadmium lamp. Using a slit width of 60 μm (used for all experiments in this work), a Gaussian instrument function of 0.16 nm was determined. A colliding plasma generated in the target chamber is imaged onto the entrance slit of the spectrometer using the variable zoom lens. A dove prism is placed behind the variable lens at 45^0 in order to rotate the image of the plasma by 90^0, so that the image of the plasma expands upwards (vertically) along the length of the entrance slit of the spectrometer. A diagram of the function of the dove prism is shown in 2.12.

The optical spectrometer is a Czerny-Turner mount with toroidal focusing

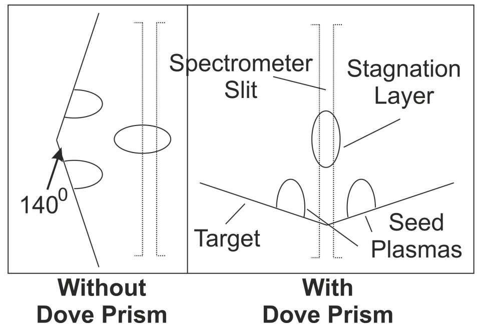

Figure 2.12: **Function of the dove prism. When the dove prism is added to the optical setup, expansion occurs along the length of the entrance slit of the spectrometer.**

mirrors enabling aberration-corrected flat field imaging. A 1200 line/mm diffraction grating with a blaze wavelength of 400 nm is used providing a resolution of 0.07 nm (FWHM) [7]. The grating efficiency in the 190 nm to 700 nm range was determined by Kavanagh and is represented in figure 2.13. The instrument function of the spectrometer was determined by Kavanagh [6]; a slit width of 60 μm giving an instrument function with an approximately Gaussian profile of width 0.16 nm is used for all experiments presented in the current study.

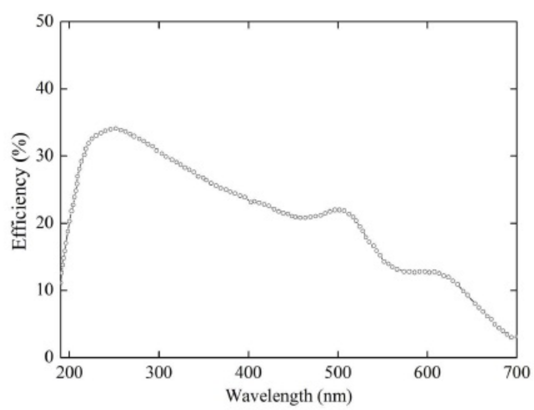

Figure 2.13: **Grating efficiency curve for the 1200 grooves mm^{-1} supplied with the Chromex visible spectrometer, from ref [6].**

Figure 2.14 shows a schematic timing diagram (not to scale) of the various trigger pulses used to synchronise the laser systems and the camera. Stanford DG535 signal generators are used in tandem with AND gates to realise the system of flashlamp and q-switch signal for each laser, along with a signal which is split in two to operate both the spectroscopic camera and the imaging camera simultaneously. Three signal generators are used, an initial "T_0" signal of 10 Hz is generated by the first generator and routed to each of the other two generators. This provides the input signal for the flashlamps in each laser, and can be delayed according to experimental requirements. The 10 Hz Q-Switch signal is time-delayed according to laser specifications (i.e. when saturation of the upper-state populations is reached), and is routed through an AND gate such that Q-switch triggering will only occur when a second signal is sent. This second signal is sent by the ICCD camera so that timing of the camera, the seed laser and the reheat laser is achievable. The gate width of the camera is set to a minimum (i.e. 1.2 ns in the case of the iStar camera) for time resolved measurements and to 10 μs for time integrated measurements.

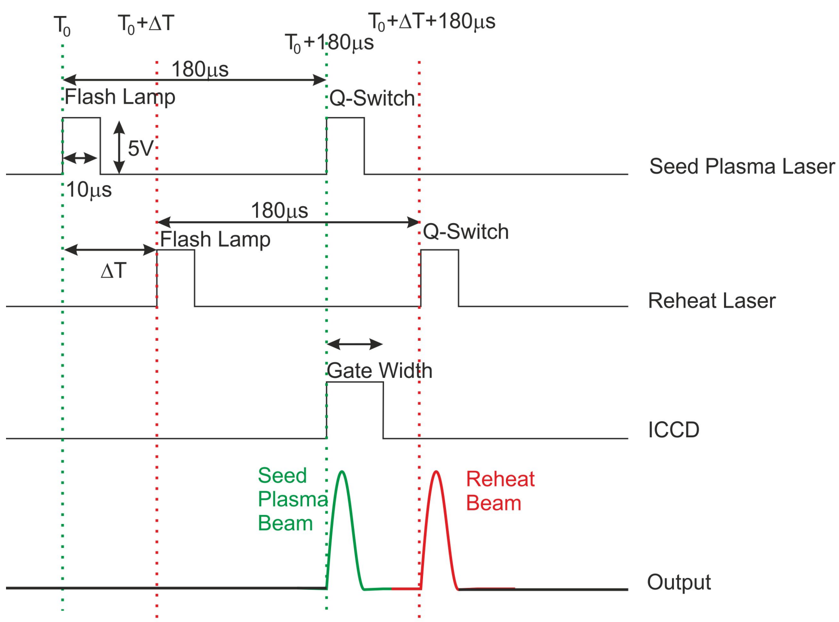

Figure 2.14: **Timing diagram showing synchronisation of the lasers and the camera for reheating experiments.**

2.3 Plasma Diagnostic Techniques

The experimental systems presented in section 2.2 describe methods to acquire spectroscopic data which can be used to diagnose plasma conditions. The work presented in this thesis required very large numbers of spectra to characterise various plasmas with a high degree of temporal and spatial resolution. Thus it was necessary that analytical codes be developed which could perform batch calculations of spectra to a high degree of accuracy. Codes were developed in the course of this work which allow relatively simple monitoring of this accuracy, and will be presented in section 2.4. First we will look at the spectroscopic methods which these codes implemented.

There are many spectroscopic theories used to relate the emission spectrum to the physical parameters of the plasma. Atoms which undergo transitions from a bound state to a lower energy state emit radiation of well defined energy and line shape. The line shape is related to the lifetime of the upper state of the transition and is also influenced by perturbations due to external influences as well as the velocity distribution of the emitting species. Thus the factors affecting the emission profiles of lines must be considered if line profiles are to be used to extract plasma parameters.

2.3.1 Line Broadening

Radiation from plasmas falls into two main categories: continuous radiation, emitted by bound-free and free-free radiative processes, and line radiation, emitted by bound-bound processes (see subsection 1.4.1). The contribution of each to a particular spectrum is dependent on many factors such as temperature, target material and integration time.

In this section we will look at the various factors affecting line profiles. There are three main broadening mechanisms: natural, pressure and Doppler broadening. Each of these mechanisms reflects a fundamental property of the emitting species, i.e. transition probability, collision frequency and thermal velocity [8].

2.3.1.1 Natural Broadening

The Heisenberg Uncertainty Principle prevents the exact determination of the lifetime and energy of a level, since the effective spreading of the quantum states in an atom leads to line broadening in the emission radiation when the upper state decays to some lower energy state. An energy level with energy E_b and lifetime t_b has an uncertainty in energy of $\Delta E_b \approx \hbar/\Delta t_b$. A photon emitted from this level to a lower level E_a will have a range of possible energies in an interval centred about $(E_b - E_a)$ of width $(\hbar/t_a + \hbar/t_b)$. This broadening due to the lifetimes of the states is referred to as natural broadening and leads to a Lorentzian intensity distribution function. Natural broadening is extremely difficult to observe because of other more significant broadening mechanisms. Also, the natural width of a line is beyond the resolution of most typical laboratory spectrometers (although not all).

2.3.1.2 Doppler Broadening

The observed wavelength of a discrete line emitted by an atom or ion can be both shifted and broadened by the Doppler effect. If the atom/ion in the plasma plume is moving towards or away from the spectrometer the line will be shifted, whereas broadening occurs due to the random motion of the emitting ions which are undergoing Brownian motion. If we can assume local thermodynamic equilibrium (LTE, see section 1.5) the velocities of the particles are described by a Maxwellian distribution with temperature T giving rise to a Gaussian line profile of full width half maximum (FWHM):

$$\Delta\lambda_{1/2} = 7.16 \times 10^{-6} \lambda_0 \sqrt{T/m} \tag{2.2}$$

where m is the atomic weight and λ_0 is the centre wavelength [9].

2.3.1.3 Pressure (Stark) Broadening: Density Calculations

Pressure broadening is caused by interactions between an emitter and surrounding particles and can be separated into three categories; the emitter interacting with the same type of atom, a different type of atom, or a charged particle. The majority of particles in a plasma are by definition charged and so it is the emitter's interaction with charged particles that we are most interested in, i.e. the process known as Stark broadening.

The two components that contribute to Stark broadening are electron-emitter collisions and ion-emitter collisions. Ion-emitter collisions occur over relatively long time scales, typically longer than that of the natural lifetime of the state, and longer than the time between ion-emitter collisions. On the other hand, electrons are much more mobile in the plasma and electron-emitter collisions take place on a very short time-scale, shorter than both the natural lifetime of the excited state, hence they are much more frequent. It is the electron collisions that make the greatest contribution to the Stark broadening of a spectral line. The half width of a Stark-broadened spectral line is given by [10]

$$\Delta\lambda_{width} = 2w\left(\frac{n_e}{10^{16}}\right) + 3.5A_i\left(\frac{n_e}{10^{16}}\right)^{\frac{1}{4}}[1 - 1.2N_D^{-\frac{1}{3}}]w\left(\frac{n_e}{10^{16}}\right) \tag{2.3}$$

where w is the electron-impact parameter, N_D is the number of particles in the Debye sphere and A_i is the ion broadening parameter [11]. The first term on the right-hand side of equation 2.3 describes the contribution due to electron-emitter collisions and the second term on the right-hand side is the ion-emitter contribution. Since Stark broadening of lines in lowly ionised species (i.e. the plasmas of interest in the current context) is dominated by electron collisions, this allows the ion broadening term to be omitted. Ion-emitter collisions effects natural lifetimes and so Stark broadening also leads to a Lorentzian intensity distribution function.

2.3.2 Line Profiles: The Boltzmann Plot Method

Under LTE conditions, the electrons and ions obey a Maxwell-Boltzmann distribution and the population of any two electronic states can be related by the Boltzmann factor

$$\frac{N_a}{N_b} = \frac{g_a}{g_b} exp\left(-\frac{E_a - E_b}{k_b T}\right) \tag{2.4}$$

where g_a and g_b are the upper and lower state degeneracies respectively, $E_a - E_b$ is the energy difference between the two states, k_b is Boltzmann's constant and T is the temperature of the plasma. Once the plasma is optically thin the integrated intensity of a line (I_{ab}) can be related to the excited state population distribution N_a and the length of the line of sight, l_{sight} by

$$I_{ab} \approx \frac{h\omega_{ba}}{8\pi^2} A_{ab} N_a l_{sight} \tag{2.5}$$

where A_{ab} is the oscillator strength of the transition, ω_{ba} is the frequency and h is Planck's constant. Relating this equation to equation (2.4) we obtain

$$\frac{I_1}{I_2} \approx \left(\frac{\omega_1 A_1 g_1}{\omega_2 A_2 g_2}\right) exp\left(-\frac{E_1 - E_2}{k_b T}\right) \tag{2.6}$$

where 1 and 2 refer to two individual spectral lines. Thus an analysis of the intensity of two experimentally observed lines can determine the temperature T_e of the plasma by rearranging equation 2.6 to give

$$k_b T = \frac{E_2 - E_1}{ln\left(\frac{\omega_2 A_2 g_2 I_1}{\omega_1 A_1 g_1 I_2}\right)} \tag{2.7}$$

It is very important to allow for the contribution of extended line wings along with continuum corrections and blending with neighbouring lines. This rarely permits temperature calculations with errors of less than 10 %. However, the accuracy can be improved to some extent by measuring the line ratio along some spectral series and plotting the logarithms of the relative intensities along with the appropriate factors as a function of the energies of the upper levels:

$$ln\left(\frac{I\lambda}{gA}\right) = -\frac{1}{k_b T}E. \tag{2.8}$$

The value of T can be deduced from the slope of this so-called Boltzmann plot.

2.4 Programming Techniques

As mentioned earlier, large scale spectra analysis can be difficult and prone to errors. Matlab^{TM} is useful for manipulation of batch files, but the fitting process can be difficult to perform. Error outputs are not always accurate, and low quality fits can occur without adequate declaration. Fityk [12] is a much more simple to use program, allowing visual monitoring of the fitting process. A mathematical model can be fitted to each curve as in figure 2.15, for example, and the parameters of the fit outputted in an easy-to-use format. To fully utilise the benefits of the Fityk program, a suite of Matlab^{TM} codes has been developed. A flowchart illustrating the operation of an example of the codes is shown in figure 2.18. The first code, "densoutput2yk", prompts the user to select a group of files to be analysed. The files are converted

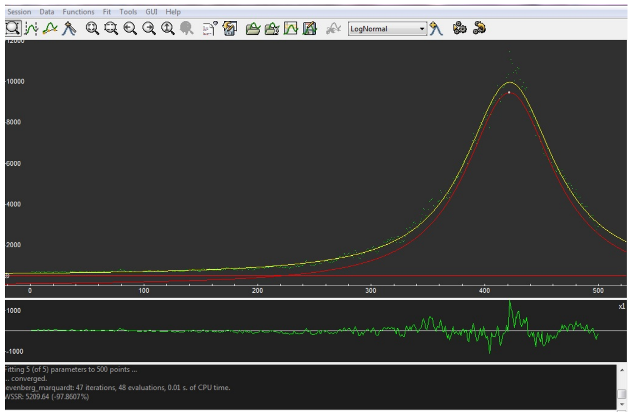

Figure 2.15: **Example of the Fityk program and it's determination of the peak of a curve.**

to spatially and spectrally resolved images, divided into spatial regions and lineouts extracted by binning the pixels. Figures 2.16 and 2.17 illustrate this process.

Each lineout is saved and it's memory address along with instructions for Fityk saved in a Fityk script file. These instructions include for example the estimate of a constant and a Voigt function fit to a particular wavelength region. Once the spectra have been divided up, the lineouts saved and the script prepared, Fityk runs the script which outputs the fit parameters to a further series of files. These multiple files are selected and read by another Matlab^{TM} code, densykoutput, which can calculate physical parameters of the plasma.

In the flowchart example, (figure 2.18), a Lorentzian profile was extracted from the spectra. This operation is performed by fitting a Voigt function. A Voigt function is the convolution of a Gaussian function and a Lorentzian function. Since spectral lines broadened by natural or Stark broadening leads to a Lorentzian shape, whereas Doppler broadening leads to a Gaussian profile, most spectral lines are best fitted by this technique. The Voigt function is given by:

$$y = a_0 \int_{-\infty}^{+\infty} \frac{exp(-t^2)}{a_3^2 + (\frac{x-a_1}{a_2} - t)^2} dt \times \left(\int_{-\infty}^{+\infty} \frac{exp(-t^2)}{a_3^2 + t^2} dt \right)^{-1} \tag{2.9}$$

where a_0 is the height, a_1 is the centre, a_2 is proportional to the Gaussian

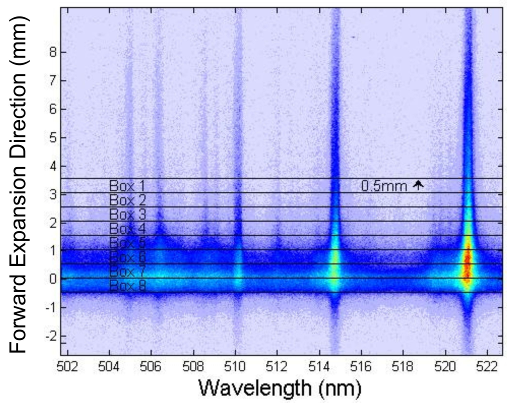

Figure 2.16: **Spectral image showing three neutral Cu transitions at 510.55nm, 515.32 & 521.82nm split into spatial regions (cf. Chapter 3).**

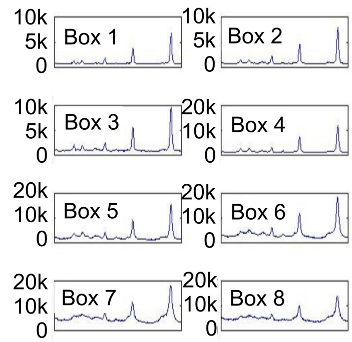

Figure 2.17: **The trace of 8 boxes from figure 2.16 after vertical binning is performed.**

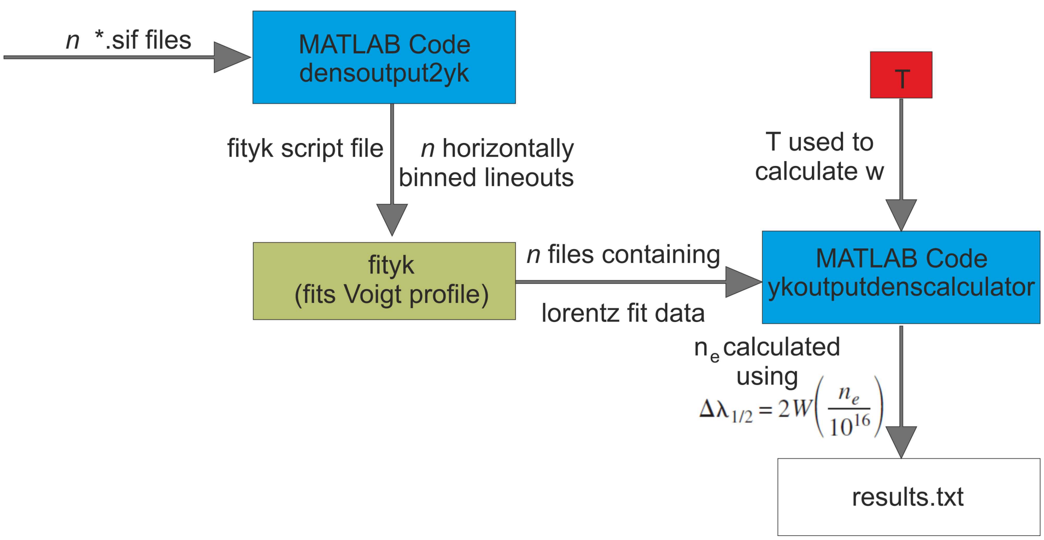

Figure 2.18: **Flowchart of the suite of codes used to fit density profiles to multiple spectra.**

width, and a_3 is proportional to the ratio of the Lorentzian and Gaussian widths. It is computed by the Fityk program according to R.J. Wells [13]. The Voigt FWHM w_V is estimated using the approximation by Olivero and

Longbothum [14]:

$$w_V = 0.5346 w_L + \sqrt{0.2169 w_L^2 + w_G^2} \tag{2.10}$$

where w_L is the Lorentzian width and w_G is the Gaussian width. In the case of temperature calculations, the suite of codes is very similar to the density codes, but for the fact that only the area under the line (i.e. the intensity of the line) is required.

2.5 Summary

In this chapter details of the apparatus used to perform experiments on colliding laser produced plasmas as well as analysis techniques to extract densities and temperatures from the resultant spectra were presented. The dual laser pulse system used for reheating stagnation layers created by a wedge target system, as well as the optical setup used to record images and spectra simultaneously were described. The suite of codes for extracting information from batch spectra was illustrated also.

References

[1] S.S. Harilal, C.V. Bindhu, and H.J. Kunze. Time evolution of colliding laser produced magnesium plasmas investigated using a pinhole camera. *Journal Of Applied Physics*, 89(9):4737–4740, MAY 1 2001. ISSN 0021-8979.

[2] D. Colombant and G.F. Tonon. X-Ray-Emission in Laser-Produced Plasmas. *Journal OF Applied Physics*, 44(8):3524–3537, 1973. ISSN 0021-8979.

[3] P. Hough. *Laser, Optical and Electrical Diagnostics of Colliding Laser-produced plasmas*. PhD thesis, Dublin City University, (2010).

[4] A. Cummings, G. O'Sullivan, P. Dunne, E. Sokell, N. Murphy, J. White, P. Hayden, P. Sheridan, M. Lysaght, and F. O'Reilly. A spatio-temporal study of variable composition laser-produced sn plasmas. *Journal of Physics D: Applied Physics*, 39(1):73, 2006. URL `http://stacks.iop.org/0022-3727/39/i=1/a=013`.

[5] "Andor iStar Brochure", 2013. URL `http://www.andor.com/pdfs/literature/Andor_iStar_ICCD_Brochure.pdf`.

[6] K. Kavanagh. *Imaging and Spectroscopy of Laser-Produced Colliding Plasmas*. PhD thesis, Dublin City University, (2006).

[7] H. Luna, K. D. Kavanagh, and J. T. Costello. Study of a colliding laser-produced plasma by analysis of time- and space-resolved image spectra. *Journal Of Applied Physics*, 101(3), FEB 1 2007. ISSN 0021-8979. doi: {10.1063/1.2431685}.

[8] K. Muraoka and M. Maeda. *Laser-aided diagnostics of plasmas and gases*. Institute of Physics Publishing, 2001.

[9] W. Lochte-Holtgreven. *Plasma Diagnostics*. AIP Press, New York, 1995.

[10] M.A. Hafez, M.A. Khedr, F.F. Elaksher, and Y.E. Gamal. Characteristics of cu plasma produced by a laser interaction with a solid target. *Plasma Sources Science and Technology*, 12(2):185, 2003. URL `http://stacks.iop.org/0963-0252/12/i=2/a=310`.

[11] A. Alonso-Medina and C. Colón. Stark broadening of sn iii spectral lines of astrophysical interest: predictions and regularities. *Monthly Notices of the Royal Astronomical Society*, pages no–no, 2011. ISSN 1365-2966. doi: 10.1111/j.1365-2966.2011.18438.x. URL `http://dx.doi.org/10.1111/j.1365-2966.2011.18438.x`.

[12] M. Wojdyr. Fityk: a general-purpose peak fitting program. *Journal Of Applied Crystallography*, 43(5):1126–1128, OCT 2010. ISSN 0021-8898. doi: {10.1107/S0021889810030499}.

[13] R.J. Wells. Rapid approximation to the Voigt/Faddeeva function and its derivatives. *Journal Of Quantitative Spectroscopy & Radiative Transfer*, 62(1):29–48, MAY 1999. ISSN 0022-4073. doi: {10.1016/S0022-4073(97)00231-8}.

[14] J.J. Olivero and R.L. Longbothum. Empirical Fits To Voigt Line-Width - Brief Review. *Journal Of Quantitative Spectroscopy & Radiative Transfer*, 17(2):233–236, 1977. ISSN 0022-4073. doi: {10.1016/0022-4073(77)90161-3}.

Chapter 3

Target Geometrical Effects on a Stagnation Layer

3.1 Introduction

In this chapter the results obtained during the study of the interaction of two counter-propagating laser-produced copper plasmas using optical imaging and spectroscopic diagnostic techniques are presented. In particular, the results of a time and space resolved optical-spectroscopic study of colliding plasmas formed on the front surfaces of inclined and partially facing Cu slab targets, as a function of the distance and of the wedge angle between them for angles ranging from 100^0 to 180^0 (i.e., laterally colliding plasmas), are reported.

The key parameters studied here are the spatial and temporal distributions of neutral species (henceforth assumed to be atoms) and singly charged ions, as well as electron temperature and density distributions within the interaction region. The aim of this work is to determine appropriate parameters for the optimisation of this system for Laser Induced Breakdown Spectroscopy (LIBS) of specific systems, especially low-Z atoms in steel [1].

The collisionality parameter of two colliding plasmas is described in subsubsection 1.6 with the relevant equations reproduced here for the reader's convenience:

$$\zeta = D/\lambda_{ii} \tag{3.1}$$

where D is the separation between the two seed plasmas and λ_{ii} is the ion-ion mean free path given by [2],

$$\lambda_{ii}(1 \rightarrow 2) = \frac{m_i^2 v_{12}^4}{4\pi q^4 z^4 n_i ln\Lambda_{1\rightarrow 2}} \tag{3.2}$$

where ϵ_0 is the permittivity of free space, m_i is the ion mass, v_{12} is the relative collision velocity, q is the elementary charge, z is the average ionisation state of the plasma, n_i is the average plasma ion density at the collision plane and $ln\Delta_{1\rightarrow 2}$ is the so-called Coulomb logarithm (all in SI units).

The collisionality parameter ϵ, relates the two factors that dictate the form the interaction will most likely take; The higher the value of the collisionality parameter, the more likely it is that stagnation will occur at the plasma-plasma interface. As equations 3.1 and 3.2 show, the collisionality of a two-plasma system is highly dependent on v_{12}, the relative velocity of the colliding seed plasmas and to a lesser extent on D, the separation between the two seed plasmas. Therefore, an experiment may be engineered in such a way as to control the collisionality of the system by changing either (i) the orientation (and thus the relative velocity) of the seed plasmas with respect to each other, (ii) the laser power density on each target face, (iii) the distance between the two seed plasmas, or (iv) a combination of the above.

Here we present a study of the stagnation layers formed when two plasmas collide by varying initial parameters to study their effect on the formation of the interaction between the two plasma plumes. Results will be compared from data obtained using (i) different laser pulse energies, (ii) a range of target wedge angles (i.e. the orientation), & (iii) varying distances between the seed plasmas.

The Surelite laser system (discussed in section 2.2.1.1) was used to generate pulses with a wavelength of 1064 nm and duration of 6 ns. The laser beam was split into two parts using a wedge prism (section 2.2.1.2) prior to being focussed to two spots of $\sim 100\mu$m diameter. The intensity ratio of the two resulting laser beams was $\sim$ 1:1 leading to an on-target irradiance of the order of $\sim 10^{11}$ W/cm^2 (depending on the energy per pulse). Figure 3.1 shows time-integrated (i.e. 10 μs, most emissions occur in the first μs) optical images of the stagnation layer created using slab targets with wedge angle between them of (a) 180^0, (b) 140^0, & (c) 100^0, each with a seed plasma separation of D = 1.3 mm.

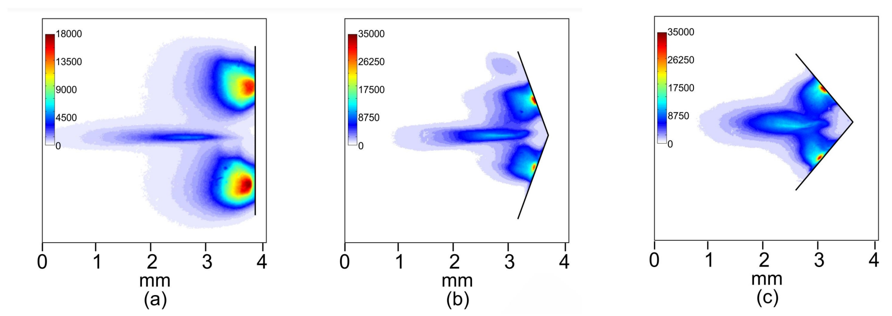

Figure 3.1: **Time integrated ($10\mu s$) images of the stagnation layer formed using 3 separate wedge angles: (a)** 180^0 **(b)** 140^0 & **(c)** 100^0**.**

Figure 3.1 (a) shows the emission image obtained by colliding seed plasmas created on laterally facing (i.e. parallel) targets, i.e. on a 180^0 target wedge angle or the flat configuration. As the two seed plasmas expand, they collide at relatively low velocities along the lateral expansion plane (parallel to the target surface). By employing a 140^0 wedge-shaped target (figure 3.1 (b)) the two seed plasmas now collide with a larger component of their forward expansion velocity. The relative collision velocity is higher, and the ion-ion mean free path (MFP) becomes larger, resulting in a higher degree of plume interpenetration. Figure 3.1 (c) shows the case where the wedge angle is decreased to 100^0; the degree of plume interpenetration is increased further here. The shape of the stagnation layer illustrates the degree of interpenetration in each case, where hard stagnation creates tight and well defined stagnation layers as in figure 3.1.

Time-resolved optical emission imaging and spectroscopy of colliding plasmas have previously [3, 4] been used to obtain information about the evolution of a plasma over time, and the plume front position has been tracked as a function of time delay [5, 6]. Here we trace the point of maximum intensity of the atoms and singly charged emitting ions as a function of time by analysis of time resolved spectra as described in section 3.2 below.

Two important characteristic properties of a laser produced plasma are its electron density n_e and temperature T_e. Electrons are by far the most active plasma constituents; they affect every aspect of the plasmas evolution, and all radiative emissions are due to atomic processes governed by changes in electron energies (as discussed in section 1.4).

To extract electron densities and temperatures, emission spectroscopy is commonly used as it is non-invasive, relatively easy to set up and use and it provides unique insights into the structure and dynamics of the plasma itself and its atomic and ionic constituents. Using space and time-resolved spectroscopy one can measure and analyse the spectra to extract space and time-resolved density and temperature distributions. To determine the temperature distributions of a copper plasma in local thermodynamic equilibrium (LTE) the Boltzmann plot method (section 2.3.2) is used, and the density distributions are determined using Stark broadening comparisons (section 2.3.1.3).

The temperature of a laser-produced plasma can be directly related to the laser power density using the collisional radiative model by Colombant & Tonon [7], (subsection 1.5.2, reproduced here for convenience) to obtain

$$T_e \cong 5.2 \times 10^{-6} A^{1/5} [(\lambda^2 I(W/cm^2)]^{3/5} \tag{3.3}$$

where A is the atomic number of the element under consideration (in this case copper), λ is the incident wavelength in μm and I is the laser irradiance, which is proportional to the laser energy. Therefore the temperature of a LPP scales as (laser power density)$^{0.6}$, which will duly have an effect on the temperature of the stagnation layer, although other heating processes such as the internal collisions between ionic species themselves in each of the individual seed plasmas will occur.

3.2 Distribution of Atoms and Ions Throughout the Plume

Fast gated emission imaging is a simple and effective way to determine the spatial distributions and expansion velocities of selected plume species. It has been used in combination with spectral filters to exclude the spectral signatures of all but one atomic or molecular species [5]; however such highly selective filters which can discriminate between species emitting in close spectral proximity are not always available. In such cases, spatially resolved high resolution optical spectroscopic techniques make it possible to track the forward expansion velocities of individual ion stages emitting throughout the lifecycle of the plasma. This technique, which can be implemented with a stigmatic spectrometer [8] is used here.

Shown in figure 3.2 below is an example of a space resolved spectrum of the stagnation layer of two colliding copper plasmas centred at λ =515 nm. The image provides space resolution in one dimension (1D) along the plasma expansion axis. The width of the slit, combined with the magnification of the optics used to image the plume or stagnation layer onto the slit, determine the lateral width of the slice of plasma plume normal to the plasma expansion axis that is integrated over the 60μm slit width (cf. Experimental details in Chapter 2). So, in principle the plume can be sampled laterally by its translation across the entrance slit of the spectrometer and a time resolved 2D mosaic image constructed. There are many distinct transition lines shown in this spectral window, including the Cu I line at 521.82 nm $[4d\,^2\mathbf{D}_{5/2} - 4p\,^2\mathbf{P}_{3/2}]$ and the Cu II line at 508.83 nm $[4f\,^3\mathbf{F}^0_3 - 4d\,^3\mathbf{D}_2]$.
By following the maximum point of the intensity of the emitting atoms and ions, taken to be the brightest part of each emission line (assuming no opacity loss), it is possible to trace the movement of each specie throughout the plume. This is achieved by recording and plotting the intensity at each point along the forward expansion direction of each spectral line to yield a curve showing the peak of intensity of the atoms & ions along the plume. Using time resolved spectra each curve can be followed to determine the movement of the emitting atoms/ions within the plume as a function of time. Figures 3.3 and 3.4 show examples of these plots, obtained by analysis of the Cu I line at 521.82nm and the Cu II line at 508.83nm respectively, revealing the differing movements of each atomic/ionic fluid.

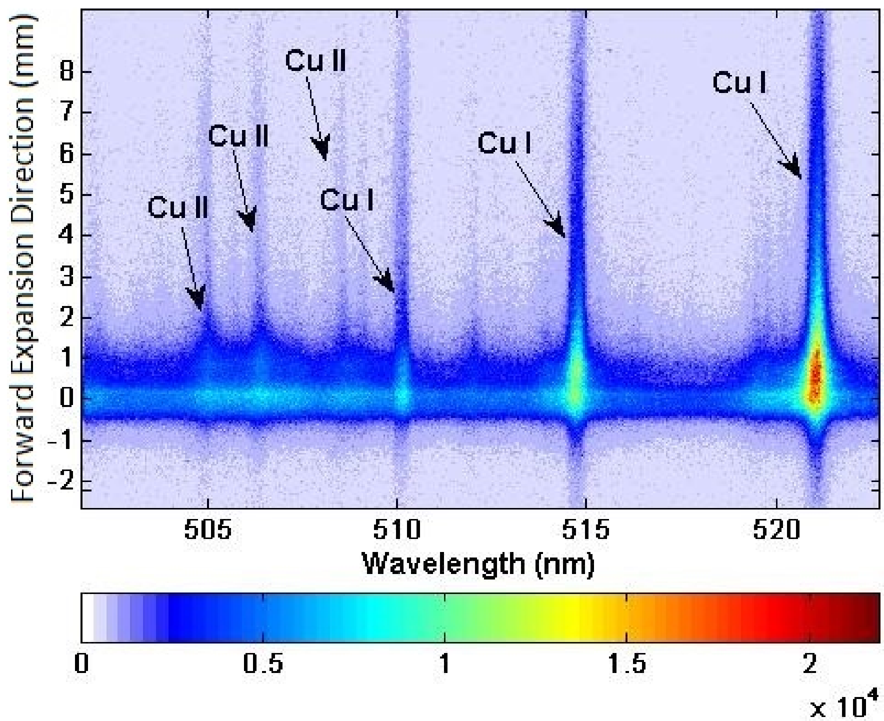

Figure 3.2: **Example time-integrated spectroscopic image of the stagnation layer generated by focussing two 105 mJ 6 ns laser pulses onto the 140^0 wedge system at a distance of D = 1.3 mm, in the wavelength region 502 nm-522 nm.**

In order to measure the movement of the atoms/ions within the stagnation layer, a mathematical model is fitted to each curve using *Fityk* [9], and the peak position of this model fit recorded and traced.

This peak position represents the point of maximum intensity of the atoms and ions emitting in the transitions mentioned above. Below we show that these peak positions are significantly dependent on the target configurations. It is very important to exercise caution when interpreting the intensities recorded in this work; these distributions do not necessarily reflect the plasma density or temperature profiles. Such analyses are carried out in sections 3.3 and 3.4.

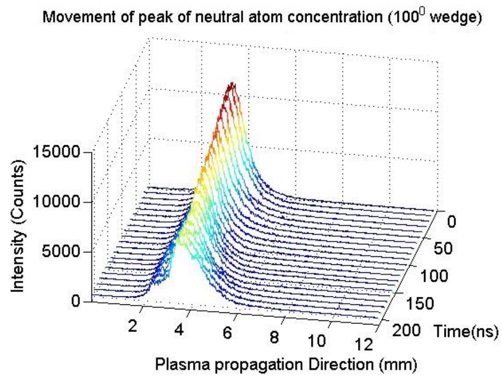

Figure 3.3: **Motion of the peak intensity point of atomic copper (λ = 521 nm) in the stagnation layer.**

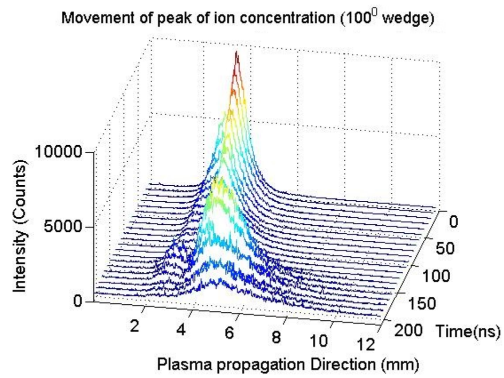

Figure 3.4: **Motion of the peak intensity point of singly charged copper (λ = 508 nm) in the stagnation layer.**

3.2.1 Target Geometries

3.2.1.1 Seed Plasma Orientation

As described above, the point of maximum intensity of the atoms and ions emitting in the transitions mentioned is traced as a function of time. The results in figure 3.5 below show these traces for three separate wedge angles (100^0, 140^0 & 180^0) at a seed distance of D = 1.3 mm for both neutral atoms and singly charged ions. Shown also is a linear fit to each data set. At later times the data seems to stray slightly from a linear approximation, due in part to insufficient signal at these times which can skew the data set. A deviation from the linear approximation can be seen to occur earlier for the case of the 180^0 wedge target as compared to the other two cases, since the signal weakens as the wedge angle opens. The goodness of fit at earlier times (i.e. $\leq$ 150 ns) demonstrates that both the atoms and ions move with constant, but respectively different, velocity.

A quick comparison of both graphs reveals that the ions move at a significantly higher velocity relative to the atoms (see table 3.1 below). It can be seen that the ratio of ion velocity to atom velocity does not vary linearly with wedge angle, which is due to more than one mechanism being involved in stagnation layer growth. The expansion velocity of electrons from the seed plumes far exceeds that of the heavier ions [10]. This leads to the generation of a strong electric field caused by the steep spatial distribution of charged particles as the electrons try to separate from the ions. The electric field

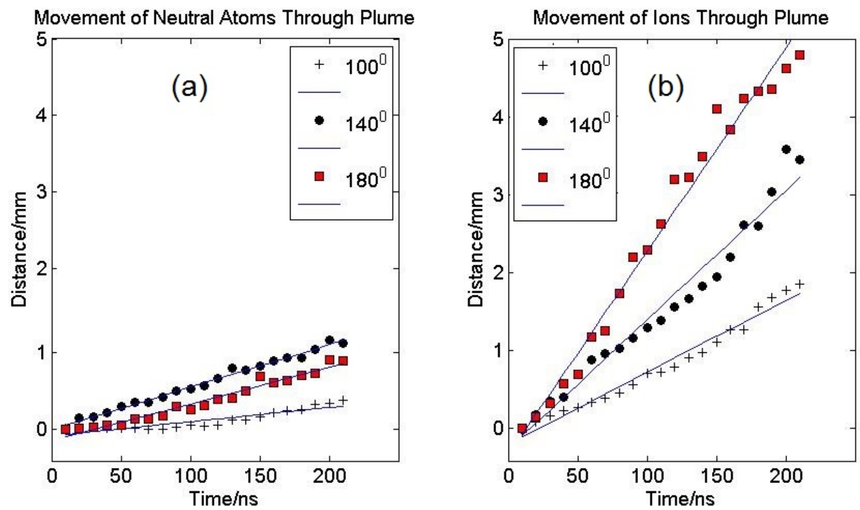

Figure 3.5: **Comparison of the movement of the peak of intensity of neutral emitting atoms and ions in a stagnation layer generated by focussing two 105 mJ 6 ns laser pulses onto three different wedge systems.**

slows the electrons while accelerating the ions, and has little effect on the neutral atoms. The plasma constituents arriving in this manner contribute to the velocity of the peaks of concentration of the stagnation layer, as does the thrust of the layer due to internal collisions, whose orthogonal component are generally in this direction.

In summary the overall stagnation layer growth depends on relative seed plasma plume velocities while the growth rate of each atomic or ionic 'fluid' within the stagnation layer depends on the expansion rate of that fluid in each seed. For any one wedge angle the atom and ion growth rates are different and hence fluid growth rates in the stagnation layer will be different (as will the initial spatial distribution for each as the layer grows). Also, the relative velocity of atoms and the relative velocity of ions will vary with wedge angle, and the difference in velocity between atoms and ions will vary with wedge angle.

The growth rates can be seen to vary as a function of the wedge angle used to generate the stagnation layers. The emitting atoms move at a very low velocity in each case, with the atoms from the 100^0 wedge moving most slowly. The stagnation layer in this case is highly confined allowing for little movement of the neutral species. The growth rate of neutral species in the stagnation layer of the 180^0 wedge are lower than from the 140^0 wedge, an observation that is, at first sight, seemingly counter-intuitive. However, it must be noted that these graphs show the peak of the emission intensity of neutral species, and not the actual concentration values. The number and density of atoms is higher in the case of the 140^0 wedge, and the peak intensity growth rates must be visualised in this context.

In the case of the emitting ions the geometrical effects of the target configuration play a much more pronounced role. The ions are accelerated by the aforementioned electric field, the distribution of which is highly dependent on the target geometry. The ions are more confined and their emission yields are higher as the target wedge angle is decreased.

3.2.1.2 Distance Variation

We present the results of experiments undertaken with a further variation of the target geometry. The distance between the two seed plasmas was varied by changing the wedge prism in the optical setup (section 2.2.1.2). Using the same experimental conditions used in the previous sections, i.e. a target wedge of 140^0 and a pulse energy of 210 mJ, seed distances of D = 1.3 mm and D = 2.6 mm were used. A comparison of the peak movements of both as in figure 3.6 shows that the time evolution of atomic and ionic species in the stagnation layer from shorter distance seeds is, as one might expect, faster.

3.2.2 Laser Pulse Energy Variation

We examine the results obtained using the same experimental conditions used in the previous section except for the fact that the target wedge angle is held constant at 100^0 and the laser pulse energies are varied. The output from the Surelite laser was set to 110 mJ, 160 mJ, and 210 mJ in a 6 ns pulse at 1064 nm (laser fluence $350J/cm^2$, $510J/cm^2$ & $670J/cm^2$ respectively, and split equally between each plasma plume, a distance of D = 1.3 mm apart with a spot-size of $\sim 100\ \mu$m diameter. The results are shown in figure 3.7.

The longitudinal growth rate of the neutral atomic copper component of

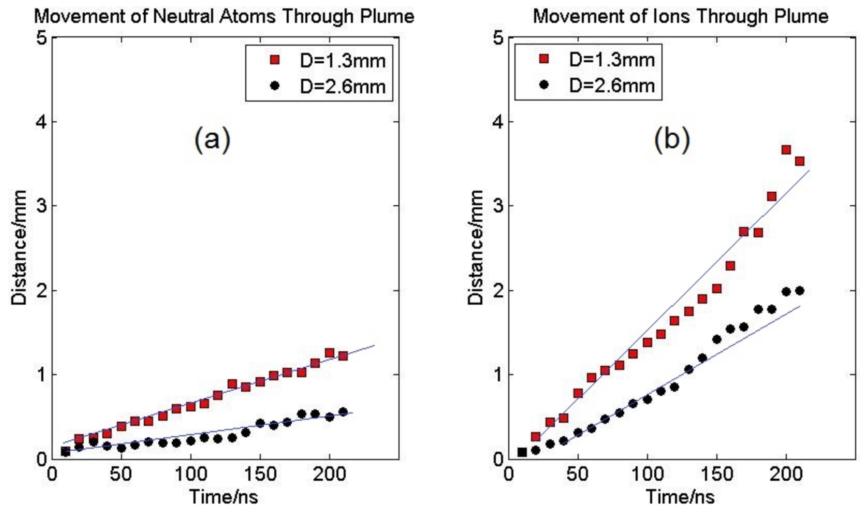

Figure 3.6: **Comparison of the movement of the peak of intensity of neutral emitting atoms and ions in a stagnation layer generated by focussing two 105 mJ 6 ns laser pulses at a distance of 1.3 mm & 2.6 mm apart.**

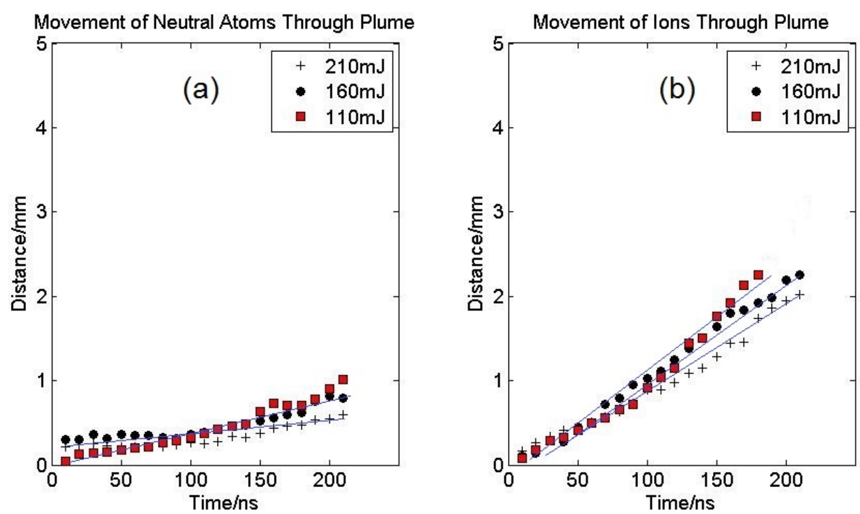

Figure 3.7: **Comparison of the movement of the peak of intensity of neutral emitting atoms and singly charged copper ions in a stagnation layer generated by focussing two 6 ns laser pulses of three distinct energies.**

the stagnation layer is again linear and relatively low in comparison to the movement of emitting singly charged ions, and does not vary much with laser energy (although the intensity of each line does increase with pulse energy). The peaks of the intensity of emitting singly charged ions also move along the stagnation layer linearly with time, implying a rather constant velocity, and there is little variation with laser pulse energy.

3.2.3 Comparison of Distribution Analysis Results

Spatially and temporally resolved imaging spectra have been used to study the movements of neutral emitting atoms and ions in the interaction region of counter-propagating laser-produced Cu plasmas for a range of target geometries, as well as for varied laser energies. In each case it was found that the movement per unit time is linear and so are recorded as velocities, and presented in table 3.1 below.

Table 3.1: Velocity* of peak of intensity of neutral emitting atoms and ions.

Target Geometry	neutrals/(cm/s)	ions/(cm/s)	ion/neutral ratio
1.3 mm, 210 mJ, 180^0 Wedge	4.8×10^5	26.1×10^5	5.4
1.3 mm, 210 mJ, 140^0 Wedge	5.5×10^5	16.6×10^5	3.0
1.3 mm, 210 mJ, 100^0 Wedge	1.9×10^5	9.2×10^5	4.8
1.3 mm, 160 mJ, 100^0 Wedge	2.4×10^5	11.3×10^5	4.7
1.3 mm, 110 mJ, 100^0 Wedge	4.4×10^5	14.5×10^5	3.3
2.6 mm, 210 mJ, 140^0 Wedge	2.3×10^5	10.4×10^5	4.5

* *Velocity here does not mean expansion rate in the normal sense of plasma plume expansion. Rather it refers to the propagation of the peak intensity value along the stagnation layer as material from the seed plasma plumes reaches the collision plane at a delay determined by the distance to be travelled and the concomitant times-of-flight.*

The seeds in the 180^0 wedge target experiment supply the interaction region with plasma species with a relatively higher velocity component parallel to the target surface compared to the 'velocity' component normal to the surface (see Dardis et. al. [5]), resulting in growth rates that are lower than those of the 140^0 wedge target setup, all else being equal. However, the brightness (not shown here) of the spectral lines analysed in the 140^0 case is higher. The growth rates in the 2.6 mm, 210 mJ, 140^0 case are also lower, but again the brightness is much lower. The 1.3 mm, 210 mJ, 100^0 wedge geometric setup demonstrates the highest brightness of the spectral lines analysed, and has relatively low growth rates of both plasma species. The brightness of spectral lines in all wavelength regions can be predicted to a higher degree of accuracy when the temperature and electron density of the plasma is known, and when used in conjunction with atomic calculations. The analysis of the copper plasma spectra to obtain the space- and time resolved electron densities and temperatures of the plasma is discussed in the following sections.

3.3 Spatio-Temporal Electron Density Distributions

The electron number densities have been determined from the line profiles of the isolated neutral copper lines at 521.83 nm using the technique described in section 2.3.1.3. The Stark contribution to the line broadening is described by the Lorentzian component of a Voigt fit (using Fityk [9]) and all other contributions, such as the Doppler effect (≈ 0.005 nm for a plasma temperature of 1 eV) and the instrument function of ≈ 0.22 nm (section 2.2.4) were accounted for in the Gaussian component of the Voigt profile [11, 12]. The full width at half maximum of the Lorentzian component of the line is used to estimate the electron number density using the simple linear equation:

$$\Delta\lambda_{1/2} = 2\omega(n_e/10^{16}) \tag{3.4}$$

The value of ω (the electron-impact parameter) obtained from the literature [13], is for a plasma of temperature 10,000K. It is known that this is a reasonable temperature for the plasmas [3] and the same literature shows that it does not vary much with temperature.

To ensure a sufficiently high signal to background ratio, the shutter of the micro-channel plate (MCP) intensifier coupled to the camera is opened for 100ns, at 5 different temporal delays. Figure 3.8 shows a spectroscopic image taken 100 ns after plasma initiation. Partial vertical binning of the image has been performed on the image, specifically for the eight boxes that have been drawn on the image in figure 3.9 to improve the signal-to-noise ratio (SNR) of the image for illustrative purposes only. For the analysis the contents of the eight boxes labelled Box 1 - Box 8 (containing 42 rows of pixels corresponding to half a millimeter each) have been summed and plotted in the graphs to the right of the image labelled Box 1 - Box 8.

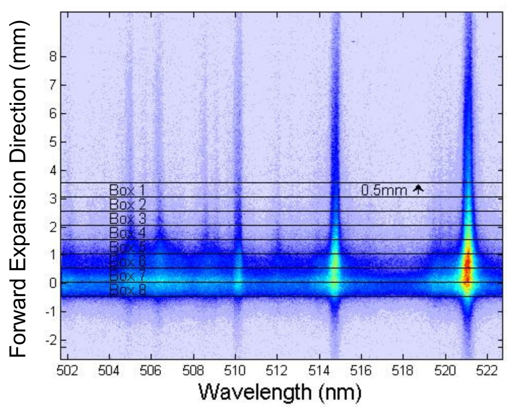

Figure 3.8: **Spectral image showing the three neutral Cu transitions at 510.55nm, 515.32 & 521.82nm.**

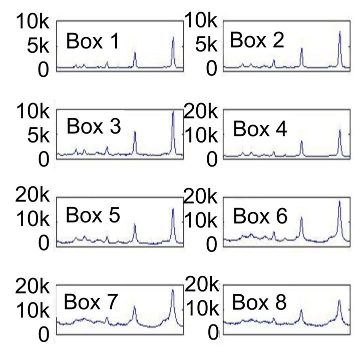

Figure 3.9: **The trace of 8 boxes from figure 3.8 after vertical binning is performed.**

Using Fityk, [9] Voigt profiles are fitted to the curves and the Lorentzian parameters extracted, and applied to equation 3.4 to obtain the average density in each box. Thus temporal (using time resolved spectra) and spatial (using spectra split into boxes) distributions for each target geometry can be determined.

3.3.1 Target Geometries

3.3.1.1 Seed Plasma Orientation

The data sets used in section 3.2 have been used to determine the electron density distributions of the stagnation layer. A Surelite laser operated at the fundamental wavelength of 1064 nm and a pulse width of 6 ns was split equally using the optical setup described in section 2.2.1.2 to generate a pulse of energy 210 mJ (105 mJ per seed) on three separate wedge angles (100^0, 140^0 & 180^0) at a seed distance of D = 1.3 mm. Figure 3.10 shows spatially resolved time integrated electron density distributions over the interaction region of the three target wedge angles. The boxes have been converted into distance in the forward expansion direction.

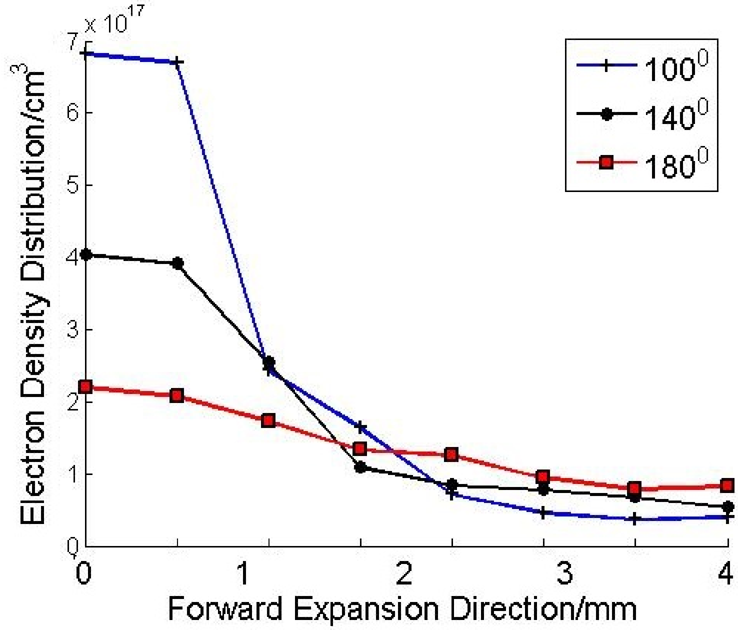

Figure 3.10: **Spatially resolved & time integrated electron density distributions in the stagnation layer generated by focussing two 105 mJ 6 ns laser pulses onto three target wedge angles.**

As figure 3.10 shows, the base of the stagnation layer (i.e. the volume of the stagnation layer material at the collision plane lying directly above the laser focal spots) is the most dense in each case. The density in this region is highest in the case of the 100^0 wedge, but this decreases sharply some 2 mm along the stagnation layer away from the targets. The densities in the case of the 140^0 and 180^0 wedges do not reach the same values, nor do they decrease as sharply. The layer created by the 180^0 wedge has the lowest density gradient, i.e. it is spread most evenly in this case. The fact that the laterally colliding plume has the most homogeneous density distribution is potentially important for certain applications, e.g. reheating of the stagnation layer, as in chapter 4.

Since the greatest variations between the plasma densities happens in the lower region of the stagnation layer, we will focus in on this domain of the plume, i.e. boxes 5-8, when comparing time resolved results, as in figure 3.11.

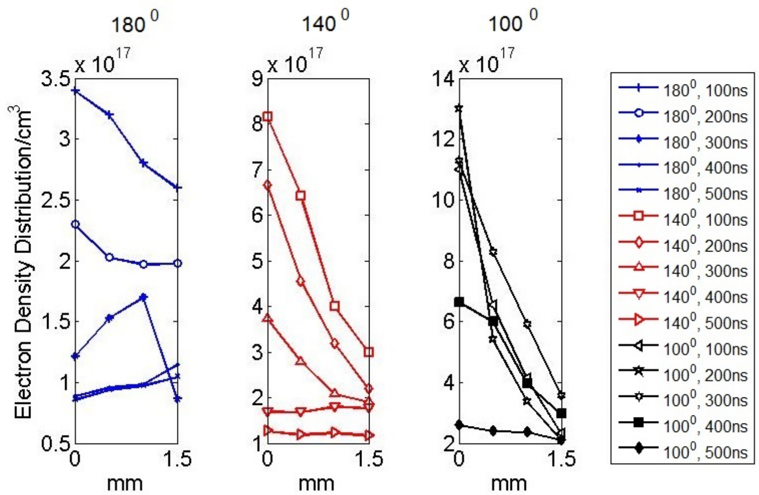

Figure 3.11: **Spatially & temporally resolved electron density distributions at the end of the stagnation layer furthest from the seed plasmas for three target wedge angles.**

Figure 3.11 shows the spatially resolved electron density distributions as a function of time and of the target wedge angle used to create them. The gate width on the ICCD camera connected to the spectrometer was set to 100 ns and the signal recorded at 5 separate time delays, from 100 ns to 500 ns after seed plasma initiation, in 100 ns steps. In the case of the 100^0 wedge target, the density declines are relatively high across the 2 mm inspection area before arriving at a more even distribution across the region by 500 ns. The same applies in all cases, although the density decline is less in the case of the 140^0 and 180^0 wedge targets.

3.3.1.2 Distance Variation

The second part of the density analysis due to target geometry variations is a comparison of the interaction region created by two seeds with varying distance, with all other parameters held constant. The distance is varied from 1.3 mm to 2.6 mm by changing the wedge prism in the optical setup. The results for time integrated and time resolved spectroscopy are shown in figures 3.12 and 3.13 respectively.

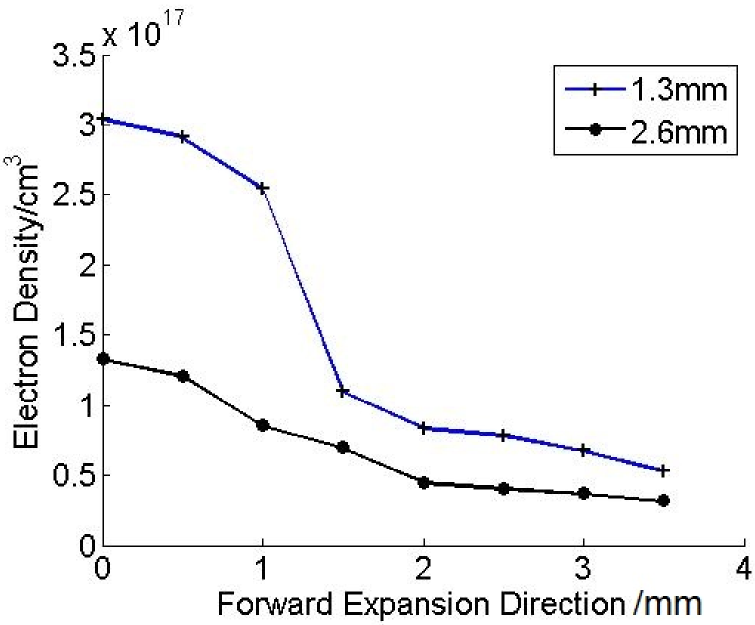

Figure 3.12: **Time integrated electron density distributions along the stagnation layer for two seed plasma separations.**

In figure 3.12 the time integrated electron density profiles show that the higher densities are at the end of the stagnation layer which is closest to the seeds and tail off as one measures further and further along the stagnation layer and away from the seed plasmas. The density of the region close to the seeds is roughly doubled when the distance is halved. The time resolved results (figure 3.13) show a drop off in densities after 100 ns for the 2.6 mm seed distance case, with slightly higher densities in the 1.3 mm case.

3.3.2 Laser Pulse Energy Variation

Spatially resolved emission spectra of a stagnation layer formed by focusing two laser pulses onto a 100^0 target wedge at 1.3 mm separation of the seed plasmas and laser pulse energies of 110 mJ, 160 mJ, and 210 mJ in a 6 ns

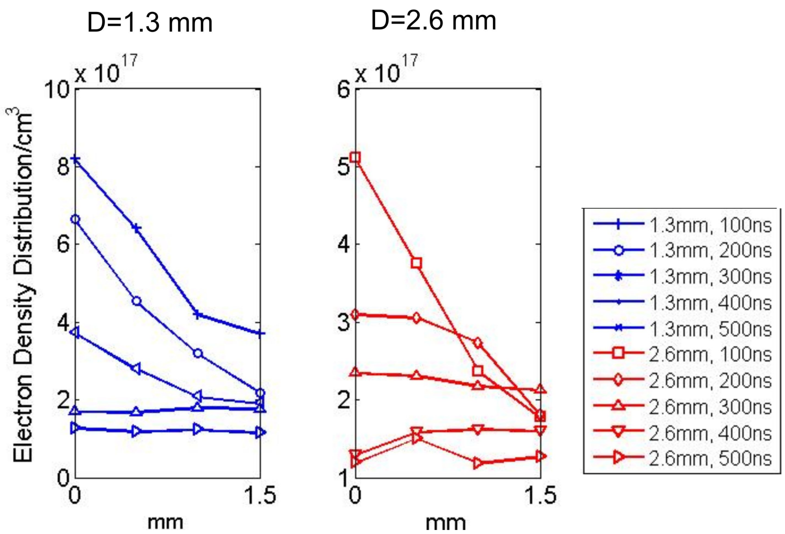

Figure 3.13: **Time resolved electron density distributions along the stagnation layer at two different seed plasma separations.**

pulse at 1064 nm were recorded using the same techniques as above. Both time integrated and time resolved spectra were recorded; a delay step size of 100 ns and range stretching from 100 ns to 500 ns (i.e. 100 - 200 ns, 200 - 300 ns etc.) after seed plasma initiation was used and the corresponding density profiles were extracted from the measurements. The time integrated results are shown in figure 3.14 while time resolved results are shown in figure 3.15. The region of interest again occurs in the furthest region of the stagnation layer, and so we will focus in on this domain of the plume, i.e. boxes 5-8, when comparing time resolved results.

As the time resolved results in figure 3.15 show, the electron densities grow relatively linearly with seed laser energy. For the lower energy cases, the densities decrease with time, but in the case of the 210 mJ laser energy, the density increases and peaks at 200 ns rather than at 100 ns.

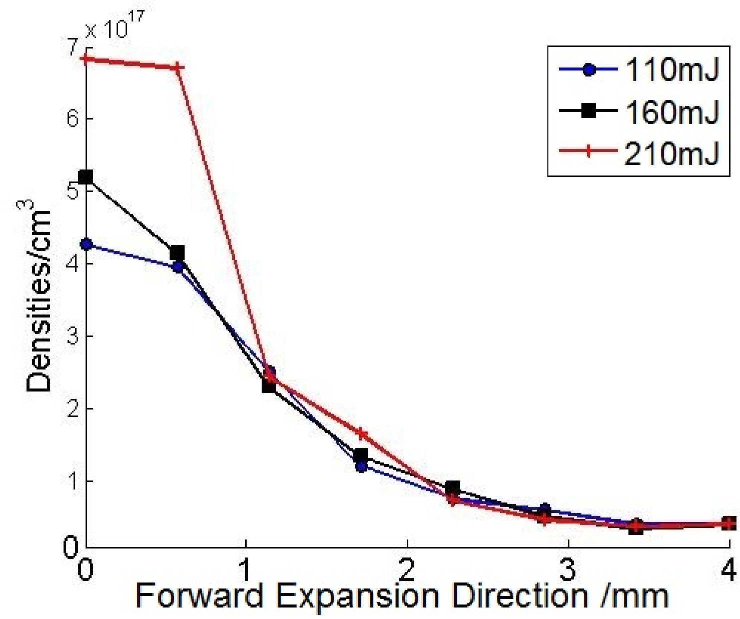

Figure 3.14: **Time integrated electron density distributions along the stagnation layer for three laser pulse energies.**

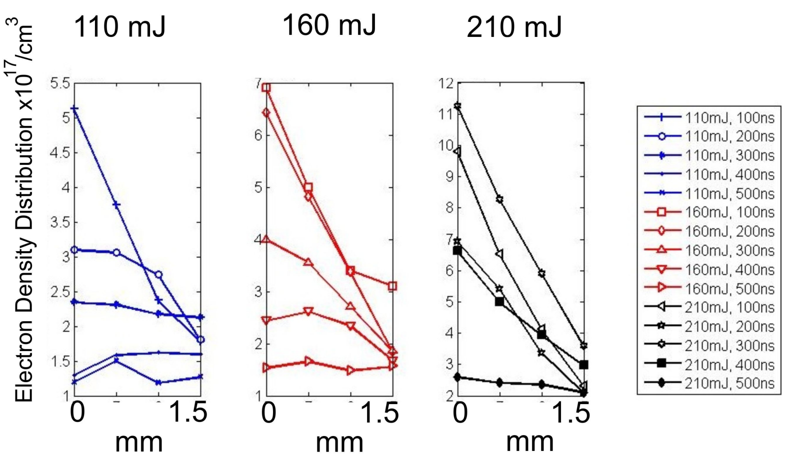

Figure 3.15: **Time resolved electron density distributions over the interaction region of three laser pulse energies.**

3.4 Spatio-Temporal Excitation Temperature Distributions

The excitation temperature has been determined by employing the Boltzmann plot method (subsection 2.3.2). In optically thin plasmas and under the assumption of local thermodynamic equilibrium [11, 12] one can plot the magnitude on the left hand side of equation 3.5 (repeated below for the reader's convenience), against the energy of the upper level of the species in ionisation stage z for several transitions to yield a linear plot (the so-called Boltzmann plot). The value of T is deduced from the slope of this plot.

$$ln\left(\frac{I\lambda}{gA}\right) = -\frac{1}{k_bT}E. \tag{3.5}$$

I refers to the integrated intensity of the spectral line, λ is the transition wavelength, E and g are the energy and degeneracy of the upper energy level respectively, A is the transition probability, k_b is Boltzmann's constant and T is the plasma temperature. The overall uncertainty of the excitation temperature is deduced using this method to be $\approx 10\%$ which mainly comes from the uncertainties in the transition probabilities and the integrated line intensities used in the Boltzmann plots. The relevant spectroscopic details for the copper transitions are listed in table 3.2.

Table 3.2: Wavelength, upper level energy, upper level degeneracy and transition probability [14] for the Cu I emission lines used in the Boltzmann plot.

Wavelength /nm	Transition	Upper Level Energy/eV	gA $\times 10^8/s$
465.11	$3d^9 4s5s\,^4\mathbf{D}_{7/2} - 3d^9 4s4p\,^4\mathbf{F}_{9/2}$	7.740	5.7
510.55	$4p\,^2\mathbf{P}_{3/2} - 4s^2\,^2\mathbf{D}_{5/2}$	3.817	0.051
515.32	$4d\,^2\mathbf{D}_{3/2} - 4p\,^2\mathbf{P}_{1/2}$	6.191	4.7
521.82	$4d\,^2\mathbf{D}_{5/2} - 4p\,^2\mathbf{P}_{3/2}$	6.192	5.8
578.21	$4p\,^2\mathbf{P}_{1/2} - 4s^2\,^2\mathbf{D}_{3/2}$	3.786	0.054

The intensities of each of these five spectral lines can be extracted from the spectra recorded in three distinct spectral windows; centred around 510 nm (as in figure 3.2) and around 465 nm and 578 nm as in figures 3.16 and 3.17 below.

The Boltzmann plot is obtained by employing equation 3.5 and using the integrated intensities in conjunction with the data in table 3.2, and the temperature is determined from the slope of the linear fit as in figure 3.18.

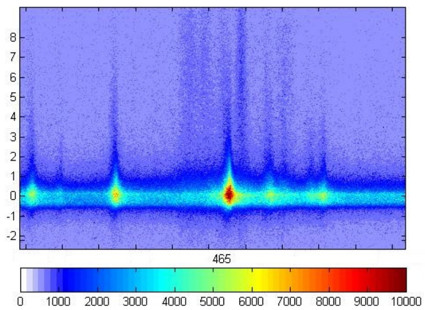

Figure 3.16: **Spectral image showing the neutral Cu transition at 465.11 nm.**

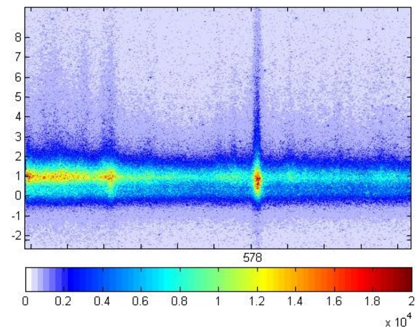

Figure 3.17: **Spectral image showing the neutral Cu transition at 578.21 nm.**

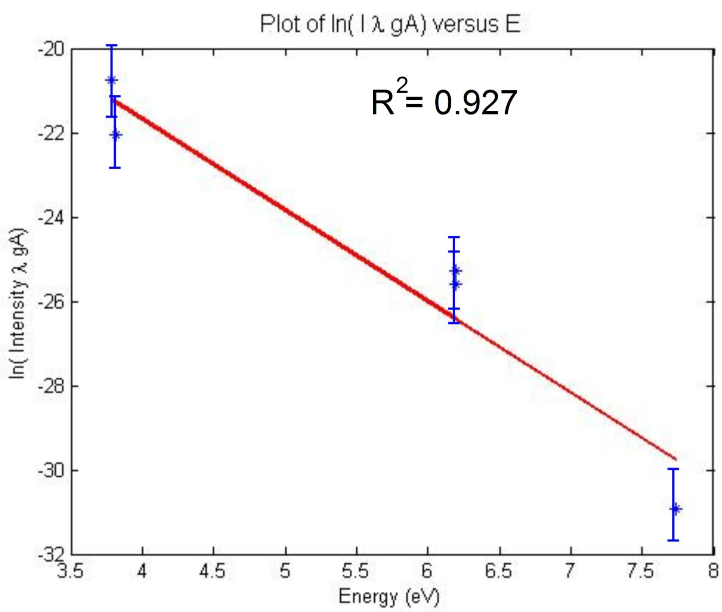

Figure 3.18: **Example of a Boltzmann plot to determine the temperature of a copper plasma constructed from the analysis of five lines and corresponding data points.**

The continuous line in figure 3.18 represents the result of a linear best fit; the slope of which gives the temperature. Note that the spectral images in figures 3.16 and 3.17 are not to scale since the gain of the image intensifier on the ICCD (section 2.2.3) and grating efficiency (section 2.2.4) must be accounted for. There are disadvantages as well as advantages involved in using three spectral windows; the measurement must be recorded three times in order to determine the temperature at each experimental setting, but the high groove density of 1200 grooves per mm of the Czerny-Turner spectrometer enables high resolution integrated intensities to be recorded, as opposed to lower resolution and a larger number of lines as in other studies [15]. The assumptions of an optically thin plasma and LTE combined with uncertainties in the transition probabilities used [16] and uncertainties in the integrated line intensities (in particular around the regions where the background continuum emission signal level is high) result in difficulties in temperature calculations, particularly at earlier plasma times. Therefore the temperature distributions presented here are for times $\geq 300ns$.

3.4.1 Target Geometries

As in sections 3.2.1 and 3.3.1 we will look at the effects on the interaction region between two colliding plasmas by varying the target geometry of the system.

3.4.1.1 Seed Plasma Orientation

Boltzmann plots have been used to determine the excitation temperature distributions of the plume. A Surelite laser operating at the fundamental wavelength of 1064 nm with a pulsewidth of 6 ns was split equally using the optical setup described in section 2.2.1.2 to generate a pulse of 210 mJ (105 mJ per seed plasma) on three separate wedge angles (100^0, 140^0 & 180^0) at a seed distance of D = 1.3 mm. Figure 3.19 shows spatially resolved time integrated temperature distributions over the interaction region of the three target wedge angles.

In the case of the 180^0 (i.e. flat) wedge target system, the plume temperature is lowest, and the temperature gradient along the major axis of the stagnation layer, i.e., away form the seed plasmas, is relatively flat. This temperature gradient increases slightly for the 140^0 case with respect to the laterally colliding plasmas case, and the temperature increases by an average of ∼1000 K. The temperature gradient remains in the 100^0 case, but the average absolute temperature increases by ∼1700 K. The seed plume velocity

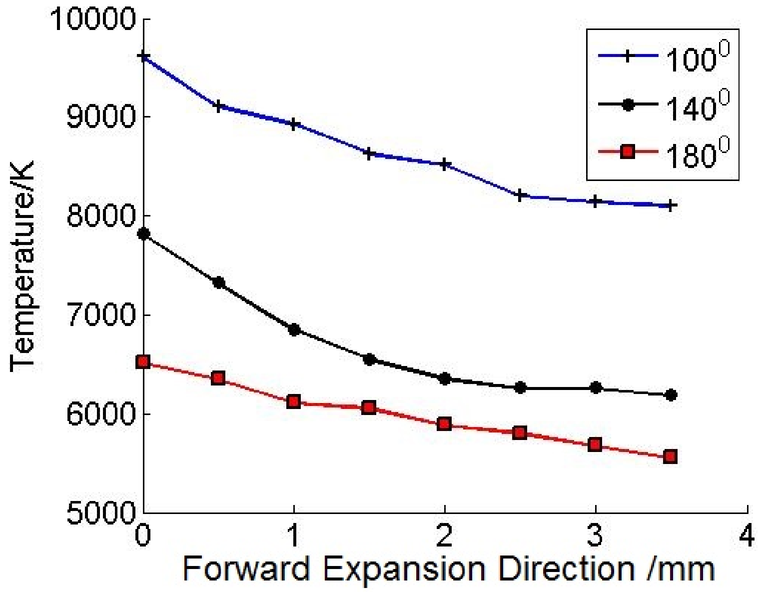

Figure 3.19: **Spatially resolved & time integrated excitation temperature distributions along the stagnation layer for three target wedge angles.**

component parallel to the target surface has increased while that normal to the surface has decreased.

The time integrated temperature distributions shown in figure 3.20 represent temperatures for times $\geq 300ns$ after seed initialisation, and $\sim 100ns$ after the stagnation layer has begun to form. In the case of the 180^0 and 140^0 wedge systems, the plasma temperature gradient is relatively gentle and so the temperatures are quite homogeneous across the plume. However, in the case of the 100^0 wedge system, there is still a decrease in the temperature visible along the stagnation layer 500 ns after seed initialisation. This decrease in temperature is approximately linear (in this temporal region) in each case.

3.4.1.2 Distance Variation

The distance between the two seed plasmas was varied, by changing the wedge prism in the optical setup (section 2.2.1.2). Using the same experimental conditions as usual, i.e. a target wedge angle of 140^0 and a pulse energy of 210

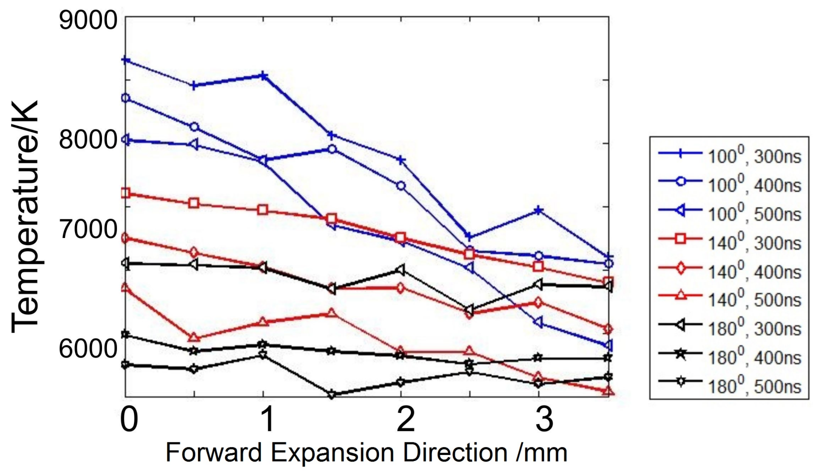

Figure 3.20: **Spatially resolved excitation temperature distributions for a range of time delays along the stagnation layer for three target wedge angles.**

mJ, seed distances of D = 1.3 mm and D = 2.6 mm were used, and a series of spectra were recorded from which temperatures were extracted. A spatially resolved & time integrated comparison of the excitation temperatures for both seed plasma separations is shown in figure 3.21, from where it can be seen that the temperature gradient is not as steep in the D = 2.6 mm case as it is in the D = 1.3 mm case.

The space and time resolved distributions are shown in figure 3.22. It can be seen that the temperature of the stagnation layer in the D = 2.6 mm case is only very slightly more homogeneous as one moves normal to the target and along the plume. The decrease in temperature is again approximately linear (in this temporal region) in both cases.

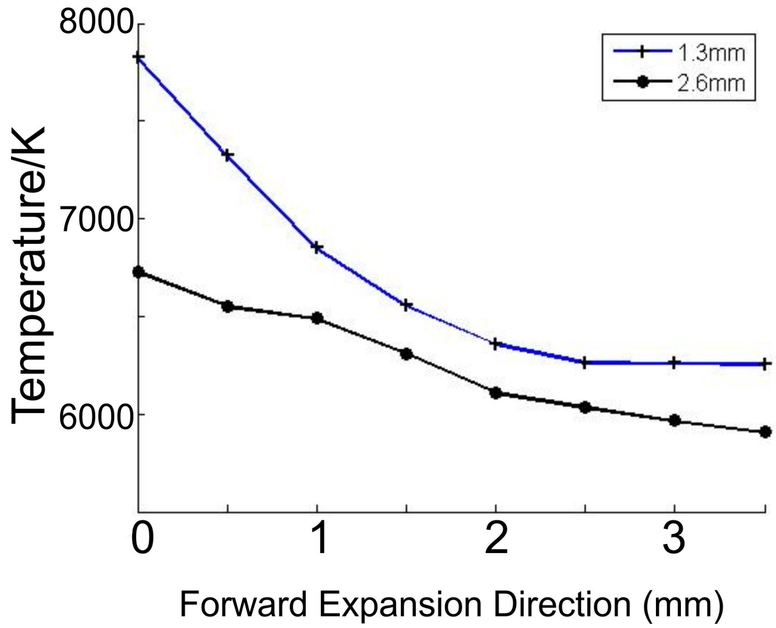

Figure 3.21: **Spatially resolved & time integrated excitation temperature distributions along the stagnation layer for two seed plasma separations, namely 1.3 mm and 2.66 mm.**

3.4.2 Laser Pulse Energy Variation

In this section, as in sections 3.2.2 and 3.3.2, we vary the energy of the laser pulse from 110 mJ through 160 mJ, to 210 mJ in a 6 ns pulse at an operating wavelength of 1064 nm, and thus the on-target irradiance for each seed plasma, and hold constant the target wedge angle (140^0) and the distance between the seeds (D = 1.3mm). The spatially resolved & time integrated results are shown in figure 3.23 below.

The effect of changing the seed laser pulse energy on the time integrated temperature distributions is a linear change in the overall temperature of the plume while the general temperature distributions do not change as the laser energies change. Space and time resolved temperature distributions (figure 3.24) show a similar pattern, with the temperatures decreasing monotonically along the stagnation layer as a function of time.

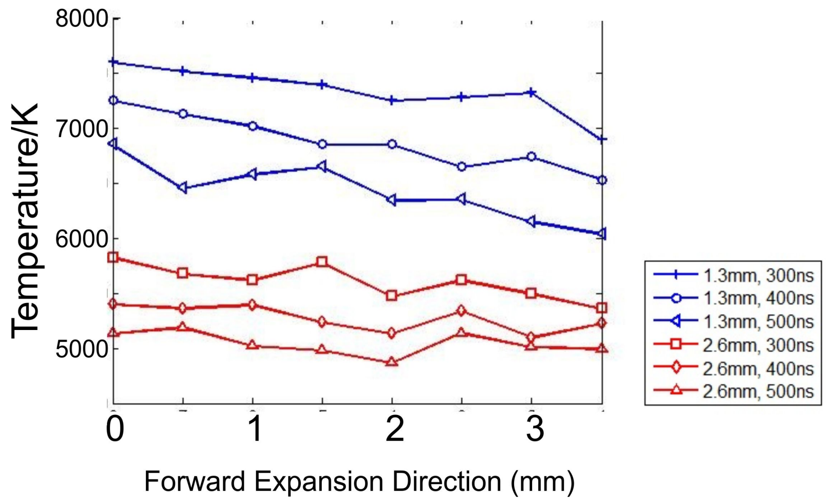

Figure 3.22: **Spatially resolved excitation temperature distributions for a range of time delays along the stagnation layer for two different seed plasma separations, namely D = 13. mm and D = 2.6 mm.**

3.5 Comparison of Emission Results

Spatially resolved and temporally integrated as well as spatially and temporally resolved imaging spectra have been used to study the interaction of counter-propagating laser-produced plasmas. The results presented show a range of different behaviours in the interaction dynamics between each of the plasma plumes, caused by differing initial conditions. A study of the progression of the peak of the intensity of the neutral emitting atoms along the stagnation layer and ions as a function of time for a range of initial conditions is presented in table 3.1, showing that while the growth rates of neutral emitting atoms are generally relatively low, i.e. $\leq 5.5 \times 10^5$ cm/s, the ions are more fast moving and vary significantly as a function of the wedge angle between the seeds. The Cu^+ ion growth rates range from 9.2 $\times 10^5$ cm/s for the case of the 1.3 mm, 210 mJ, 100^0 wedge case to 26.1 $\times 10^5$ cm/s for the 1.3 mm, 210 mJ flat target case.

In the flat target case, the stagnation layer grows predominantly in a direction normal to the target surface as time progresses. This is supported by

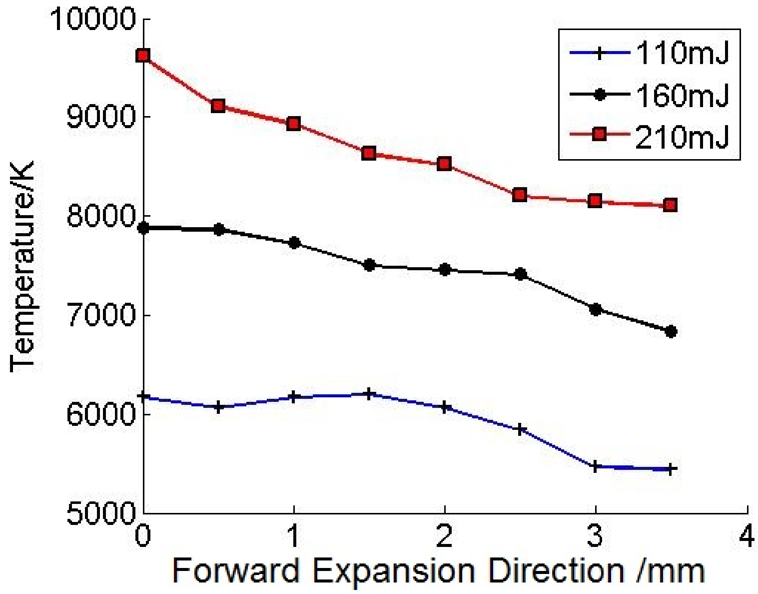

Figure 3.23: **Spatially resolved & time integrated excitation temperature distributions along the stagnation layer for three different laser pulse energies.**

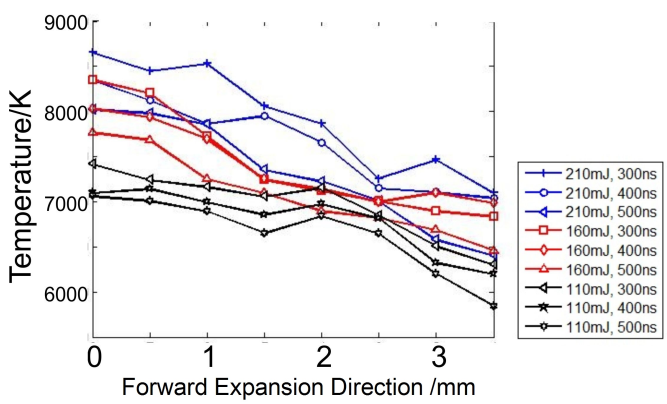

Figure 3.24: **Spatially resolved excitation temperature distributions for a range of time delays along the interaction region for three pulse energies.**

figure 3.1 (a), where the stagnation layer formed is narrow and elongated. There is little or no growth along its lateral dimension, giving a strong indication that the degree of interpenetration is quite low. This is known as 'hard stagnation', and occurs when there is a low degree of interpenetration, because the ion ion MFP (λ_{ii}) is shorter than the typical dimensions of the system [17], usually taken to be the separation of the seed plasma plumes. The collisionality parameter, ζ, is greater than unity in the case of hard stagnation (see equation 1.19).

Combining equation 1.19 with equation 1.20, one can see that ζ is highly dependent on the relative collision velocity of the seed plasmas, decreasing as the velocity increases, which in turn is caused by a decrease in the target wedge angle. To rephrase, as the target wedge closes the collisionality parameter decreases and moves towards the 'soft stagnation' regime, where the degree of interpenetration of the colliding plasmas grows. Figure 3.1 (b) and (c) illustrate this progression, where the increase in the lateral dimension, i.e. the width, and the decrease in length is apparent. The decreasing growth rates of the peak position of emitting atoms and singly charged ions (table 3.1) as the wedge angle closes, confirm this.

In general, the electron density follows the shape of the stagantion layer, (along the length of the layer) as in figure 3.1. The density reaches a maximum of $\sim 1 \times 10^{18} cm^{-3}$ in the case of the 100^0 wedge target for 1.3 mm seed distance & 210 mJ total pulse energy, where it is spread across a 1 mm range close to the base of the stagnation layer. Beyond this region it decreases sharply to $\sim 1 \times 10^{17} cm^{-3}$, as do the stagnation layers in the 140^0 and 180^0 wedge cases. They do not reach the same densities in the base region, although they do increase with decreasing wedge angle. The densities peak between 100 and 300 ns after seed initialisation in all three cases. The temperature reaches a maximum of $\sim$ 9,500 K in the 100^0 wedge target, again closest to the base of the stagnation layer. This decreases by $\sim$ 1000 K in the tail of the plasma. A simiar pattern occurs for the other cases, except that the temperatures are lower as the wedge angle opens. The time resolved temperature measurements don't show the same drop in temperature across the layer, suggesting that the majority of the temperature gradient across the layer occurs at t $\leq$ 300 ns. The effect of moving the seeds further apart is to cool the plasma; in the case investigated (i.e. 140^0 wedge, 210 mJ total pulse energy, seed distance D = 1.3 mm & 2.6 mm) the effect of doubling the seed distance was to decrease the plume temperature by $\sim$ 1000 K.

Changing the laser energy and hence the on-target irradiance had little effect on the growth rates of the species measured, i.e. neutral Cu atoms and Cu^+ ions. An increase in laser energy has a strong effect on the electron densities near the base of the stagnation layer causing the density to rise sharply, but has only minor effects beyond this region. This is in contrast to the temperatures; the influence of an increase in laser energy can be seen right along the stagnation layer where the temperature seems to increase linearly with laser energy.

3.6 Comparison of a Stagnation Layer with a Single Seed Plasma

The stagnation layer of most interest for LIBS was in the case of the 1.3 mm seed separation, 210 mJ total pulse energy, 100^0 wedge case, where relatively low species growth rates and high electron temperatures and densities occured. Here we compare these results to a plasma plume created by a single laser pulse of the same energy.

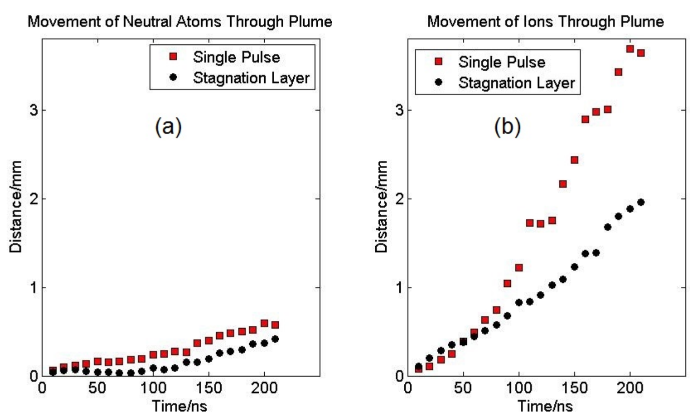

Figure 3.25: **Comparison of the movement of the peak of intensity of neutral emitting atoms and ions for a single pulse plasma with a stagnation layer.**

Figure 3.25 shows a comparison of the growth rates of species in a stagnation layer created using the settings described above, and a single plume using the same pulse energy. The velocity of the both the peak of the neutral atoms and of the singly charged ions is higher in the case of the single pulse plume, and the ions disperse at almost twice the velocity in the forward direction. The stagnation layer is confined in space which slows it's evolution through time and should cause the density gradient to be lower than the single pulse case.

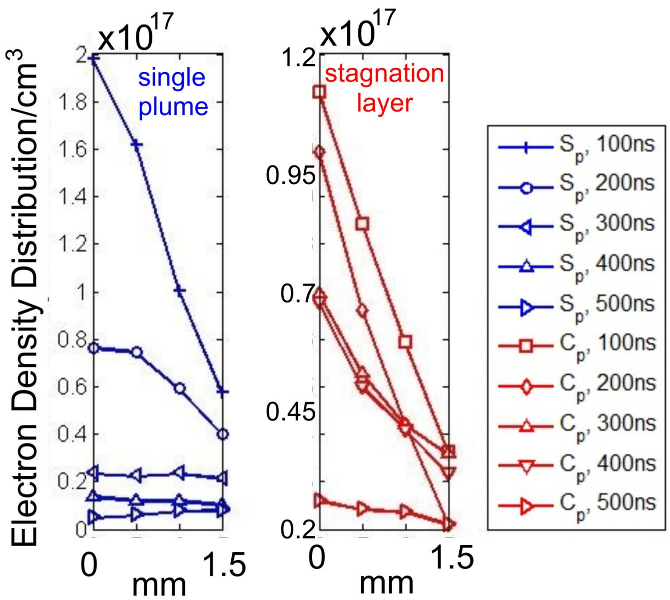

Figure 3.26: **Comparison of the electron densities of a single pulse plasma with a stagnation layer.**

The electron density distributions plotted in figure 3.26 show that the density of the single plume is almost twice that of the colliding plasma at their respective peak densities, but the density of the single plume plasma quickly decreases to a value below that of the stagnation layer ~ 200 ns after the laser pulse impinges upon the target surface, while the stagnation layer maintains it's density for a longer period. The stagnation layer also holds it's temperature for longer, as figure 3.27 shows. It is expected that the temperature of the single pulse plasma would be higher for earlier times than those shown, but decreases at a faster rate than that of the stagnation layer.

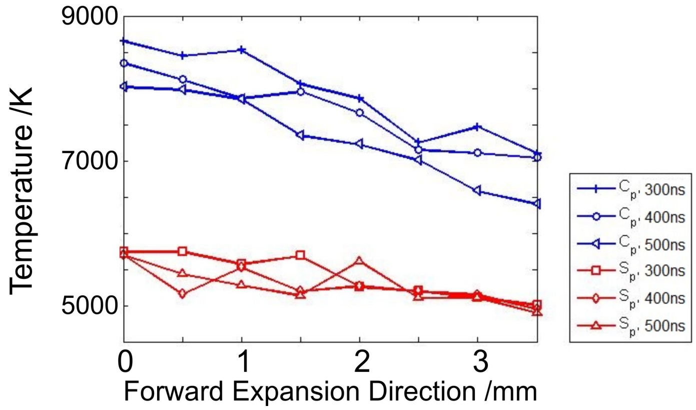

Figure 3.27: **Comparison of the excitation temperatures of a single pulse plasma with a stagnation layer.**

3.7 Summary

The orientation of two seed plasmas with respect to each other has been shown to alter the temperature, electron density, evolution of species in, and degree of confinement of the stagnation layer generated when they collide. By employing various distinct target configurations, plasma collisions at both low and relatively high growth rates were studied. By decreasing the angle of orientation between the seeds, the temperature was increased, due to increased internal collisions, and the densities were raised due to a higher number of plasma constituents involved in the collision process. Due to a lower seed plasma growth component normal (and an increased component parallel) to the target surface, the stagnation layer was confined and temperatures and densities remained high for a relatively long time duration.

We have shown that the method of changing the target angle between two colliding plasmas gives an extra dimension of control over plasma parameters such as the density, temperature and confinement. The rate of decrease of densities and temperatures is lower in the case of a stagnation layer as opposed to a single plasma plume, allowing for the highly useful property of an optical source with a long lifetime, which is suspended in space making it a useful pre-heated target for applications in e.g., LIBS.

References

[1] X. Jiang, P. Hayden, R. Laasch, J. T. Costello, E. T. Kennedy. Inter-Pulse Delay Optimization in Dual-Pulse Laser Induced Breakdown Vacuum Ultraviolet Spectroscopy of a Steel Sample in Ambient Gases at Low Pressure. *Spectrochimica Acta Part B*, 2013, In Press.

[2] O. Rancu, P. Renaudin, C. Chenaispopovics, H. Kawagashi, JC Gauthier, M Dirksmoller, T Missala, L Uschmann, E Forster, O Larroche, O Peyrusse, O Renner, E Krousky, H Pepin, and T Shepard. Experimental-Evidence Of Interpenetration And High Ion Temperature In Colliding Plasmas. *Physical Review Letters*, 75(21):3854–3857, NOV 20 1995. ISSN 0031-9007.

[3] H. Luna, K. D. Kavanagh, and J. T. Costello. Study of a colliding laser-produced plasma by analysis of time- and space-resolved image spectra. *Journal Of Applied Physics*, 101(3), FEB 1 2007. ISSN 0021-8979. doi: {10.1063/1.2431685}.

[4] P. Hough, C. McLoughin, T. J. Kelly, P. Hayden, S. S. Harilal, J. P. Mosnier, and J. T. Costello. Electron and ion stagnation at the collision front between two laser produced plasmas. *Journal Of Physics D-Applied Physics*, 42(5), MAR 7 2009. ISSN 0022-3727. doi: {10.1088/0022-3727/42/5/055211}.

[5] J. Dardis and J. T. Costello. Stagnation layers at the collision front between two laser-induced plasmas: A study using time-resolved imaging and spectroscopy. *Spectrochimica Acta Part B-Atomic Spectroscopy*, 65(8, SI):627–635, AUG 2010. ISSN 0584-8547. doi: {10.1016/j.sab.2010.03.005}. 5th Euro-Mediterranean Sympsoium on Laser Induced Breakdown Spectroscopy, Rome, Italy, Sep 28-Oct 01, 2009.

[6] S. S. Harilal. Influence of spot size on propagation dynamics of laser-produced tin plasma. *Journal of Applied Physics*, 102(12):123306, 2007. doi: 10.1063/1.2822450. URL `http://link.aip.org/link/?JAP/102/123306/1`.

[7] D. Colombant and G.F. Tonon. X-Ray-Emission in Laser-Produced Plasmas. *Journal OF Applied Physics*, 44(8):3524–3537, 1973. ISSN 0021-8979.

[8] D. Doria, K.D. Kavanagh, J.T. Costello, and H. Luna. Plasma parametrization by analysis of time-resolved laser plasma image spectra. *Measurement Science & Technology*, 17(4):670–674, APR 2006. ISSN 0957-0233. doi: {10.1088/0957-0233/17/4/010}.

[9] M. Wojdyr. Fityk: a general-purpose peak fitting program. *Journal Of Applied Crystallography*, 43(5):1126–1128, OCT 2010. ISSN 0021-8898. doi: {10.1107/S0021889810030499}.

[10] Y. Okano, Y. Hironaka, K.G. Nakamura, and K. Kondo. Time-resolved electron shadowgraphy for 300 ps laser ablation of a copper film. *Applied Physics Letters*, 83(8):1536–1538, AUG 25 2003. ISSN 0003-6951. doi: {10.1063/1.1604946}.

[11] H.R. Griem. *Plasma spectroscopy.* McGraw-Hill, New York, 1964.

[12] H.R. Griem. *Principles of plasma spectroscopy.* Cambridge monographs on plasma physics. Cambridge University Press, New York, 1997.

[13] N. Konjevic and W.L. Wiese. Experimental stark widths and shifts for spectral lines of neutral and ionized atoms . *Journal of Physical Chemistry and Reference Data*, 19(6):1307–1385, 1990. ISSN 0047-2689.

[14] C. H. Corliss and W. R. Bozman,. Experimental Transition Probabilities for Spectral Lines of Seventy Elements. *Washington: National Bureau of Standards Monograph S3, U. S. Government Printing Office*, 1962.

[15] J.A. Aguilera and C. Aragon. Characterization of a laser-induced plasma by spatially resolved spectroscopy of neutral atom and ion emissions. Comparison of local and spatially integrated measurements. *Spectrochimica Acta Part B-Atomic Spectroscopy*, 59(12):1861–1876, DEC 1 2004. ISSN 0584-8547. doi: {10.1016/j.sab.2004.08.003}.

[16] F.O. Borges, G.H. Cavalcanti, and A.G. Trigueiros. Determination of plasma temperature by a semi-empirical method. *Brazilian Journal Of Physics*, 34(4B):1673–1676, DEC 2004. ISSN 0103-9733. 10th Latin American Workshop on Plasma Physics/7th Brazilian Meeting on Plasma Physics, Sao Pedro, Brazil, NOV 30-DEC 05, 2003.

[17] P.W. Rambo and J. Denavit. Interpenetration And Ion Separation In Colliding Plasmas. *Physics Of Plasmas*, 1(12):4050–4060, DEC 1994. ISSN 1070-664X.

[18] R.K. Singh and J. Narayan. Pulsed-laser evaporation technique for deposition of thin films: Physics and theoretical model. *Phys. Rev. B*, 41:8843–8859, May 1990. doi: 10.1103/PhysRevB.41.8843. URL `http://link.aps.org/doi/10.1103/PhysRevB.41.8843`.

Chapter 4

Emission Characteristics of Ionic Species in a Tin Plasma

4.1 Introduction

In this chapter we introduce a novel technique to increase Laser Induced Breakdown Spectroscopy (LIBS) performance through improved coupling of laser energy to the target and ablated material, yielding more efficient production of plasma species in an excited state. A dual laser scheme in combination with the generation of a highly tunable stagnation layer (SL) is employed to succesfully enhance emission line intensities and emission lifetimes.

The double-pulse technique was initially reported in 1969 [1] in relation to the analysis of solid aluminum alloy samples in air; since then several studies have been undertaken (reviewed in [2]) to enhance the intensity of emission lines employing numerous configurations of the double-pulse approach. However, the reheating of a stagnation layer formed when two plasmas collide, and the benefits that such a system might offer to LIBS have heretofore not been studied.

The stagnation layer formed at the collision front between two colliding plasmas is a potentially important augmentation of the double-pulse technique for many reasons. It is a plasma suspended in space, with tunable shape, density and temperature [3]. If we consider the SL generated by colliding two nanosecond laser produced plasmas, the density can be made quite high ($10^{19} cm^3$), but the temperature is relatively low (1 - 5 eV typically) and so it does not emit strongly in certain desirable wavelength regions. Hence the SL is used simply as the fuel to be reheated by a second laser to the appropriate temperature for optimal emission. The fact that the density may be controlled for reheating-laser absorption, and also that its shape may be controlled (important for certain applications, e.g. Extreme UltraViolet Lithography (EUVL) light sources) makes stagnation layers potentially important as a target fuel.

In any consideration of the reheating of a laser plasma, one must take into account plasma shielding. The critical density (described in subsection 1.3.2) is given by

$$n_c = \frac{\epsilon_0 m_e}{e^2} \omega_p^2 \tag{4.1}$$

.

This gives a value of $\approx 1 \times 10^{21} cm^{-3}$ for the fundamental wavelength of Nd:YAG lasers (λ = 1064 nm). A plasma with a higher density will not allow the laser beam to propagate; if the density is too low the laser beam will be transmitted with little or no absorption. Previous experiments have shown that a stagnation layer created by colliding two Nd:YAG fundamental wavelength laser produced plasmas will have an electron density of the order of $10^{17} cm^{-3}$ [4]. This number can be increased in order to improve absorption, at least in the case of each seed plasma, by using a lower wavelength laser [5, 6], e.g. the first harmonic (532 nm) of the Nd:YAG laser.

Therefore, as a means of increasing LIBS sensitivity, the traditional double-pulse scheme consists of separating the two steps of sampling and excitation, and using the most appropriate laser wavelength for each. This amounts to using a long wavelength pulse for ablation and creation of the stagnation layer, followed by a higher pulse for efficient heating of the preplasma formed in the 'sampling' step.

Here we present a study of the effects of reheating the interaction region of two colliding plasmas, while varying the initialisation conditions of those plasmas. Key parameters involved in the study include variations in the intensities and profiles of the spectral lines representing various ion stages of the stagnation layer, using combinations of laser pulses with different wavelengths, energies and durations and with different target geometries, along with the effects of interpulse delay on these spectral lines. Optical diagnostics techniques such as broadband fast imaging and optical emission spectroscopy (as described in subsection 2.2.4) have been employed to probe the colliding plasmas, revealing important factors in the formation of the reheated stagnation layer. For example the studies have found that the increase in line emission is dependant on the target geometry. The target used in all of these studies was composed of bulk tin slabs.

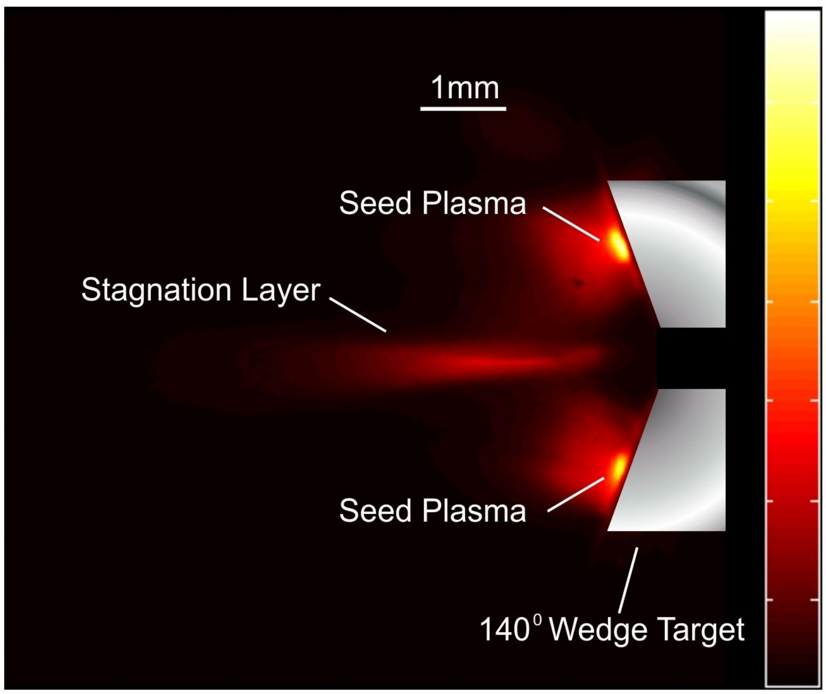

Figure 4.1: **(a) Time integrated broadband emission imaging of a reheated tin stagnation layer created on a 140^0 wedge target.**

Figure 4.1 shows a time-integrated (i.e. 10 μs) optical image of a reheated stagnation layer. The Surelite laser system (discussed in subsubsection 2.2.1.1) was used to generate pulses with a wavelength of 532 nm and a pulse duration of 4 ns FWHM; this laser beam was split in two parts using the wedge prism (subsubsection 2.2.1.2) prior to being focussed to two spots of $\sim$ 100

μm diameter. The intensity ratio of the two resulting laser beams was $\sim$ 1:1 leading to an on-target irradiance on the order of $\sim 10^{10}$ W/cm^2 (depending on the energy per pulse). The focussed laser pulses irradiated slab targets with a wedge angle of 140^0 between them and with a seed separation of 1.3 mm, while the stagnation layer was reheated by a 1064 nm laser pulse carrying an energy of 340 mJ in a pulse of duration of 6 ns, with a delay of 120 ns after seed plasma formation.

4.2 Stagnation Layer Optimisation

In this section we will study the effects of changing the seed laser wavelength on emission line intensity and emission lifetimes of specific spectral lines in the stagnation layer, as well as measuring spatially and temporally resolved electron density distributions. (N.B. the emission lifetime is a separate value to the lifetime of the upper state in the transition). A variety of models exists in the literature for laser produced plasmas under vacuum conditions e.g. [7], and experiments carried out [6] reflect the findings; the laser wavelength has a significant effect on properties such as electron temperature and density, which strongly affect the line intensies. Here we study the effects of the generation of two colliding tin laser plasma pulses by (i) a 532 nm pulse, and (ii) a 1064 nm pulse. Using the Colombant & Tonon [7] model described in subsection 1.5.2, the ion fractions for both laser wavelengths as a function of temperature have been calculated, using a fixed electron density of 10^{18} cm^{-3} and for temperatures up to 5 eV, which are similar to those used in the work presented here. Figure 4.2 shows that a plasma created by a longer wavelength pulse will have higher ionisation states at a lower temperature. However, equation 1.16 from the same model relates the temperature to the laser wavelength,

$$T \propto (I\lambda^2)^n \tag{4.2}$$

where I is the laser pulse irradiance and n=0.6 typically. The plasma created by the longer wavelength laser pulse will have a higher temperature resulting in a closer ionisation balance than two plasmas of the same temperature, due to higher densities in the plasmas created by shorter wavelengths, leading to collisional radiative excitations to higher states.

Here we will look at the electron density distributions as well as the en-

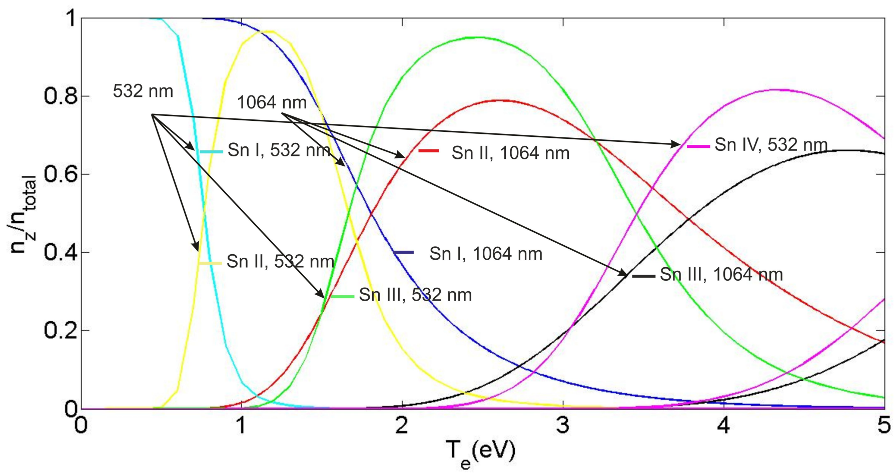

Figure 4.2: **Ion fractions for a LPP generated using a 532 nm and a 1064 nm laser pulse at a fixed density of 10^{18} cm^{-3}**

hancement of intensities and emission lifetimes of two emission lines; namely the 645.4 nm SnII line ($5s^2 6p\,^2\mathbf{P}_{3/2} - 6s\,^2\mathbf{S}_{1/2}$) and the 485.97 nm SnIII line ($5s6p\,^3\mathbf{P}_1 - 6s\,^3\mathbf{S}_1$).

Figure 4.3 shows sample images of broadband (550 nm - 950 nm) time resolved emission imaging of a tin stagnation layer created using two 50 mJ 532 nm laser pulses of 4 ns FWHM duration on a 140^0 wedge target. Note the interaction region begins to emit radiation $\sim$ 40 ns after seed initialisation, and the brightness peaks at $\sim$ 150 ns. By 290 ns there is very little emitted radiation in this wavelength region, even with maximum intensifier ICCD gain.

Emission imaging helps track the formation of the stagnation layer and can give a time-space map of its evolution. Spectrally filtered imaging allows tracking of excited state atomic & ionic species in certain circumstances. It can also be used to compare directly with hydrodynamic fluid codes, however it does have its limitations. Spectroscopy gives much better species selectivity, and combined with spatial resolution gives unprecedented space-time measurement capability (see chapter 3). Three lines are presented for spectral analysis here; the 485.97 nm SnIII line ($5s6p\,^3\mathbf{P}_1 - 6s\,^3\mathbf{S}_1$),

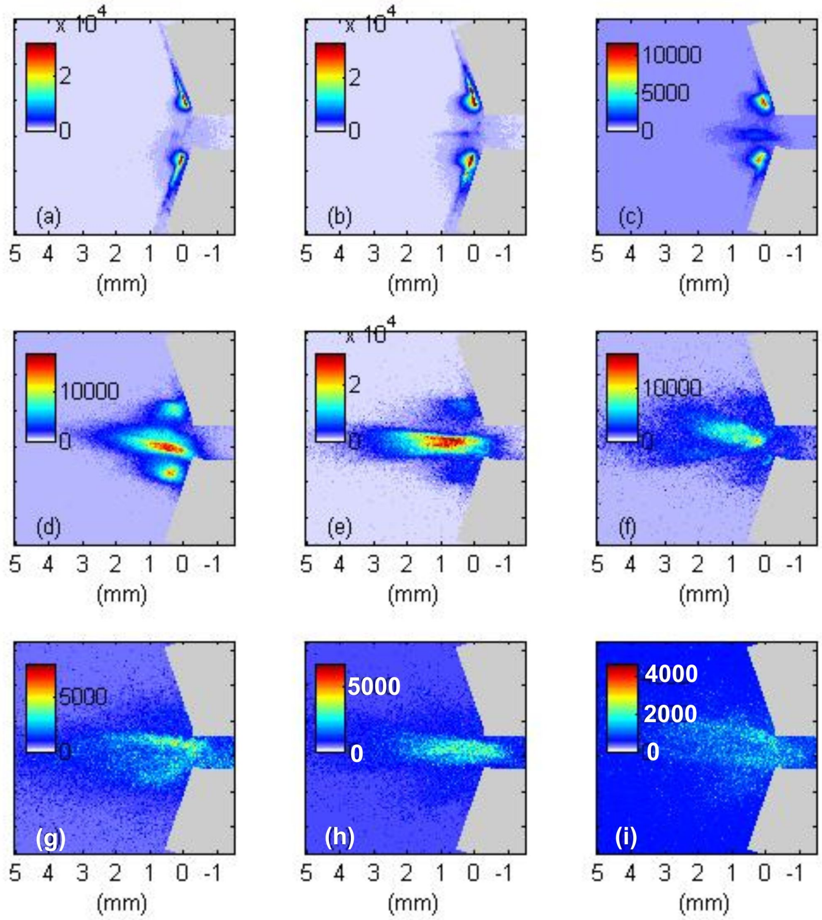

Figure 4.3: **Time resolved broadband emission imaging of a tin stagnation layer created on a wedge target acquired at times (a) 0 ns, (b) 40 ns, (c) 80 ns, (d) 120 ns, (e) 160 ns, (f) 200 ns, (g) 230 ns, (h) 260 ns, & (i) 290 ns. Images (a), (b) & (c) were acquired using an intensifier gain setting of 1500, (d) was acquired at a setting of 3000, and (e), (f), (g), (h) & (i) were acquired at a setting of 4000.**

the 492.57 nm SnIII line ($5s6p\,^3\mathbf{P}_0 - 6s\,^3\mathbf{S}_1$) and the 645.4 nm SnII line ($5s^26p\,^2\mathbf{P}_{3/2} - 6s\,^2\mathbf{S}_{1/2}$). The SnIII lines can be recorded in a single spectral window, as in figure 4.4.

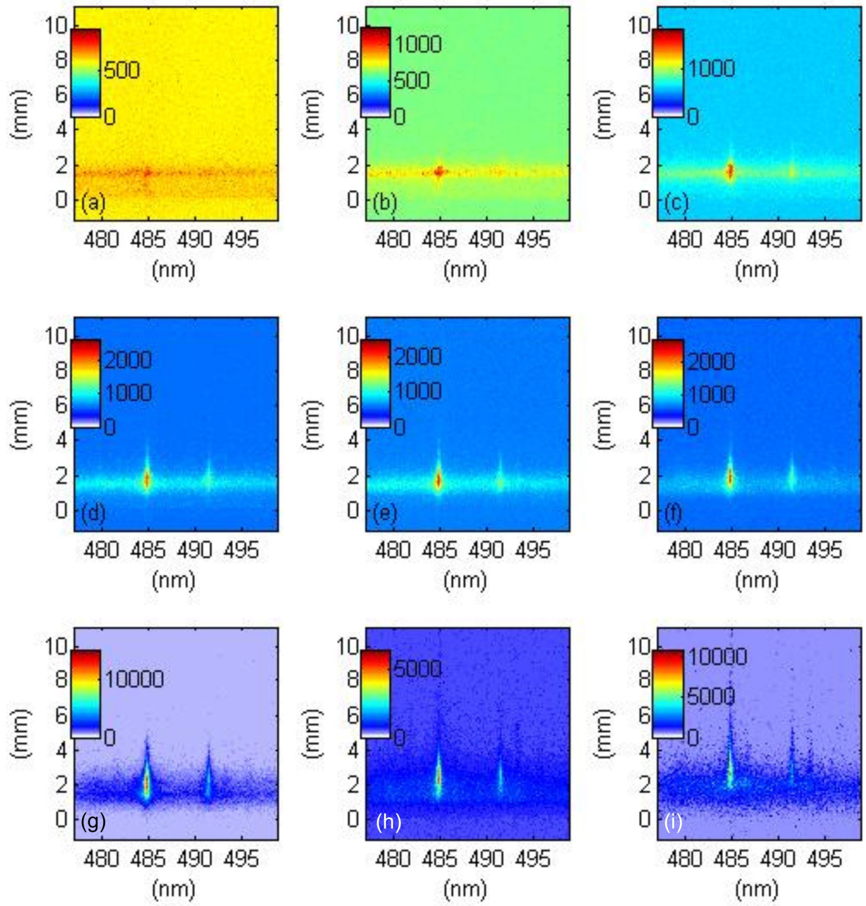

Figure 4.4: **Time resolved emission imaging spectra of the 485 nm and 492 nm specrtral lines of a tin stagnation layer created on a wedge target acquired at times (a) 40 ns, (b) 60 ns, (c) 90 ns, (d) 120 ns, (e) 150 ns, (f) 180 ns, (g) 210 ns, (h) 240 ns, & (i) 270 ns. Images (a), (b), (c), (d), (e) & (f) were acquired using an intensifier gain setting of 2000, (g) & (h) were acquired at a setting of 3000, and (i) was acquired at a setting of 4000.**

Figure 4.4 shows the spectral evolution of the two SnIII lines mentioned above as a function of time. The spectra of the stagnation layer formed by the collision of two seed plasmas which were in turn created by a pair of frequency doubled (532 nm) Q-switched laser pulses each carrying an energy of 50 mJ in pulses of duration 4 ns FWHM, focussed on a wedge target with an angle of 140^0 between each seed and with a seed separation of D = 1.3 mm, are presented in this figure. They show that a weak signal (mainly continuum) begins to appear at $\sim$ 40 ns, while discrete spectral lines do not become apparent until 80 or 90 ns. The earlier continuum signal is indicative of an initially hot and dense layer with a large number of electrons just as the collision front is forming; it is well known [8] that the separation of charge in space plays a significant role in the stagnation of various plasma constituents and arrival of electrons prior to other plasma constituents has previously been reported [9].

However, later results (section 4.3) show that the reheating laser pulse is successfully coupled to the stagnation layer even at these early times; inverse bremsstrahlung (IB) is required for this coupling mechanism which in turn requires the presence of ions. Therefore the most highly ionised (i.e. the fastest, due to ambipolar effects) ions have reached the collision plane by this stage ($\approx$ 90 ns) favouring IB and electron-ion recombination which will later add to the excited states that will decay yielding spectral line emission from lower charge states. The dense plasma will exhibit opacity effects at this early stage, attenuating line emission so severely that they become buried below the superimposed continuum. At later times the two lines become apparent and the 485 nm line is more intense than the 492 nm line; otherwise the evolution (i.e. the relative intensity and motion) of both lines is similar, as expected.

If we look at the 645 nm line (figure 4.5) we can see that the presence of continuum emission at an early stage is apparent here also. The emission lifetime of this line is longer than either of the SnIII lines, although it is not as intense (even accounting for other factors such as the grating efficiency). The 645 nm line represents a lower charge state and this is related to ionisation balance. As the plasma expands, the temperature drops and so the Sn^{2+} fraction drops while the Sn^{+} fraction will be favoured (as per the Colombant & Tonon collisional radiative model, figure 4.2).

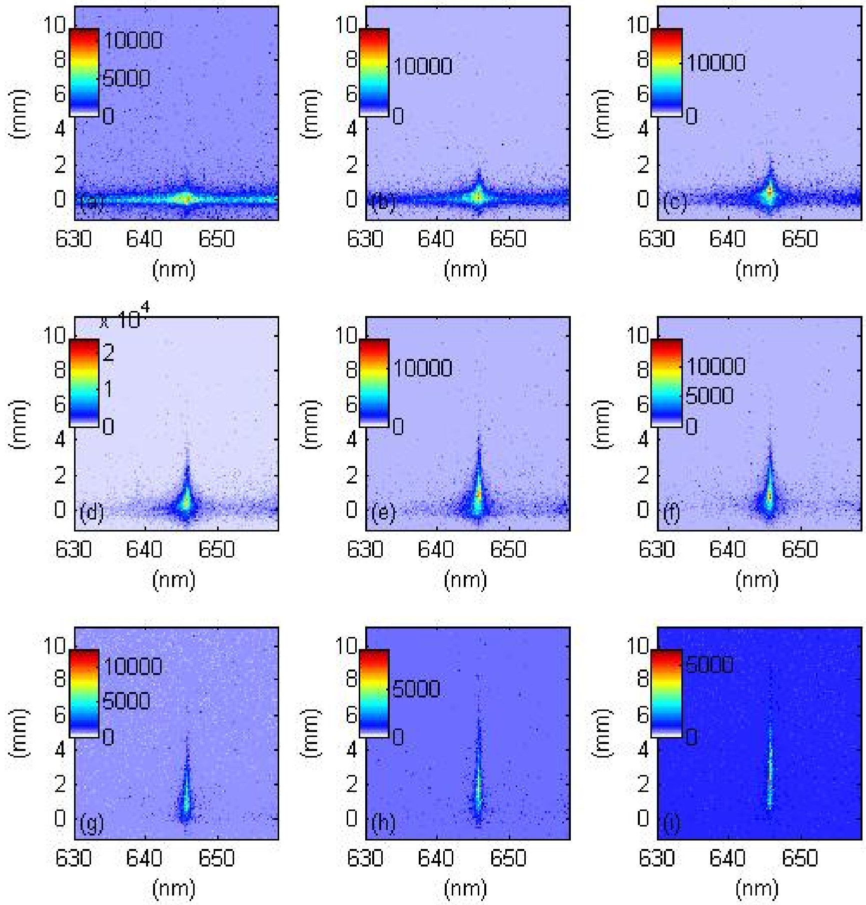

Figure 4.5: **Time resolved broadband emission imaging of a tin stagnation layer created on a wedge target acquired at times (a)40 ns, (b)60 ns, (c)90 ns, (d)120 ns, (e)150 ns, (f)180 ns, (g)210 ns, (h)240 ns, &(i)270 ns. All images were acquired using an intensifier gain setting of 4000.**

4.2.1 Optical Time of Flight Studies

A more detailed analysis can be carried out by optical time-of-flight (OTOF) studies of the plasma, which give information regarding the time taken by a particular plasma specie to evolve after the plasma is formed, and the intensity of lines as a function of time. Lineouts of the spectra along the length of each spectral line were obtained as follows. A box, enveloping the complete image region of the spectral line which was 20 pixels wide and stretched along the full length of the line, was defined. The lineout was obtained by first integrating across the 20 pixel width at each vertical (along the stagnation layer direction) position. The resulting trace was then plotted for each spectral line of interest at different time delays after seed plasma formation. Figures 4.6 and 4.7 show the intensities of these lineouts for the 485 nm line and the 645 nm line respectively, plotted as a function of time. The intensities grow to a peak at around ~ 150 ns in each case, after which point in time the line starts to fade and is barely visible after 300 ns. The position of the intensity peak of each lineout moves away from the target at different velocities in each case.

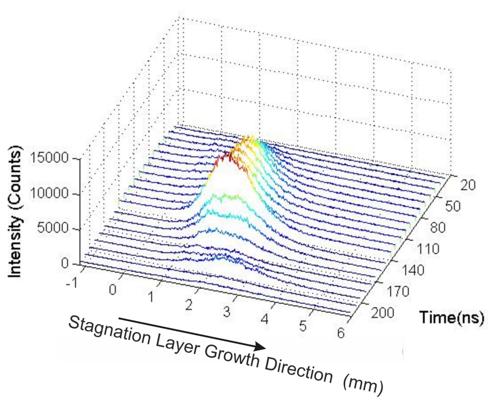

Figure 4.6: **Time and space resolved plot of the spectral line emission along the stagnation layer for the doubly ionized Sn ions as tagged with the Sn III 485 nm line. It can be seen that the peak intensity point moves along the stagnation layer as time progresses.**

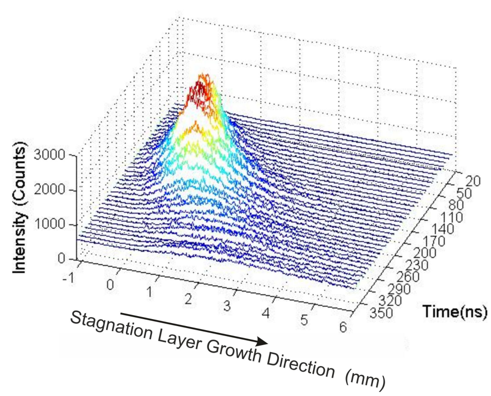

Figure 4.7: **Time and space resolved plot of the spectral line emission along the stagnation layer for the singly ionized Sn ions as tagged with the Sn II 645 nm line. It can be seen that the peak intensity point moves along the stagnation layer as time progresses.**

When comparing the intensities of these lines, the intensifier gain (subsection 2.2.3) and the grating efficiency at each wavelength (subsection 2.2.4) must be accounted for. Figure 4.8 shows the movement of the peak of intensity of the three aforementioned lines in a stagnation layer created using two 532 nm seeds and two 1064 nm seeds. Figure 4.10 shows the spectral line at 645 nm due to Sn^+ ions, isolated and magnified from figure 4.9. The variables held constant were the laser energy used to create each seed (50 mJ), the seed separation (1.3 mm) and the geometry of the target (a 140^0 wedge).

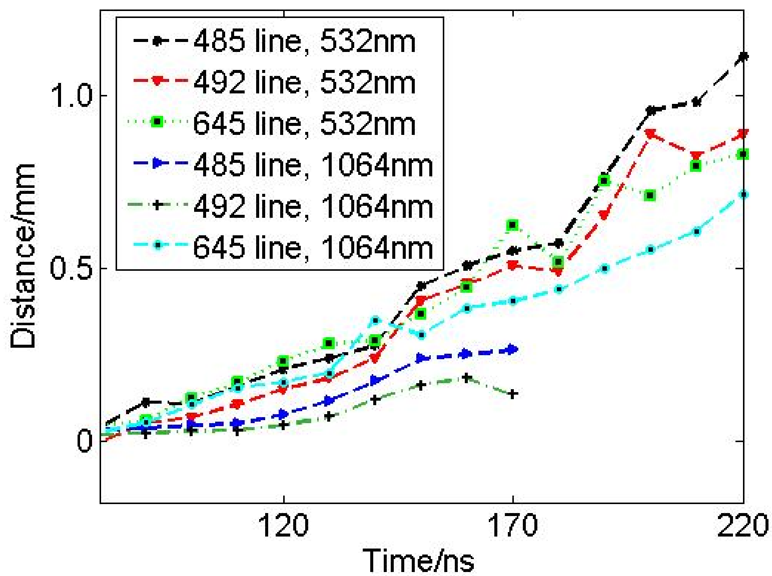

Figure 4.8: **Comparison of the movement of the peak intensity position along the stagnation layer of emitting ions in a stagnation layer, Sn^{2+} (485 nm and 492 nm) and Sn^+ (645 nm), for two different laser wavelengths.**

The velocity of the peak of each line does not vary significantly; in each case it is of the order of 10^4 cm/s. It can be seen that the velocities of the two SnIII lines are the same (as expected), and the velocities of the SnII line are lower than that of the SnIII line. Note that due to the lack of data points it is difficult to fit a straight line to either of the SnIII lines in the stagnation layer created by the longer wavelength seeds. Evidence of the separation of charge in space occurring in expanding single plasma plumes has previously been reported [10], where it was found that a fast electron bunch leads the expansion of the plasma, followed by the more highly charged ions. The excited neutral species were the slowest moving particles. This phenomenon is also observed and presented elsewhere in this work (chapter 3). Velocity is used here in the sense of the rate of change of peak intensity position with time. In the more usual case of plasma plumes expanding from the laser focal or deflagration zone, it is quite usual to talk about plume expansion velocities. Here, the stagnation layer is a plasma in the sense that it contains ionised matter, however it's expansion is not driven by the more usual hydrodynamic effects, e.g., density and pressure gradients, as in laser plasmas. Rather its growth outwards in time along the major axis is reflective of the delayed arrival of material which has to travel greater and greater distances to reach the more distant points on collision plane - in effect the 'expansion' or outward growth of the stagnation layer is determined by the time-of-flight of seed plasma material to the collision plane. Of course, material closer to the target will have a component of velocity along the layer and so as time proceeds, some material will move along the layer, i.e the layer itself will move. Also, accumulation of material just arriving and stagnating with material moving along the layer creates a localised increase in material density, which moves as time proceeds.

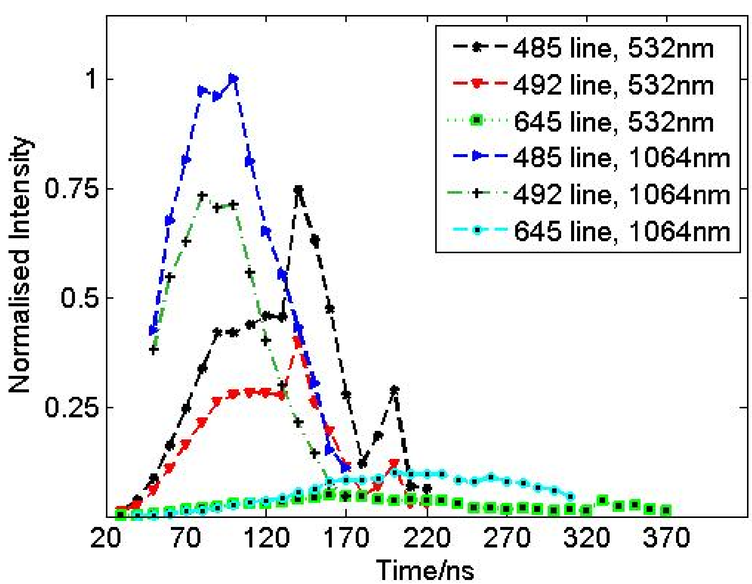

Figure 4.9: **Comparison of spatially integrated intensities of emitting Sn^{2+} and Sn^{+} ions in a stagnation layer created by seed plasmas generated with 1064 nm laser wavelength and by seed plasmas generated with 532 nm laser wavelength.**

The intensity of each line is vitally important in the context of LIBS. A comparison of the spatially integrated intensities of each line as a function of time and seed laser wavelength is shown in figure 4.9.

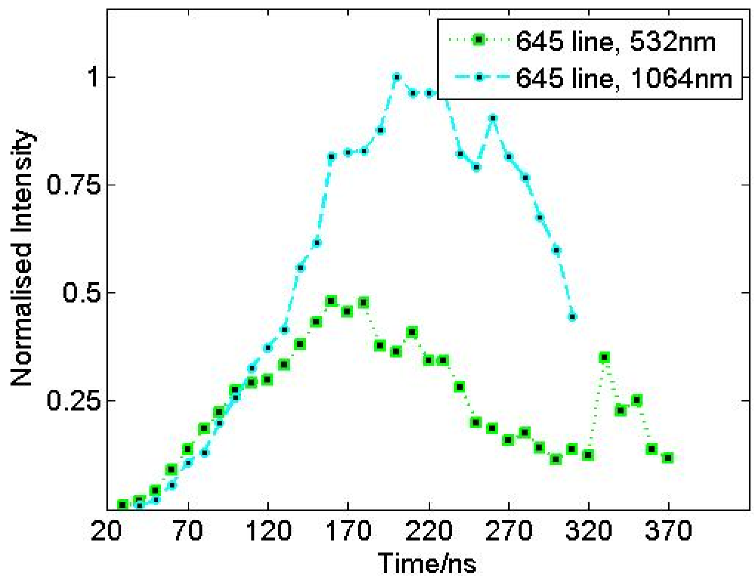

Figure 4.10: **Comparison of spatially integrated intensities of emitting Sn^{+} ions in a stagnation layer created by seed plasmas generated with 1064 nm laser wavelength and by seed plasmas generated with 532 nm laser wavelength.**

The integrated intensities of spectral lines created by Sn^{2+} in the stagnation layer generated by the longer wavelength seeds peak earlier than that of the shorter wavelength (i.e., 532 nm) seeds; however the SL created by two 532 nm laser pulses emits for longer. The Sn^{+} spectral lines peak earlier for the 532 nm case, and also emit for longer in this case. The higher intensities may be misleading; as noted earlier continuum emission exists at earlier times which increases the integrated intensity but is not useful for LIBS. LIBS requires high signal to background ratio which is not available at earlier times. The increased duration of the SL emission in the case of the 532 nm laser generated seed plasmas may be explained in terms of plasma shielding; since the plasma frequency scales as the square root of the plasma density, the shorter the wavelength of the laser field, the more dense the seed plasma created. Accordingly it can be expected that the stagnation layer will be more dense and so the emission intensity, relative to the SL created with 1064 nm seeds, should be expected to be of longer duration, as observed.

The 1064 nm laser creates hotter (equation 4.2) plasmas but they are of lower density at this distance from the surface [6]. At the collision front they have much more translational energy to convert to thermal energy in the stagnation layer which is initially hotter but decays rather rapidly. For the shorter wavelength laser a more dense but cooler (lower temperature and hence more slowly moving) seed plasma is produced. This then results in lower temperature stagnation layers which last longer because the seeds are moving more slowly and hence the growth and decay of the stagnation layer and its emission are more slow than in the 1064 nm case.

4.2.2 Spatio-Temporal Electron Density Distributions

In the current context, we are particularly interested in the density of the stagnation layer plasma. As stated earlier, the density needs to be high enough to absorb the second laser, without reaching the plasma's critical density where shielding will occur and the reheating laser will be completely reflected from the layer. The density distributions were measured using the Stark broadening method (subsubsection 2.3.1.3). The change in full width at half maximum of the Lorentzian component ($\Delta\lambda_{1/2}$, in nm) of the 645 nm Sn^+ line is used to estimate the electron number density. The equation of interest is reproduced here for the reader's convenience:

$$\Delta\lambda_{1/2} = 2w(n_e/10^{16}) \tag{4.3}$$

where w in angstroms is the electron-impact parameter of the 645.4-nm SnII line, obtained from reference [11] for two temperatures; 0.86 and 2.86 eV. We estimated the density of the plasma by assuming the impact parameter varies linearly in the temperature range mentioned above.

4.2.2.1 Electron Density Distributions as a Function of Laser Wavelength

The electron density distributions of stagnation layers created by varying seed laser wavelengths were measured and are presented in figures 4.11 and 4.12.

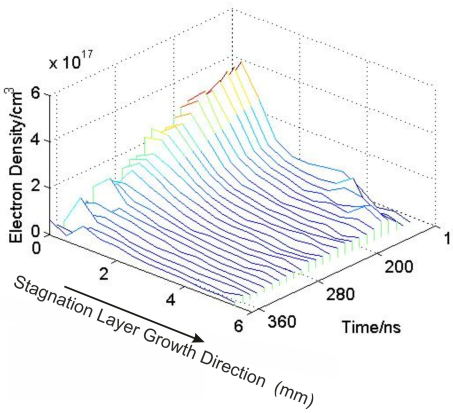

Figure 4.11: **Electron density distributions of a stagnation layer created using two 532 nm seeds on a** 140^0 **wedge target.**

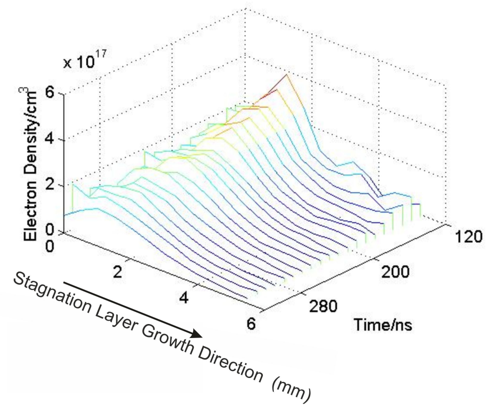

Figure 4.12: **Electron density distributions of a stagnation layer created using two 1064 nm seeds on a** 140^0 **wedge target.**

N.B. When comparing the stagnation layer generated by two different seed laser wavelengths as in figures 4.11 and 4.12 it should be noted that the power density on each target surface has been held constant. The laser energy has been increased by 50% in the case of the 1064 nm laser wavelength since the FWHM of the laser pulse is 4 ns FWHM in the case of the 532 nm laser and 6 ns FWHM in the case of the 1064 nm laser. The power density is calculated using the following equation:

$$Applied\ Power\ Density = E/\Delta T \times 1/\pi r^2 \tag{4.4}$$

where E is the energy of the incident laser pulse, ΔT is the FWHM of the laser pulse and r is the radius of the laser focal spot. In each case the power density for each seed is $\sim 1 \times 10^{11}\ Wcm^{-2}$.

The density distribution along the stagnation layer major axis (direction of growth, i.e. normal to the target surface), is similar in both cases and so a comparison of the peak of the density is justified. Following the peak for each gives a plot as in figure 4.13.

Figure 4.13 shows that the densities are similar for both, although more information is available for the 532 nm seeds - this is another reflection of the extended emission observed for this laser wavelength compared to the 1064 nm seed case.

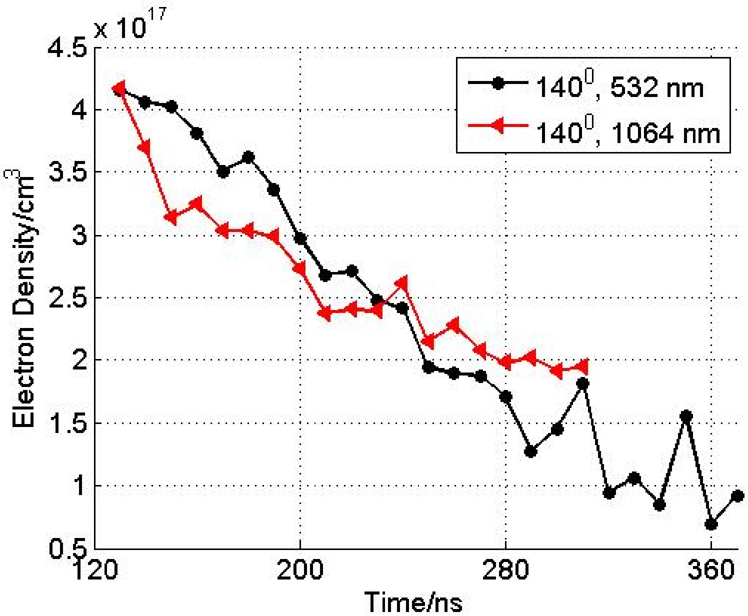

Figure 4.13: **Comparison of the peak density in a stagnation layer created by two 532 nm seeds and by two 1064 nm seeds as a function of time.**

4.2.2.2 Electron Density Distributions as a Function of Wedge Angle

The target wedge angle can be varied using the setup described in subsubsection 2.2.1.3. The resulting effects have been explored in detail for the case of colliding copper plasmas (chapter 3). Here we use the conclusions gathered from those experiments to vary the shape and density of the stagnation layer. Figures 4.14, 4.15 (as in figure 4.11, repeated here for comparison), 4.16 and 4.17 show the electron density distributions of a 180^0 wedge target system, a 140^0 wedge target system, a 100^0 wedge target system, and an 80^0 wedge target system, respectively. Note in the case of the 180^0 wedge, that the density peak is quite sharp in space at earlier times, and broadens as it decreases. The stagnation layer is not as confined as in the other cases, allowing for a relatively quick expansion into vacuum after cessation of seed collisions. This broadening as a function of time as the density peak decreases occurs in the case of both the 140^0 and the 100^0 case, although the decrease is not as sharp due to confinement of the layer. In the 80^0 case the peak density remains at a high value until around 180 ns after seed initialisation, where it drops off to values similar to the other cases. This is reflected in figure 4.18, where the peak density of each as a function of time is shown.

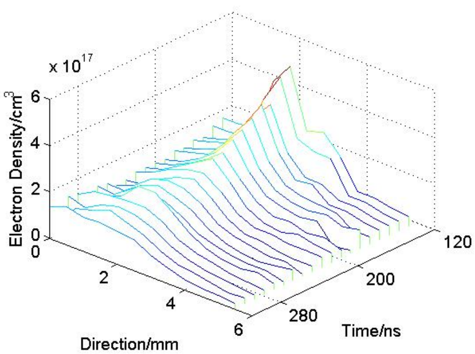

Figure 4.14: **Electron density distributions of a stagnation layer created using a flat target (180^0).**

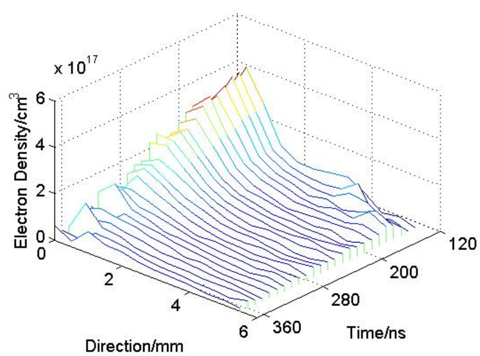

Figure 4.15: **Electron density distributions of a stagnation layer created on a** 140^0 **wedge target.**

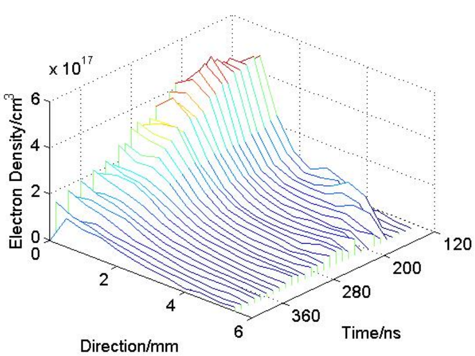

Figure 4.16: **Electron density distributions of a stagnation layer created created on a** 100^0 **wedge target.**

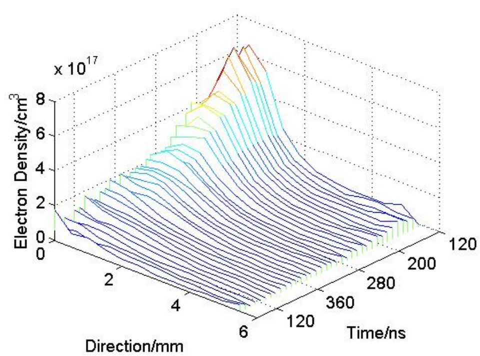

Figure 4.17: **Electron density distributions of a stagnation layer created on a** 80^0 **wedge target.**

A study of the lateral density distributions has not been carried out, but since the density distributions seem to follow the emission intensity distributions (see figure 3.1) we can assume that the density peak broadens as the wedge angle decreases. When reheating of the stagnation layer is carried out, this will become important as a higher proportion of higher density 'fuel' is available to the reheating laser allowing the focal spot to be larger or the tolerance in the focal spot positioning to be relaxed, for example.

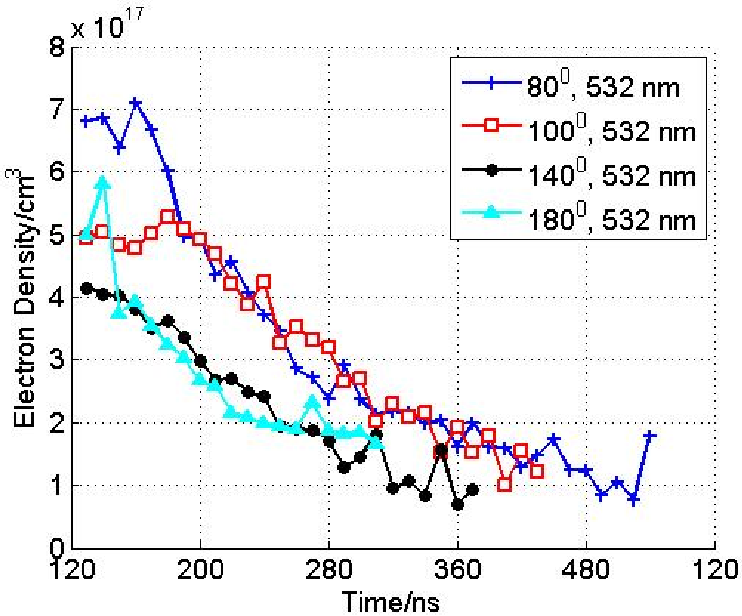

Figure 4.18: **Comparison of the peak density in a stagnation layer created by two 532 nm seeds and by two 1064 nm seeds as a function of wedge angle & time.**

4.2.3 Opacity

Opacity tends to reduce line intensities and can attenuate line intensities to the point where line intensities are reversed, i.e., the centre portion of a line profile appears to have been sliced out.. Since the emission intensity scales as Nf where N is number of excited ions and f is the oscillator strength of the transition, while absorption (opacity) scales as e^{Nfl}, where l is the absorption length, it is clear that strong lines or transitions (i.e., high f value), experience also the strongest absorption while trying to pass through the cooler outer regions of the plasma plume. Figure 4.19 and 4.20 shows the lineouts as a function of time for the 485 and 492 line transitions for the 80^0 wedge, in which case the density is highest and the plume most confined.

A dip occurs in each line at $\sim$ 100 - 200 ns, although at different regions along the length of the plume. This suggests one of two things: there are density 'islands' in the plume, or opacity is apparent. Since no density islands were apparent in the analysis in subsubsection 4.2.2.2, and the intensity of

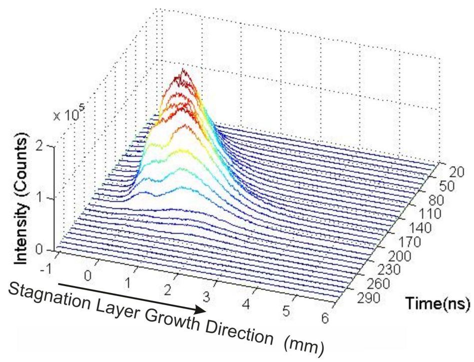

Figure 4.19: **Opacity effects on the spatially integrated intensities of emitting ions in a stagnation layer (485 nm line) as a function of time for an 80^0 wedge target setup**

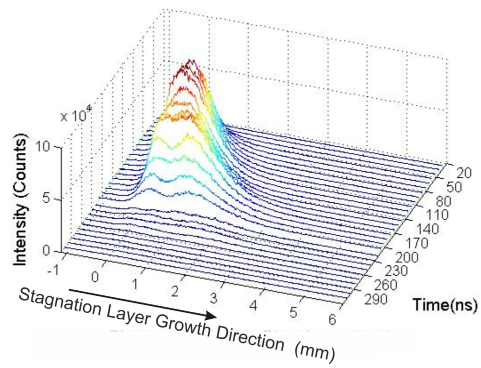

Figure 4.20: **Opacity effects on the spatially integrated intensities of emitting ions in a stagnation layer (492 nm line) as a function of time for an 80^0 wedge target setup**

the dip occurs in different regions along the plume for the different lines, it is more likely that the dip is due to opacity in the plasma. This 'dip' was not observed in the larger wedge angle, lower density plasma plumes. The significance or otherwise of opacity in the current context will become apparent in the following section.

4.3 Reheating the Stagnation Layer

The aim of the dual pulse LIBS technique is to efficiently couple laser light to a preformed plasma, in order to increase the signal-to-background ratio (SBR) and hence the limit of detection. Dual pulse LIBS also seeks to achieve enhanced emission intensities and longer sustained emission with the aim of increasing the signal level and ideally signal-to-noise ratio (SNR). The technique introduced in this section uses a 'reheating' laser in combination with the highly tunable stagnation layer with the aim of demonstrating that these enhancements may very well be possible. The key parameters studied are the effects of reheating on line intensities (corresponding to specific ion stages) and lifetimes of singly and doubly charged ion transitions, i.e. the spectral lines described above. The stagnation layer initialisation parameters are varied to change the shape and density of the 'fuel' plasma (i.e. the plasma to be reheated), and the plasma is reheated at a range of delay times.

When a laser interacts with a plasma, the laser radiation is absorbed by a process known as inverse bremsstrahlung (IB). The absorption coefficient [12] is given in subsection 1.3.2, and reproduced here for the reader's convenience:

$$K = 2^5 e^4 \left(\frac{2c^2\pi}{k_b m_e}\right)^{3/2} \frac{z^2 n_e^2 n_c ln\Lambda}{\omega_L} \left(\omega_L^2 - \omega_p^2\right)^{-1/2} \tag{4.5}$$

where e is the charge of the electron, c is the speed of light in vacuum, k_b is Boltzmanns constant, m_e is the mass of the electron, n_c is the critical density for the laser pulse wavelength, n_e is the electron number density, z the degree of ionisation of the ions in the plasma, ω_L is the frequency of the incoming laser pulse radiation, lnΛ is the Coulomb logarithm (equation 1.6) and ω_p is the plasma frequency (related to the electron density, see equation 1.4). The absorption coefficient is a strong function of the electron density no less so when one considers that above the critical density, this quantity takes the form of a reflection coefficient as the laser light is scattered from the critical density layer. Upon absorption of the laser energy, enhancement of electron kinetic energy occurs, increasing the collision frequency. The ions become more excited and more highly ionised, resulting in enhanced intensities and lifetimes of spectral lines.

Figure 4.21 shows time resolved imaging of a reheated tin stagnation layer generated by colliding two 50 mJ of duration 4 ns FWHM, 532 nm seed plasmas at a distance of 1.3 mm on a 140^0 wedge target together, and reheating with a 340 mJ, 6 ns, 1064 nm laser pulse, which propagates through the interaction region 120 ns after seed initialisation. When compared with figure 4.3 on page 88, it can be seen that reheating has a significant effect on both emission intensities and emission lifetimes. If figure 4.21 (f) is compared to figure 4.3 (i), both of which were acquired 290 ns after seed initialisation at an intensifier gain setting of 4000, the intensity gain by reheating becomes apparent. In figure 4.3 (i), emissions are minimal and peak at around 2000 counts, whereas in figure 4.21 (f), emissions from the layer are still quite intense, peaking at over 2×10^4 counts. At 440 ns after seed initialisation, i.e. figure 4.21 (i), the reheated stagnation layer emission levels have decreased to a level similar to those at 290 ns without the reheating laser pulse.

The method described in section 4.2.1 above is used to study the effects of reheating a stagnation layer. An example of this effect is shown by plotting

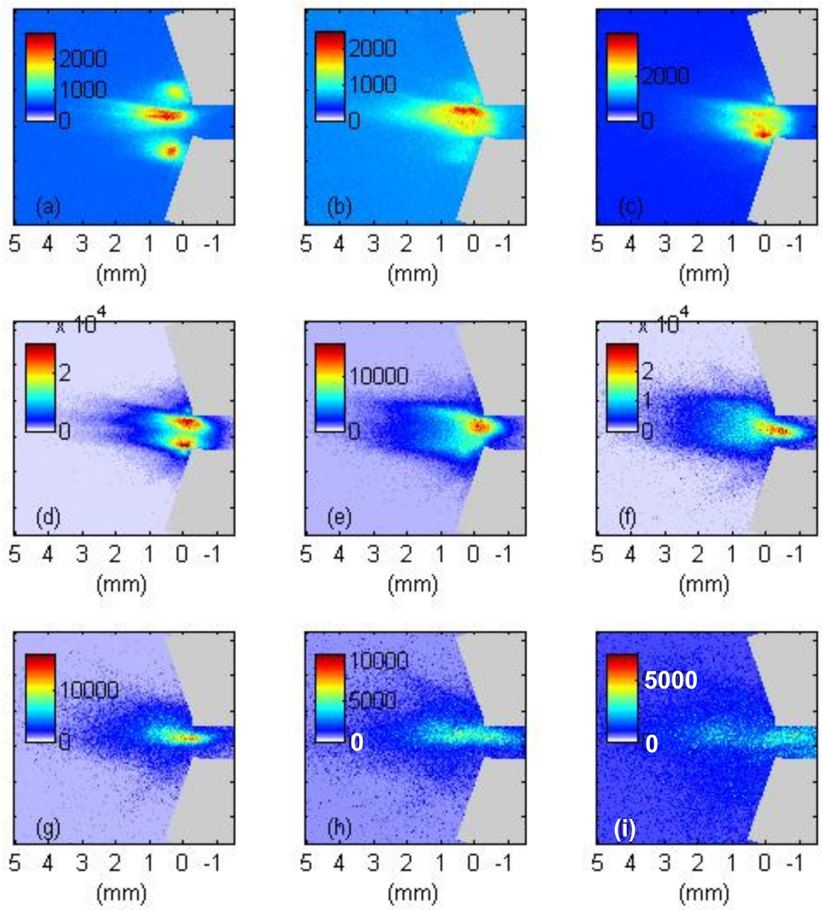

Figure 4.21: **Time resolved broadband emission imaging of a reheated tin stagnation layer created on a wedge target acquired at times (a) 120 ns, (b) 150 ns, (c) 180 ns, (d) 210 ns, (e) 260 ns, (f) 290 ns, (g) 340 ns, (h) 390 ns, &(i) 440 ns. Images (a), (b) & (c) were acquired at an intensifier gain setting of 1500, (d) and (e) were acquired at a setting of 3000, and (f), (g), (h) & (i) were acquired at a setting of 4000. The interpulse delay was 120 ns.**

the lineouts of the 485 nm Sn III line as a function of time, without and with reheating, as in figures 4.22 & 4.23 respectively. Again, it is apparent that reheating has a significant effect on both the intensity and lifetime of the emission line. This effect is best represented by measuring the spatially integrated areas of each line as a function of time.

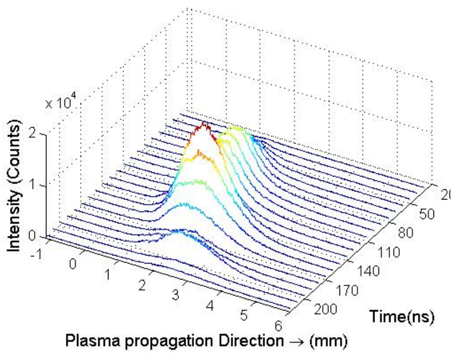

Figure 4.22: **Intensity trace of 485nm SnIII line in a stagnation layer generated by creating two seed plasmas with a 532 nm laser at a distance of 1.3 mm apart on a 140^0 wedge target as a function of time**

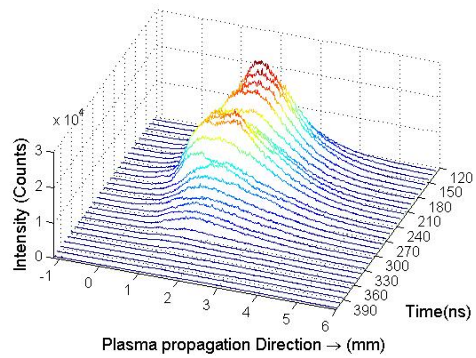

Figure 4.23: **Intensity trace of the same 485nm SnIII line in a stagnation layer which has been reheated 120 ns after seed initialisation using a 340 mJ 1064 nm laser pulse.**

4.3.1 Reheating the Stagnation Layer generated using Differing Seed Laser Wavelengths

Presented in figures 4.24 & 4.25 are the results of the experiment to reheat the stagnation layer generated by colliding two 50 mJ pulses of duration 4 ns FWHM, 532 nm seed plasmas at a distance of 1.3 mm on a 140^0 wedge target together, and reheating with a 340 mJ of duration 6 ns FWHM, 1064 nm laser pulse.

Figure 4.24 shows the effects of varying the interpulse delay from 40 ns to 240 ns (in steps of 40 ns), as well as the spatially integrated intensities as a function of time without reheating. It can be seen that the intensity of the 485 nm line is almost doubled by reheating at 80 ns, with a similar result at 120 ns. Referring to figure 4.11, it can be seen that the density reaches a maximum within this time window. Reheating at later times significantly increases the lifetime of the plasma. Not shown here is the case for the 492 nm line, since it is the same ion stage and carries the same information.

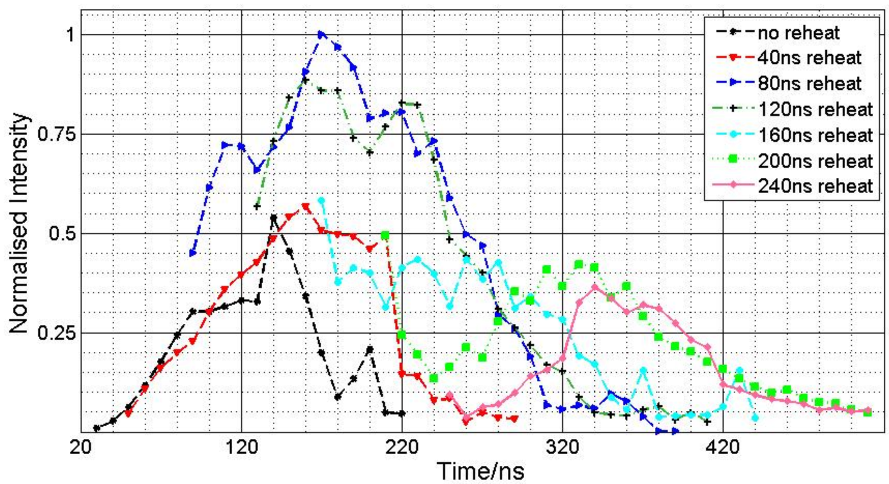

Figure 4.24: **Spatially integrated intensities of the SnIII 485 nm line of a stagnation layer created using a 532 nm, 4 ns FWHM laser pulse on a** 140^0 **wedge target for various reheat times, as a function of time.**

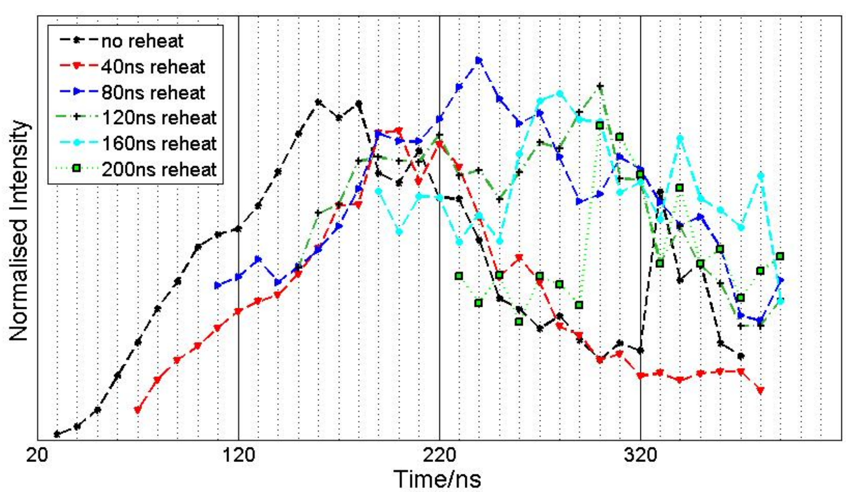

Figure 4.25: **Spatially integrated intensities of the SnII 645 nm line of a stagnation layer created using a 532 nm, 4 ns FWHM duration laser pulse on a** 140^0 **wedge target for various reheat times, as a function of time.**

Figure 4.25 shows the integrated intensities of the SnII 645 nm line due to reheating. Interestingly, the arrival of the reheat laser pulse initially suppresses the emission intensities, at least for short time delays and hence early into the life cycle of the stagnation layer. In particular, in the case of the reheat pulse after a 40 ns delay the layer is just being formed and so absorption of the laser pulse is weak because of the low density at this stage. The singly charged ions that are present at this stage are most likely ionised to higher states causing the intensity to drop. As time progresses the higher ion stages recombine to Sn^{+} ions and the line emissions again match those of the layer without a reheating laser pulse. At later reheat pulse time delays, emissions quickly increase to match the unreheated case, and the emission durations are longer. The density is increased and so the layer is more suitable for laser energy absorption, and radiates for longer.

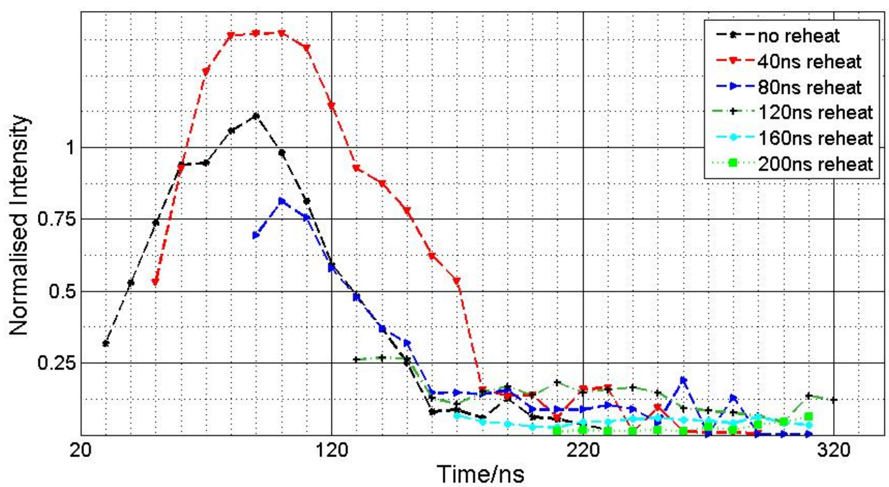

Figure 4.26: **Spatially integrated intensities of the SnIII 485 nm line of a stagnation layer created using a 1064 nm, 6 ns laser pulse on a** 140^0 **wedge target for various reheat times, as a function of time.**

Figure 4.26 & 4.27 show the results of the experiment to reheat the stagnation layer generated by colliding two 80 mJ in 6 ns, 1064 nm seed plasmas at a distance of 1.3 mm on a 140^0 wedge target together, and reheating with a 340 mJ in 6 ns, 1064 nm laser pulse.

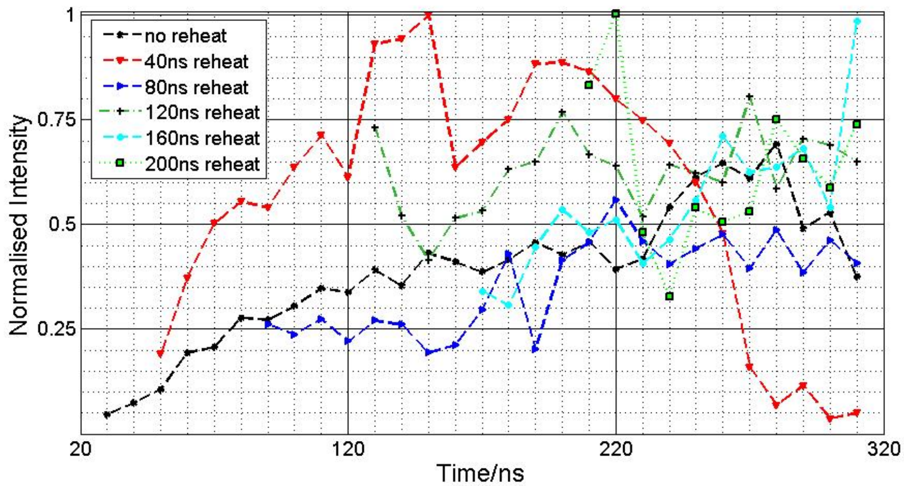

Figure 4.27: **Spatially integrated intensities of the SnII 645 nm line of a stagnation layer created using a 1064 nm, 6 ns laser pulse on a 140^0 wedge target for various reheat times, as a function of time.**

For the case of seed initialisation with a 1064 nm laser pulse, the seed plasmas are hotter (the temperature scales with the laser irradiance I ($W.cm^{-2}$) as $I^{0.6}$, equation 4.2) and so the emission of the layer without reheating is already of shorter duration than 532 nm. If we look first at the Sn^{2+} ions case, we can see that the seeds and therefore the layer are of lower density, thus only at early times will there be any chance that the density will reach that needed to absorb a decent fraction of the main pulse. Of course initially this will drive neutral Sn atoms to Sn^{+}, Sn^{+} ions to Sn^{2+} and especially here Sn^{2+} to Sn^{3+} and higher (reducing Sn^{2+} emission) immediately after arrival of the main pulse. Since the 1064 nm seeds are hot and lead to a stagnation layer that is formed quickly, all processes from formation to decay are hastened resulting in a weak and dilute layer at relatively early times. By 100 ns the layer is so dilute that the reheating 1064 nm pulse just passes through it with little or no absorption.

Figure 4.27 shows the effects of the reheat laser on the 645 nm line, representing the Sn^{+} ions. Once again only reheating with a 40 ns interpulse delay shows significant signal increase, as the density is only high enough at this delay to get decent laser-plasma coupling leading to an increase in electron-atom collisions and hence ionisation from neutral Sn to singly ionised Sn^{+}. For the interpulse delay of 80 ns there is still some coupling but it is most likely driving the stagnation layer to higher charge states, resulting in a decrease in emission intensities. For longer interpulse delays there is an increase in Sn^{+} emission as time progresses, which is quite different to the Sn^{2+} case. Here the higher charge states in collision with electrons experience electron capture and so the $Sn^{3+} + e^{-} \Rightarrow Sn^{2+}$ followed by $Sn^{2+} + e^{-} \Rightarrow Sn^{+}$ etc., as time progresses.

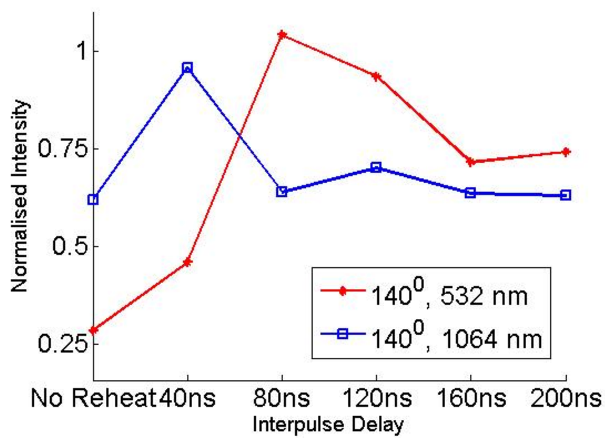

Figure 4.28: **Spatially & temporally integrated intensities of the SnIII 485 nm line of a stagnation layer created using different wavelengths for various reheat time delays.**

Figures 4.28 & 4.29 show both the spatially and temporally integrated intensities, i.e. the total line emission yield of both lines under examination, as a function of interpulse delay. Looking first at the Sn^{2+} case for a layer created by two 1064 nm laser pulses, there is a peak in emission intensity for a 40 ns pulse delay, and the total emission yield for all later times is very similar to the case without reheating. This was noted earlier; the density of the relatively low density high temperature plasma peaks early, allowing for absorption of the reheat laser pulse at this interpulse delay only. For the 532 nm seeds case, the reheating laser has a large effect at all times, driving the total emission yield to 4× that without a reheat laser pulse, at an 80 ns delay. Looking at the emissions from the singly charged ions, there is

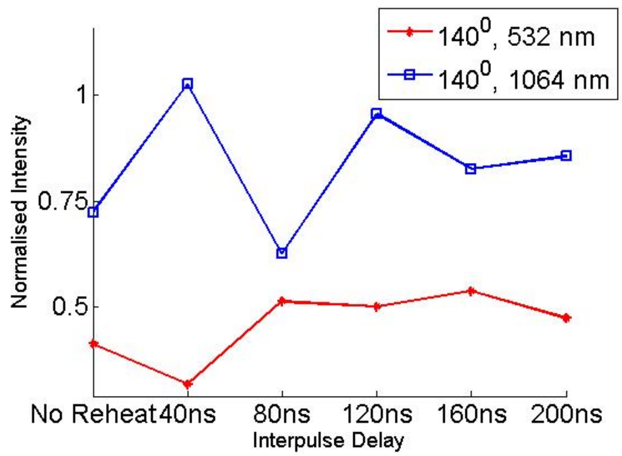

Figure 4.29: **Spatially & temporally integrated intensities of the SnII 645 nm line of a stagnation layer created using different wavelengths for various reheat time delays.**

a peak again at 40 ns interpulse delay for the case of the 1064 nm seeds. For the 532 nm seed case, the 40 ns interpulse delay exhibits a decrease in emissions, due to ions being driven to Sn^{2+} etc. The longer interpulse delays don't increase the emission signal significantly, although the Sn^{2+} signal is increased significantly, again due to the singly charged ions being driven to higher states.

4.3.2 Reheating the Stagnation Layer Generated using a Range of Target Wedge Angles

The shape and density of the stagnation layer can be controlled further in order to optimise emission intensities and lifetimes by varying the wedge target angle. The experiment was repeated for three further wedge angles; 80^0, 100^0 & 180^0.

Figures 4.30, 4.31 & 4.32 show the effects on the 485 nm SnIII spectral line of reheating the stagnation layer created using a 532 nm 4 ns FWHM duration laser pulse on a 80^0, 100^0 & 180^0 wedge target respectively. The reheat laser pulse was 340 mJ in 6ns at 1064 nm in each case. Also, the intensities in the three plots are normalised to the peak intensity for the 80^0 wedge case, illustrating the very significant difference in emission intensity by changing

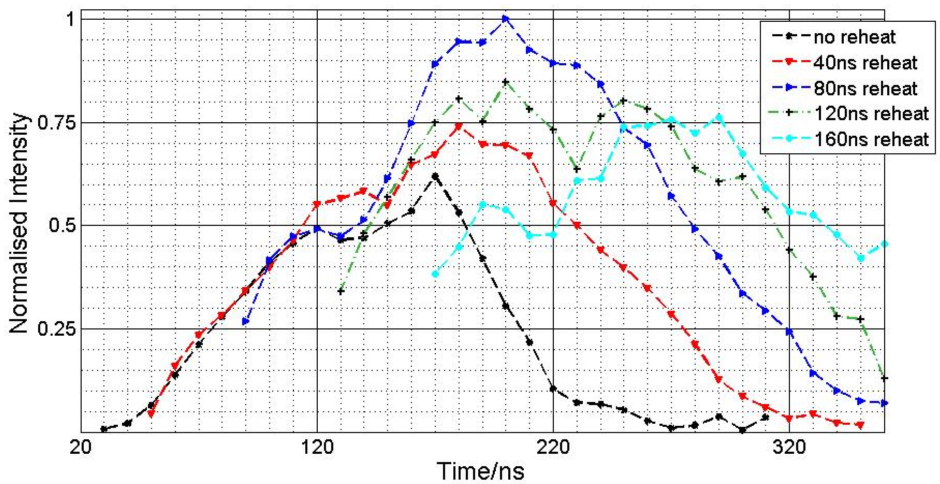

Figure 4.30: **Spatially integrated intensities of the SnIII 485 nm line of a stagnation layer created using a 532 nm, 4 ns FWHM duration laser pulse on a** 80^0 **wedge target using various reheat times, as a function of time.**

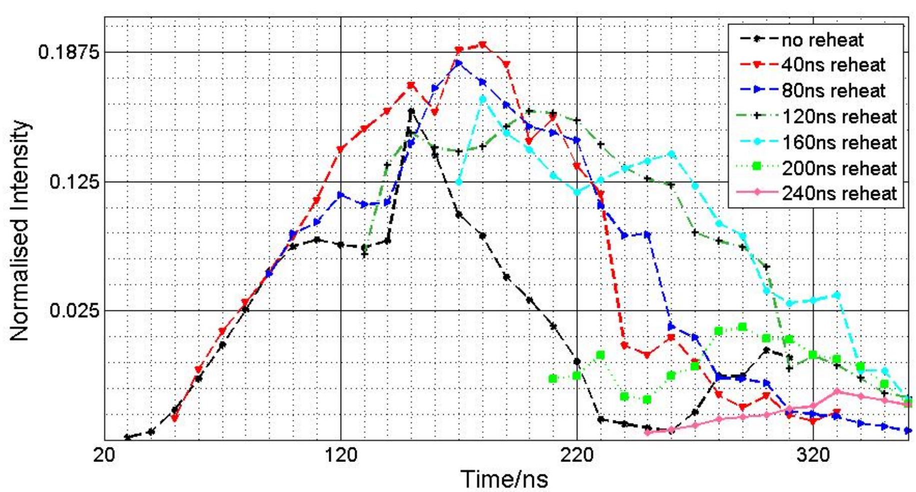

Figure 4.31: **Spatially integrated intensities of the SnIII 485 line of a stagnation layer created using a 1064 nm, 6 ns laser pulse on a** 100^0 **wedge target for various reheat times, as a function of time.**

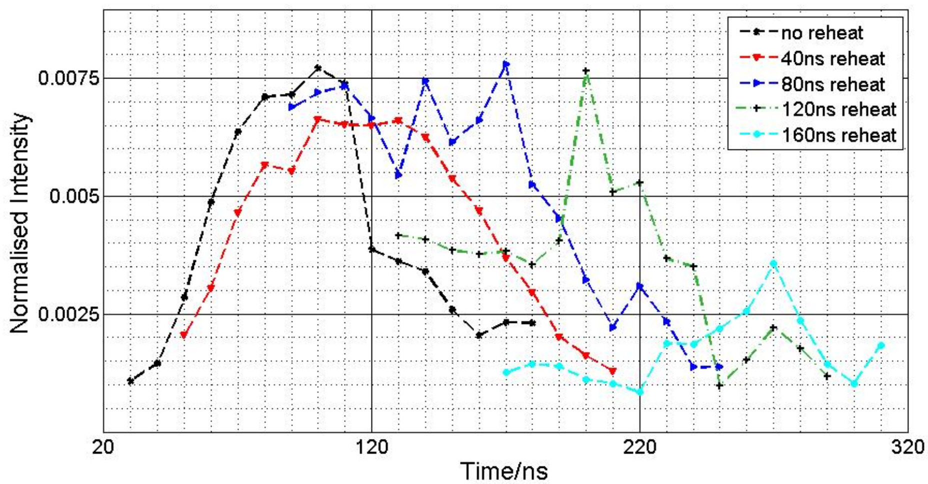

Figure 4.32: **Spatially integrated intensities of the SnIII 485 nm line of a stagnation layer created using a 1064 nm, 6 ns laser pulse on a 180^0 wedge target for various reheat times, as a function of time.**

the target wedge angle. Reheating too, differs greatly depending on wedge angle. To understand these phenomena, one must consider (i) the density distribution throughout the stagnation layer, (ii) the shape and size of the plume, and (iii) the formation of the plume, which occurs at a time which depends on the seed plasma velocity both parallel and orthogonal to the collision plane. For single plasma plumes (seeds) it is well known that the velocity normal to the target surface is higher than that orthogonal to the surface [3], and so the wedge angle for a fixed laser beam direction will result in different formation times and stagnation layer characteristics.

The results from the 80^0 wedge show that reheating of the stagnation layer even at later stages has a significant effect on both the intensity and duration of the spectral line emission. The plasma is highly confined due to the target geometry and the underlying stagnation layer plasma density remains high even after emission intensities have decreased. Note that the emission durations are increased in both the 100^0 & the 180^0 cases, although intensity increases are minimal, and decrease slightly in the 180^0 case.

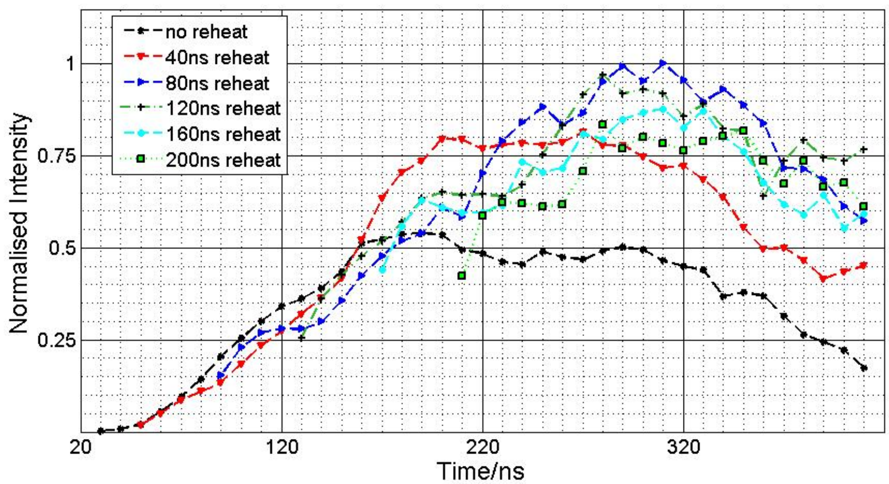

Figure 4.33: **Spatially integrated intensities of the SnII 645 nm line of a stagnation layer created using a 532 nm, 4 ns FWHM duration laser pulse on a 80^0 wedge target for various reheat times, as a function of time.**

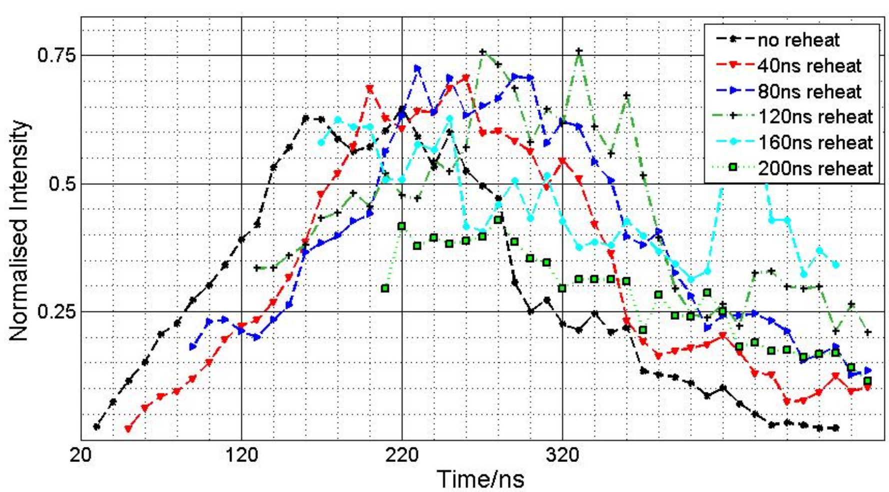

Figure 4.34: **Spatially integrated intensities of the SnII 645 nm line of a stagnation layer created using a 532 nm, 4 ns FWHM duration laser pulse on a 100^0 wedge target for various reheat times, as a function of time.**

Figures 4.33, 4.34 & 4.35 show the effects on the 645 nm SnII spectral line of reheating the stagnation layer created using a 532 nm 4 ns FWHM duration laser pulse on a 80^0, 100^0 & 180^0 wedge target respectively. For the 80^0 case one can see that the slowly evolving but higher density SL formed by 532 nm seeds shows higher Sn^+ emission at later times as expected. Sn^+ ions are formed at early times in the no reheat case due to electron-ion recombination. Such recombination processes later lead to neutral atomic Sn, which is still tightly confined in the layer. This provides the fuel for the interdelay pulse, which ionises the neutral atoms, increasing emission intensities and durations of the Sn^+ ions.

In the 100^0 case (figure 4.34) the stagnation is likely to be softer with a more extended stagnation layer, and a concomitantly lower SL plasma density at all time delays. It can be seen that emission from the layer without a reheating pulse tails off much more rapidly than in the 80^0 case, albeit the peak intensity remains similar to the 80^0 case. Figure 4.35 shows similar results to the 100^0 case, although the intensities are much lower. The density is similar but the volume is lower due to the target geometry.

For both cases, it is clear that reheating at short interpulse delays reduces the Sn^+ signal as the Sn^+ fraction is reduced. Laser induced ionisation drives the dominant ion stage higher than Sn^+. At later times the neutral atomic Sn dominates and so laser ionisation increases the Sn^+ signal except for very long time delays where the SL plasma becomes so dilute as to be almost transparent to the reheating laser field.

Looking at the effect of reheating on the SnII 645 nm line of the stagnation layer, it can be seen that there is a general increase in both emission intensities and lifetimes for the 80^0 wedge target system, where reheating works almost equally well at later times as it does earlier times (peaking at an interdelay pulse of around 80 ns, where double the intensity was recorded). The increases are not so pronounced in either the 100^0 or the 180^0 case, where the main contribution of reheating is to an increase in emission duration.
Figures 4.36 & 4.37 show the total line emission yield of both lines under examination, as a function of interpulse delay. As expected, the yield from the 80^0 case is by far the highest for both lines (the 645 nm line is not shown for the 80^0 case, but based on a comparison of figures 4.33 & 4.34, a significantly higher yield than the 100^0 case etc. is expected). There is more than $3\times$

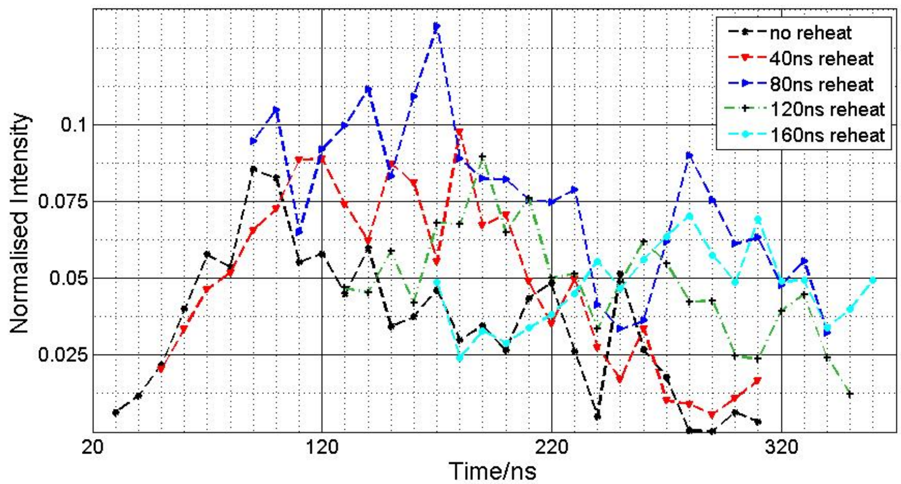

Figure 4.35: **Spatially integrated intensities of the SnII 645 line of a stagnation layer created using a 532 nm 4 ns FWHM duration laser pulse on a** 180^0 **wedge target using various reheat times, as a function of time.**

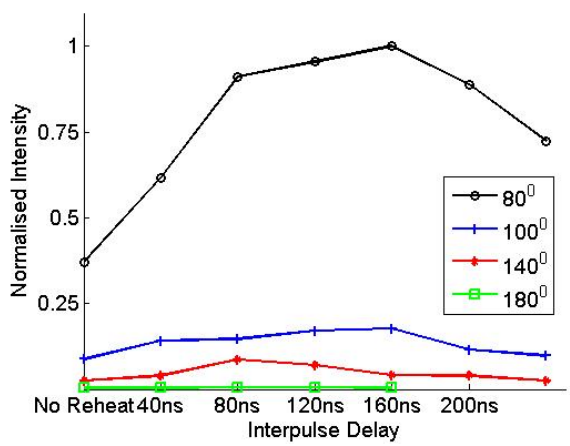

Figure 4.36: **Spatially & temporally integrated intensities of the SnIII 485 nm line of a stagnation layer created using various target wedge angles for various reheat time delays.**

intensity yield of the 485 nm line when reheated with an interpulse delay

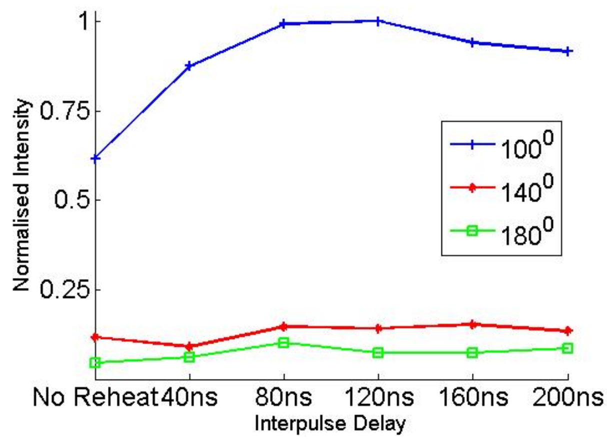

Figure 4.37: **Spatially & temporally integrated intensities of the SnII 645 nm line of a stagnation layer created using various target wedge angles for various reheat time delays.**

of 160 ns, due to a combination of higher intensities and longer durations. For each of the other cases the reheat laser generally increases yields, with the maximum yield due to an interpulse delay of between 80 and 160 ns. Reheating has the effect of increasing yields of the SnII line, although the effects are not as significant as the SnIII case, due to a large portion of singly charged ions being ionised to higher states by the process.

4.3.3 Background Reductions

For application in LIBS the signal-to-background ratio or SBR is a key parameter. Increasing the SBR increases the LIBS limit-of-detection or LOD since the LOD is given by the expression:

$$LOD = (3 \times \sigma_{background})/S \tag{4.6}$$

where $\sigma_{background}$ is the standard deviation of the background component of the spectrum with the lowest concentration of analyte, and S is the slope of the calibration curve. This is justified by the assumption that, in a calibration curve (i.e. the intensity or line ratio plotted versus the concentration of analyte) with slope S, any x value (elemental concentration) can be obtained by dividing the intensity by the slope at a certain point $y/(y/x)) = x$. When

the value of $3 \times \sigma_{background}$ is substituted for the intensity of the analytical line, the limit of detection is calculated. In the current context, we aim to demonstrate the increased signal to background ratio by implementing the method described.
Figure 4.38 shows the time resolved spectra which include the SnIII 485 nm and 492 nm spectral lines of a tin stagnation layer created on an 80^0 wedge target acquired at a range of time delays and for two different interpulse delay settings. Comparing 4.38 (a), (b) & (c) which were produced without a reheating pulse, to (d), (e) & (f) which were taken at the same time delay and with an inter-pulse delay propagating 80 ns after the seed pulse, and to (h), (i) & (j) which were acquired with an interdelay pulse propagating 120 ns after the seed pulse, it can be seen that the increase in continuum is minimal in all cases. However, the increase in line intensity emissions has been shown (figure 4.30) to be significant. The benefit of increased emission lifetimes is demonstrated in figure 4.38 (g), where the background signal is minimal and emissions are still at a high level. The SBR is improved by up to 170% and 195% for the SnIII and SnII lines when using the 80^0 wedge.

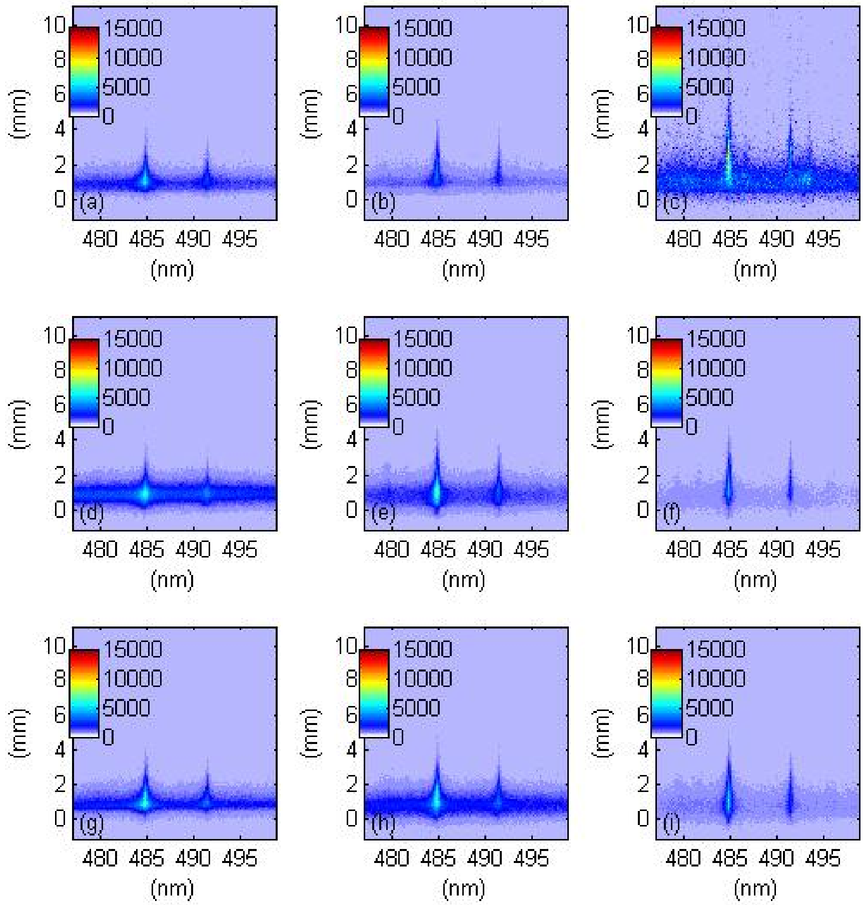

Figure 4.38: **Time resolved emission spectroscopy of a tin stagnation layer created on an 80^0 wedge target acquired at times (a)120 ns, (b)180 ns & (c)240 ns, without reheating, at times (d)120 ns, (e)180 ns & (f)240 ns with reheating interpulse delay of 80 ns, and at times (g)120 ns, (h)180 ns, &(i)240 ns with interpulse delay of 120 ns. All images were acquired at an intensifier gain setting of 2000, apart from (c) which was acquired at a setting of 3000.**

4.4 Summary

In this chapter we introduced a novel method to increase the emission line intensity from a laser plasma by the formation of a stagnation layer that was reheated in a double pulse formation-excitation configuration. For the first time it was demonstrated that pumping of the stagnation layer causes an increase in emission intensity and duration of spectral lines within the layer.

Furthermore, the effects of reheating were compared for various target geometric systems, and for various interpulse delays. It was found that although opacity began to have a noticeable effect when the 80^0 target system was employed, reheating of the stagnation layer created by this system are by far the most significant. Maximum emission yields were achieved when an interpulse delay of 80 or 120 ns was used, although optimal delay times were found to vary depending on the ion stage under consideration.

The modification of the dual pulse configuration is suggested as an enhancement to the benefits of the target geometries studied in chapter 3, with possible applications in LIBS, fundamental atomic physics studies, and enhanced emission from laser plasma light sources. It was shown that a 'reheating' laser significantly enhances both the emission intensities and lifetimes of spectral lines representing singly and doubly charged ion transitions in a tin plasma. By varying the angle of the target wedge and the seed laser wavelength, conditions of the interaction region between two colliding plasmas were altered. Time resolved emission imaging and spectroscopy were employed to study the effects of reheating this stagnation layer at a range of interpulse delays, and close to doubling of both the spatially integrated emission intensities and lifetimes of the plasma was achieved.

References

[1] E.H. Piepmeie and H.V. Malmstad. Q-switched Laser Energy Absorption In Plume Of An Aluminum Alloy. *Analytical Chemistry*, 41(6): 700–&, 1969. ISSN 0003-2700. doi: {10.1021/ac60275a014}.

[2] V. I. Babushok, F. C. DeLucia, Jr., J. L. Gottfried, C. A. Munson, and A. W. Miziolek. Double pulse laser ablation and plasma: Laser induced breakdown spectroscopy signal enhancement. *Spectrochimica Acta Part B-Atomic Spectroscopy*, 61(9):999–1014, SEP 2006. ISSN 0584-8547. doi: {10.1016/j.sab.2006.09.003}.

[3] J. Dardis and J. T. Costello. Stagnation layers at the collision front between two laser-induced plasmas: A study using time-resolved imaging and spectroscopy. *Spectrochimica Acta Part B-Atomic Spectroscopy*, 65(8, SI):627–635, AUG 2010. ISSN 0584-8547. doi: {10.1016/j.sab.2010.03.005}. 5th Euro-Mediterranean Sympsoium on Laser Induced Breakdown Spectroscopy, Rome, Italy, Sep 28-Oct 01, 2009.

[4] S.L. Gupta, P.K. Pandey, and R.K. Thareja. Dynamics of laser ablated colliding plumes. *Physics Of Plasmas*, 20(1), JAN 2013. ISSN 1070-664X. doi: {10.1063/1.4789860}.

[5] W. Sdorra, J. Brust, and K. Niemax. Basic Investigations For Laser Microanalysis .4. The Dependence On The Laser Wavelength In Laser Ablation. *Mikrochimica Acta*, 108(1-2):1–10, 1992. ISSN 0026-3672. doi: {10.1007/BF01240366}.

[6] G. Abdellatif and H. Imam. A study of the laser plasma parameters at different laser wavelengths. *Spectrochimica Acta Part B-Atomic Spectroscopy*, 57(7):1155–1165, JUL 31 2002. ISSN 0584-8547. doi: {10.1016/S0584-8547(02)00057-5}. 1st Euro-Mediterranean Symposium on Laser-Induced Breakdown Spectroscopy, Cairo, Egypt, NOV 02-06, 2001.

[7] D. Colombant and G.F. Tonon. X-Ray-Emission in Laser-Produced Plasmas. *Journal OF Applied Physics*, 44(8):3524–3537, 1973. ISSN 0021-8979.

[8] D. Salzmann. *Atomic Physics in Hot Plasmas.* Oxford University Press, New York, 1998.

[9] P. Hough, C. McLoughin, T. J. Kelly, P. Hayden, S. S. Harilal, J. P. Mosnier, and J. T. Costello. Electron and ion stagnation at the collision front between two laser produced plasmas. *Journal of Physics D: Applied Physics*, 42(5):055211, 2009. URL http://stacks.iop.org/0022-3727/42/i=5/a=055211.

[10] C. Ursu, S. Gurlui, C. Focsa, and G. Popa. Space- and time-resolved optical diagnosis for the study of laser ablation plasma dynamics. *Nuclear Instruments & Methods In Physics Re- Search Section B-Beam Interactions With Materials And Atoms*, 267(2):446–450, JAN 2009. ISSN 0168-583X. doi: {10.1016/j.nimb.2008.10.057}. 4th Conference on Elementary Processes in Atomic Systems, Clu Napoca, Romania, JUN 18-20, 2008.

[11] N. Konjevic, A. Lesage, J.R. Fuhr, and W.L. Wiese. Experimental stark widths and shifts for spectral lines of neutral and ionized atoms (A critical review of selected data for the period 1989 through 2000). *Journal Of Physical And Chemical Reference Data*, 31(3):819–927, SEP 2002. ISSN 0047-2689.

[12] S. Eliezer. *The interaction of high-power lasers with plasmas.* Series in plasma physics. Institute of Physics Publishing, Bristol, Philadelphia, 2002. ISBN 0-7503-0747-1. URL http://opac.inria.fr/record=b1133708.

Chapter 5

Conclusions & Outlook

In this final chapter, a summary of the results obtained during the project and an outlook for the future of the dual-pulse technique introduced in this thesis is given. Potential applications and suggestions for follow-on experiments are made.

5.1 Conclusions

The work presented in this thesis was divided into two main segments. The first was concerned with the properties of a stagnation layer created by colliding two laser produced plasmas and the effects of the initialisation parameters on those properties. The second involved the introduction of a novel technique to reheat the stagnation layer with a separate laser pulse, and its effects on the optical emission from that layer.

In chapter 3 the spatial distribution of different plasma species in the stagnation layer produced by colliding two copper plasmas was examined. It was found that the stagnation layer growth depends on the seed plasma plume velocities and the growth rate of each atomic or ionic 'fluid' within those seeds. The spatial distribution as a function of time as well as the ratio of velocities of both atoms and ions within the stagnation layer was found to vary as a function of the wedge angle in the target system. For the case of the 100^0 wedge the stagnation layer is highly confined allowing for little movement of the neutral species. When two ion stages were compared in chapter 4 it was shown that the 'velocities' of singly and doubly charged ions did not vary significantly.

In chapter 2 we described an experimental setup that could utilise a new camera system to monitor the plasma via broadband imaging while simultaneously recording spectra. Along with the rotating target geometry setup that provided fresh material for ablation, this method allowed for large amounts of data to be recorded. The programmes described were able to handle these large amounts of data and extract temperatures and densities, as well as optical time-of-flight results.

The temperature and density distributions were determined for the copper stagnation layer described in chapter 3, which revealed that the temporal gradients of each were gentle compared with the single plume results. The more confined layer was shown to have a higher temperature and electron density, as well as a longer emission lifetime.

The high continuum, common presence of self-absorption, and short duration of single pulse laser produced plasmas require that better optical emission sources be developed [1] for laser induced breakdown spectroscopy (LIBS). The dual-pulse LIBS technique shows much promise in overcoming these problems, and many configurations have been explored [2]. However, to date the highly tunable properties of the stagnation layer demonstrated in chapter 3 have heretofore not been utilised for such a purpose.

The use of a tin stagnation layer as the fuel to be reheated by a second laser was described in chapter 4. This is the first time that coupling of laser energy to a stagnation layer was achieved, and significant effects were observed. The stagnation layer properties were controlled using techniques described in chapter 3, and the emission intensity and duration of spectral lines created by transitions in singly and doubly charged ions were recorded. Although the presence of opacity was observed using lower angle target systems, the emission yields were highest here. The stagnation layer was pumped with a reheating laser, which demonstrated for the first time that the stagnation layer could absorb laser energy, and emission yields were increased considerably. The delay between the seed laser pulse and the reheating pulse was varied to find optimal settings. The maximum yield was attained by reheating the stagnation layer created on an 80^0 wedge target system, with an interpulse delay of between 80 & 120 ns.

5.2 Outlook

The work presented in this thesis indicates that manipulation of the target systems of colliding laser produced plasmas has significant potential for both fundamental studies of plasma collisions and applications. However, there remains a large amount of systematic studies on the properties of the stagnation layer as a function of the target geometry. The response of some of the parameters of the stagnation layer, such as temperature, density, spatial distribution and temporal evolution etc. has been studied but there are many parameters (e.g. target material, laser pulse duration, energy, wavelength etc.) remaining to be varied and stagnation layer properties to be measured. Such systematic and fundamental studies are vital to the progression of colliding plasmas from preliminary investigations in the laboratory (as is the case currently) to being utilised for further applications. They can also provide a valuable reference for designing future experiments/applications. In addition, any next phase of the work will require the extension of existing models such as the multifluid approach [3] to the parameter range of relevance here.

The reheating of the stagnation layer has been presented in the context of LIBS, where in-depth investigations are needed in order to realise fully these ambitions for the technique introduced. For example, studies on the relevant materials and conditions must be carried out, as well as the response of the system in the vacuum ultra-violet (VUV) , which has inherent advantages over visible wavelength LIBS [4].

Reheating the stagnation layer has promise in further applications; including the potential to increase conversion efficiency in tin plasmas for EUVL by creating relatively low density - high energy plasmas which can overcome the problem of EUV flux loss due to opacity while maintaining high brightness. In simple terms, while the emitted flux increases linearly with excited species number density, the opacity increases exponentially with ground state number density and so flux optimisation involves managing the tradeoff between these two by determining the optimum density and temperature.

Further applications include the improvement and development of a general array of laser produced plasma spectroscopy techniques, in particular, the reduction of opacity in laser produced Hi-Z (or high atomic number) plasmas where under normal conditions one observes predominantly continuum emission. For many applications, but especially plasma diagnostics, the underlying line emission is needed. By reducing opacity, line emission is enhanced.

In conclusion, the project has revealed some interesting findings into the properties of both the stagnation layer and the reheated stagnation layer. Preliminary experiments have shown that there is potential to utilise the reheated stagnation layer as a configuration in dual-pulse LIBS. Two manuscripts based on each of chapters 3 & 4 are currently under preparation.

References

[1] C. Gautier, P. Fichet, D. Menut, J.L. Lacour, D. L'Hermite, and J. Dubessy. Quantification of the intensity enhancements for the double-pulse laser-induced breakdown spectroscopy in the orthogonal beam geometry. *Spectrochimica Acta Part B-Atomic Spectroscopy*, 60(2):265–276, FEB 28 2005. ISSN 0584-8547. doi: {10.1016/j.sab.2005.01.006}.

[2] V. I. Babushok, F. C. DeLucia, Jr., J. L. Gottfried, C. A. Munson, and A. W. Miziolek. Double pulse laser ablation and plasma: Laser induced breakdown spectroscopy signal enhancement. *Spectrochimica Acta Part B-Atomic Spectroscopy*, 61(9):999–1014, SEP 2006. ISSN 0584-8547. doi: {10.1016/j.sab.2006.09.003}.

[3] P.W. Rambo and R.J. Procassini. A Comparison Of Kinetic And Multifluid Simulations Of Laser-Produced Colliding Plasmas. *Physics Of Plasmas*, 2(8):3130–3145, AUG 1995. ISSN 1070-664X. doi: {10.1063/1.871145}.

[4] V. Sturm, L. Peter, and R. Noll. Steel analysis with laser-induced breakdown spectrometry in the vacuum ultraviolet. *Applied Spectroscopy*, 54(9):1275–1278, SEP 2000. ISSN 0003-7028. doi: {10.1366/0003702001951183}.

List of Tables

1.1 Classification of the main atomic processes in a laser-produced plasma ($B \rightleftharpoons B$: bound-bound, $B \rightleftharpoons F$: bound-free, and $F \rightleftharpoons F$: free-free) 9

2.1 Specifications of the Surelite laser systems 31

3.1 Velocity* of peak of intensity of neutral emitting atoms and ions. 60

3.2 Wavelength, upper level energy, upper level degeneracy and transition probability [14] for the Cu I emission lines used in the Boltzmann plot. 68

List of Figures

1.1 Schematic representation of the interaction of a high power laser pulse with a solid target [23]. 5
1.2 (a) Electron impact excitation and (b) de-excitation 10
1.3 (a) Spontaneous decay and (b) resonant photoabsorption 11
1.4 (a) Electron impact ionisation and (b) three-body recombination 12
1.5 (a) Photoionisation and (b) radiative recombination 12
1.6 (a) Bremsstrahlung and (b) inverse bremsstrahlung 13
1.7 Autoionisation (a) and (b) dielectronic recombination 14
1.8 Sn ion fractions as a function of electron temperature (T_e), using the Colombant & Tonon CR model 17
1.9 Electron density and temperature ranges for applicability of LTE, CE and CR models [30] 18

2.1 Photograph of the experimental system used for generation and optical diagnostics of colliding plasmas. 30
2.2 (a) Schematic drawing of the Surelite laser system. The harmonic generating optics shown as dashed lines are absent in the Surelite III but present in the Surelite I. (b) Photodiode trace of the 1064 nm pulse output. The full width at half maximum is 6 ns. 31
2.3 Schematic of the optical setup for creation of two colliding plasmas. 32
2.4 Fixed angle wedge target system for variation of seed plasma collision angles. A disc cut to the desired angle may be loaded for over 150 separate shots on a fresh target position each time. The alignment jig provides X, Y and θ movements. 33
2.5 Schematic drawing of the experimental system used for generation and reheating of colliding plasmas (not to scale). 34

2.6 The modified target setup to allow for propagation of the reheat laser pulse without the creation of a third seed plasma 34
2.7 The seed plasmas propagate normal to the target surface. If the target is shifted slightly, the plasmas will propagate towards the reheating laser, for maximum absorption. 35
2.8 Schematic drawing of the experimental setup for fast imaging of laser produced plasmas (not to scale). 36
2.9 Schematic drawing of the micro-channel plate of the iStar camera, from ref. [5]. 37
2.10 Plot of the $\log_{10}$ of averaged intensity versus gain setting for the iStar DH334T camera. 37
2.11 Schematic diagram of the emission imaging spectroscopy setup including imaging optics and dove prism. 38
2.12 Function of the dove prism. When the dove prism is added to the optical setup, expansion occurs along the length of the entrance slit of the spectrometer. 39
2.13 Grating efficiency curve for the 1200 grooves mm^{-1} supplied with the Chromex visible spectrometer, from ref [6]. 39
2.14 Timing diagram showing synchronisation of the lasers and the camera for reheating experiments. 40
2.15 Example of the Fityk program and it's determination of the peak of a curve. 45
2.16 Spectral image showing three neutral Cu transitions at 510.55nm, 515.32 & 521.82nm split into spatial regions (cf. Chapter 3). . . 46
2.17 The trace of 8 boxes from figure 2.16 after vertical binning is performed. 46
2.18 Flowchart of the suite of codes used to fit density profiles to multiple spectra. 46

3.1 Time integrated ($10\mu s$) images of the stagnation layer formed using 3 separate wedge angles: (a) 180^0 (b) 140^0 & (c) 100^0. . . . 52
3.2 Example time-integrated spectroscopic image of the stagnation layer generated by focussing two 105 mJ 6 ns laser pulses onto the 140^0 wedge system at a distance of D = 1.3 mm, in the wavelength region 502 nm-522 nm. 55
3.3 Motion of the peak intensity point of atomic copper (λ = 521 nm) in the stagnation layer. 56

3.4 **Motion of the peak intensity point of singly charged copper (λ = 508 nm) in the stagnation layer.** 56
3.5 **Comparison of the movement of the peak of intensity of neutral emitting atoms and ions in a stagnation layer generated by focussing two 105 mJ 6 ns laser pulses onto three different wedge systems.** 57
3.6 **Comparison of the movement of the peak of intensity of neutral emitting atoms and ions in a stagnation layer generated by focussing two 105 mJ 6 ns laser pulses at a distance of 1.3 mm & 2.6 mm apart.** 59
3.7 **Comparison of the movement of the peak of intensity of neutral emitting atoms and singly charged copper ions in a stagnation layer generated by focussing two 6 ns laser pulses of three distinct energies.** 59
3.8 **Spectral image showing the three neutral Cu transitions at 510.55nm, 515.32 & 521.82nm.** 62
3.9 **The trace of 8 boxes from figure 3.8 after vertical binning is performed.** 62
3.10 **Spatially resolved & time integrated electron density distributions in the stagnation layer generated by focussing two 105 mJ 6 ns laser pulses onto three target wedge angles.** 63
3.11 **Spatially & temporally resolved electron density distributions at the end of the stagnation layer furthest from the seed plasmas for three target wedge angles.** 64
3.12 **Time integrated electron density distributions along the stagnation layer for two seed plasma separations.** 65
3.13 **Time resolved electron density distributions along the stagnation layer at two different seed plasma separations.** 66
3.14 **Time integrated electron density distributions along the stagnation layer for three laser pulse energies.** 67
3.15 **Time resolved electron density distributions over the interaction region of three laser pulse energies.** 67
3.16 **Spectral image showing the neutral Cu transition at 465.11 nm.** 69
3.17 **Spectral image showing the neutral Cu transition at 578.21 nm.** 69
3.18 **Example of a Boltzmann plot to determine the temperature of a copper plasma constructed from the analysis of five lines and corresponding data points.** 69

3.19 **Spatially resolved & time integrated excitation temperature distributions along the stagnation layer for three target wedge angles.** 71
3.20 **Spatially resolved excitation temperature distributions for a range of time delays along the stagnation layer for three target wedge angles.** 72
3.21 **Spatially resolved & time integrated excitation temperature distributions along the stagnation layer for two seed plasma separations, namely 1.3 mm and 2.66 mm.** 73
3.22 **Spatially resolved excitation temperature distributions for a range of time delays along the stagnation layer for two different seed plasma separations, namely D = 13. mm and D = 2.6 mm.** 74
3.23 **Spatially resolved & time integrated excitation temperature distributions along the stagnation layer for three different laser pulse energies.** 75
3.24 **Spatially resolved excitation temperature distributions for a range of time delays along the interaction region for three pulse energies.** 75
3.25 **Comparison of the movement of the peak of intensity of neutral emitting atoms and ions for a single pulse plasma with a stagnation layer.** 77
3.26 **Comparison of the electron densities of a single pulse plasma with a stagnation layer.** 78
3.27 **Comparison of the excitation temperatures of a single pulse plasma with a stagnation layer.** 79

4.1 **(a) Time integrated broadband emission imaging of a reheated tin stagnation layer created on a** 140^0 **wedge target.** 85
4.2 **Ion fractions for a LPP generated using a 532 nm and a 1064 nm laser pulse at a fixed density of** 10^{18} **cm**$^{-3}$ 87
4.3 **Time resolved broadband emission imaging of a tin stagnation layer created on a wedge target acquired at times (a) 0 ns, (b) 40 ns, (c) 80 ns, (d) 120 ns, (e) 160 ns, (f) 200 ns, (g) 230 ns, (h) 260 ns, & (i) 290 ns. Images (a), (b) & (c) were acquired using an intensifier gain setting of 1500, (d) was acquired at a setting of 3000, and (e), (f), (g), (h) & (i) were acquired at a setting of 4000.** 88

4.4 **Time resolved emission imaging spectra of the 485 nm and 492 nm specrtral lines of a tin stagnation layer created on a wedge target acquired at times (a) 40 ns, (b) 60 ns, (c) 90 ns, (d) 120 ns, (e) 150 ns, (f) 180 ns, (g) 210 ns, (h) 240 ns, & (i) 270 ns. Images (a), (b), (c), (d), (e) & (f) were acquired using an intensifier gain setting of 2000, (g) & (h) were acquired at a setting of 3000, and (i) was acquired at a setting of 4000.** 89
4.5 **Time resolved broadband emission imaging of a tin stagnation layer created on a wedge target acquired at times (a)40 ns, (b)60 ns, (c)90 ns, (d)120 ns, (e)150 ns, (f)180 ns, (g)210 ns, (h)240 ns, &(i)270 ns. All images were acquired using an intensifier gain setting of 4000.** 91
4.6 **Time and space resolved plot of the spectral line emission along the stagnation layer for the doubly ionized Sn ions as tagged with the Sn III 485 nm line. It can be seen that the peak intensity point moves along the stagnation layer as time progresses.** 92
4.7 **Time and space resolved plot of the spectral line emission along the stagnation layer for the singly ionized Sn ions as tagged with the Sn II 645 nm line. It can be seen that the peak intensity point moves along the stagnation layer as time progresses.** . . . 92
4.8 **Comparison of the movement of the peak intensity position along the stagnation layer of emitting ions in a stagnation layer, Sn^{2+} (485 nm and 492 nm) and Sn^{+} (645 nm), for two different laser wavelengths.** 93
4.9 **Comparison of spatially integrated intensities of emitting Sn^{2+} and Sn^{+} ions in a stagnation layer created by seed plasmas generated with 1064 nm laser wavelength and by seed plasmas generated with 532 nm laser wavelength.** 94
4.10 **Comparison of spatially integrated intensities of emitting Sn^{+} ions in a stagnation layer created by seed plasmas generated with 1064 nm laser wavelength and by seed plasmas generated with 532 nm laser wavelength.** 95
4.11 **Electron density distributions of a stagnation layer created using two 532 nm seeds on a 140^0 wedge target.** 97
4.12 **Electron density distributions of a stagnation layer created using two 1064 nm seeds on a 140^0 wedge target.** 97

4.13 **Comparison of the peak density in a stagnation layer created by two 532 nm seeds and by two 1064 nm seeds as a function of time.** 98
4.14 **Electron density distributions of a stagnation layer created using a flat target (180^0).** 99
4.15 **Electron density distributions of a stagnation layer created on a 140^0 wedge target.** 99
4.16 **Electron density distributions of a stagnation layer created created on a 100^0 wedge target.** 99
4.17 **Electron density distributions of a stagnation layer created on a 80^0 wedge target.** 99
4.18 **Comparison of the peak density in a stagnation layer created by two 532 nm seeds and by two 1064 nm seeds as a function of wedge angle & time.** 100
4.19 **Opacity effects on the spatially integrated intensities of emitting ions in a stagnation layer (485 nm line) as a function of time for an 80^0 wedge target setup** 101
4.20 **Opacity effects on the spatially integrated intensities of emitting ions in a stagnation layer (492 nm line) as a function of time for an 80^0 wedge target setup** 101
4.21 **Time resolved broadband emission imaging of a reheated tin stagnation layer created on a wedge target acquired at times (a) 120 ns, (b) 150 ns, (c) 180 ns, (d) 210 ns, (e) 260 ns, (f) 290 ns, (g) 340 ns, (h) 390 ns, &(i) 440 ns. Images (a), (b) & (c) were acquired at an intensifier gain setting of 1500, (d) and (e) were acquired at a setting of 3000, and (f), (g), (h) & (i) were acquired at a setting of 4000. The interpulse delay was 120 ns.** . . 103
4.22 **Intensity trace of 485nm SnIII line in a stagnation layer generated by creating two seed plasmas with a 532 nm laser at a distance of 1.3 mm apart on a 140^0 wedge target as a function of time** 104
4.23 **Intensity trace of the same 485nm SnIII line in a stagnation layer which has been reheated 120 ns after seed initialisation using a 340 mJ 1064 nm laser pulse.** 104
4.24 **Spatially integrated intensities of the SnIII 485 nm line of a stagnation layer created using a 532 nm, 4 ns FWHM laser pulse on a 140^0 wedge target for various reheat times, as a function of time.** 105

4.25 **Spatially integrated intensities of the SnII 645 nm line of a stagnation layer created using a 532 nm, 4 ns FWHM duration laser pulse on a 140^0 wedge target for various reheat times, as a function of time.** . . . 105
4.26 **Spatially integrated intensities of the SnIII 485 nm line of a stagnation layer created using a 1064 nm, 6 ns laser pulse on a 140^0 wedge target for various reheat times, as a function of time.** 106
4.27 **Spatially integrated intensities of the SnII 645 nm line of a stagnation layer created using a 1064 nm, 6 ns laser pulse on a 140^0 wedge target for various reheat times, as a function of time.** 107
4.28 **Spatially & temporally integrated intensities of the SnIII 485 nm line of a stagnation layer created using different wavelengths for various reheat time delays.** . . . 108
4.29 **Spatially & temporally integrated intensities of the SnII 645 nm line of a stagnation layer created using different wavelengths for various reheat time delays.** . . . 109
4.30 **Spatially integrated intensities of the SnIII 485 nm line of a stagnation layer created using a 532 nm, 4 ns FWHM duration laser pulse on a 80^0 wedge target using various reheat times, as a function of time.** . . . 110
4.31 **Spatially integrated intensities of the SnIII 485 line of a stagnation layer created using a 1064 nm, 6 ns laser pulse on a 100^0 wedge target for various reheat times, as a function of time.** . . . 110
4.32 **Spatially integrated intensities of the SnIII 485 nm line of a stagnation layer created using a 1064 nm, 6 ns laser pulse on a 180^0 wedge target for various reheat times, as a function of time.** 111
4.33 **Spatially integrated intensities of the SnII 645 nm line of a stagnation layer created using a 532 nm, 4 ns FWHM duration laser pulse on a 80^0 wedge target for various reheat times, as a function of time.** . . . 112
4.34 **Spatially integrated intensities of the SnII 645 nm line of a stagnation layer created using a 532 nm, 4 ns FWHM duration laser pulse on a 100^0 wedge target for various reheat times, as a function of time.** . . . 112
4.35 **Spatially integrated intensities of the SnII 645 line of a stagnation layer created using a 532 nm 4 ns FWHM duration laser pulse on a 180^0 wedge target using various reheat times, as a function of time.** . . . 114

4.36 **Spatially & temporally integrated intensities of the SnIII 485 nm line of a stagnation layer created using various target wedge angles for various reheat time delays.** 114
4.37 **Spatially & temporally integrated intensities of the SnII 645 nm line of a stagnation layer created using various target wedge angles for various reheat time delays.** 115
4.38 **Time resolved emission spectroscopy of a tin stagnation layer created on an 80^0 wedge target acquired at times (a)120 ns, (b)180 ns & (c)240 ns, without reheating, at times (d)120 ns, (e)180 ns & (f)240 ns with reheating interpulse delay of 80 ns, and at times (g)120 ns, (h)180 ns, &(i)240 ns with interpulse delay of 120 ns. All images were acquired at an intensifier gain setting of 2000, apart from (c) which was acquired at a setting of 3000.** 117

List of Publications

[1] N. Gambino, P. Hayden, D. Mascali, J. Costello, C. Fallon, P. Hough, P. Yeates, A. Anzalone, F. Musumeci, and S. Tudisco. Dynamics of colliding aluminium plasmas produced by laser ablation. *Applied Surface Science*, 272:69–75, MAY 1 2013.

[2] P. Hough, T. J. Kelly, C. Fallon, C. McLoughlin, P. Hayden, E. T. Kennedy, J. P. Mosnier, S. S. Harilal, and J. T. Costello. Enhanced shock wave detection sensitivity for laser-produced plasmas in low pressure ambient gases using interferometry. *Measurement Science & Technology*, 23(12), DEC 2012.

[3] P. Yeates, C. Fallon, E. T. Kennedy, and J. T. Costello. Charge resolved electrostatic diagnostic of colliding copper laser plasma plumes. *Physics Of Plasmas*, 18(10), OCT 2011.

[4] P. Hough, P. Hayden, C. Fallon, T. J. Kelly, C. McLoughin, P. Yeates, J. P. Mosnier, E. T. Kennedy, S. S. Harilal, and J. T. Costello. Ion emission in collisions between two laser-produced plasmas. *Journal Of Physics D-Applied Physics*, 44(35), SEP 7 2011.

Nomenclature

List Of Acronyms

CCD Charge Coupled Device, page 36

CE Coronal Equilibrium, page 15

CRE Collisional Radiative Equilibrium, page 15

CT Complete Thermodynamic Equilibrium, page 14

$DP-LIBS$ Dual-Pulse Laser Induced Breakdown Spectroscopy, page vii

EUV Extreme Ultraviolet, page viii

$FWHM$ Full Width Half Maximum, page 42

IB inverse bremsstrahlung, page 5

$ICCD$ Intensified Charge Coupled Device, page 35

$LIBS$ Laser Induced Breakdown Spectroscopy, page viii

LOD Limit Of Detection, page viii

LPP Laser Produced Plasma, page 4

LTE Local Thermodynamic Equilibrium, page 15

MFP mean free path, page 19

MPI multi photon ionisation, page 6

$Nd:YAG$ yttrium aluminium garnet doped with neodymium ions, page 29

PIC particle in cell, page 1

PLD Pulsed Laser Deposition, page 2

SL Stagnation Layer, page 2

USB Universal Serial Bus, page 36

SBR signal to background ratio, page 13

VUV Vacuum Ultra Violet, page 123

List Of Symbols

χ_z ionisation potential, page 16

ℓ_{min} minimum impact parameter, page 6

ϵ_0 the permitivity of free space, page 3

γ angle of wedge prism in radians, page 32

λ incident wavelength, page 17

λ_{ii} ion-ion mean free path, page 19

ω_L frequency of laser pulse radiation, page 6

ζ collisionality parameter, page 19

A_{ab}, A_1, A_2 oscillator strength of transition, page 44

A_i ion broadening parameter, page 43

c speed of light in vacuum, page 6

D separation between seeds, page 19

e electron charge, page 3

g_a, g_b statistical weights of states labelled a and b, page 15

I laser irradiance, page 17

k_b Boltzmann's constant, page 3

L geometrical size of the plasma, page 3

$ln\Lambda$ the Coulomb logarithm, page 6

n_e electron density, page 3

n_z density of ions of charge z, page 3

n_c critical density, page 6

N_D number of particles within the Debye sphere, page 3

T plasma temperature, page 3

w electron-impact parameter, page 43

w_G Gaussian width, page 47

w_L Lorentzian width, page 47

Z Atomic number, page 17

z the degree of ionisation of the ions in a plasma, page 6

$\alpha_r(z+1, T_e)$ radiative recombination coefficient, page 16

$\alpha_{3b}(z+1, T_e)$ three-body recombination coefficient, page 16

λ_D Debye length, page 3

ω_p plasma frequency, page 3

E_a, E_b energy levels of states labelled a and b, page 15

m_e electron mass, page 3

N_a, N_b populations of states labelled a and b, page 15

$S(z, T_e)$ collisional ionisation coefficient, page 16

K absorption coefficient, page 6

f focal length of lens, page 32

n refractive index, page 32

Conferences Attended

Oral Presentations:

1. EUV Facilities at the DCU Intense Laser-Matter Interactions Laboratory, Fallon, C, Hayden P., Costello, J.T., *UCD Atomic and Plasma Modelling Workshop*, April 12th to 14th, 2010.

2. Outline of Postgraduate Research undertaken by Colm Fallon at the NCPST, DCU, Fallon C, *DRHEA Graduate Education Plenary Conference,* April 29th, 2010.

Poster Presentations:

1. EUV Spectra of Highly Charged Ions in Laser Plasmas and EBITs, C Fallon, P Hayden, R Hutton, Y Zou & J T Costello, *3rd International PEARL Workshop, Dublin City University,* May 6 - 9 (2009)

2. EUV Spectra of Highly Charged High-Z Ions in Laser Plasmas & EBITS, C Fallon, P Hayden, M Andersson, R Hutton, Y Zou and J T Costello, *IOP in Ireland Spring Weekend Conference, Hodson Bay Hotel, Athlone,* March 26 - 28 (2010)

3. EUV Spectra of Highly Charged High-Z Ions in Laser Plasmas & EBITS, C Fallon, P Hayden, M Andersson, R Hutton, Y Zou and J T Costello, *37th EPS Conference on Plasma Physics, Dublin City University,* 21 - 25 June (2010)

4. Time resolved extreme ultraviolet spectra from laser-produced tin plasmas, P Hayden, C Fallon, E T Kennedy and J T Costello, *37th EPS Conference on Plasma Physics, Dublin City University,* 21 - 25 June (2010)

5. EUV Spectra of Highly Charged High-Z Ions in Laser Plasmas & EBITS, C Fallon, P Hayden, M Andersson, R Hutton, Y Zou and J T Costello, *ECAMP 10, Salamanca, Spain* July 4 - 9 (2010)

6. EUV Spectra of Highly Charged High-Z Ions in Laser Plasmas & EBITS, C Fallon, P Hayden, R Hutton, Y Zou and J T Costello, *14th HCI, Shanghai, China,* August 30 - September 3, (2010)

7. Time and Space Resolved Optical Plasma Diagnostics of Table-Top Scale Laser Produced Tin Plasmas, C. Fallon, P. Hayden, E. T. Kennedy, T. Cummins, P. Dunne, C. O'Gorman, E. Sokell and J. T. Costello, *EUV Litho - International Workshop on Extreme Ultraviolet Sources, University College Dublin,* November 13 - 15 (2010)

8. Time Resolved EUV Emission Spectra of Table-Top Scale Laser Produced Tin Plasmas, P Hayden, C Fallon, E T Kennedy, P Dunne, G O'Sullivan and J T Costello, *EUV Litho - International Workshop on Extreme Ultraviolet Sources,* University College Dublin, November 13 - 15 (2010)

9. Investigation of colliding plasma plumes generated from thick and thin targets via laser ablation, N. Gambino, C. Fallon, P. Hayden, P. Yeates,

A. Anzalone, J. T. Costello, S. Gammino, L. Gizzi, T. Levato, D. Mascali, F. Musumeci and S.Tudisco, *38th Conference on Plasma Physics, Strasbourg,* 27th June to 1st July 2011

10. Time Resolved EUV Spectra of Laser Produced Tin Plasmas, P Hayden, C Fallon, E T Kennedy and J T Costello, *1st Intense-field Short Wavelength Atomic and Molecular Processes (I-SWAMP 2011), ICPEAC XXVII Satellite, Dublin,* July 21 - 23 (2011)

11. EUV Spectra Of Highly Charged Tungsten Ions in Laser Plasmas, Fallon, C, Hayden P., Hutton R., Zou, Y., Costello, J.T., *Intense field-Short Wavelength Atomic and Molecular Processes, Official Satellite workshop of the 27th International Conference on Photonic, Electronic and Atomic Collisions (ICPEAC2011),* July 21-23, 2011.

12. Time resolved EUV emission of laser produced tin plasmas - a source for EUVL, P Hayden, J Witz, C Fallon, E T Kennedy, P Dunne, G O'Sullivan and J T Costello, *Photonics Ireland 2011, Malahide, Dublin,* September 7-9 (2011)

13. Time and Space Resolved Optical Plasma Diagnostics of Table-Top Scale Laser Produced Tin Plasmas, C Fallon, P Hayden, T Cummins, C O Gorman, E Sokell, G O Sullivan & JT Costello, *COST Action MP0601, Short Wavelength Laboratory Sources, Final Meeting, UCD,* May 30th to 31st, 2011.

14. Time and Space Resolved Optical Plasma Diagnostics of Table-Top Scale Laser Produced Tin Plasmas, C Fallon, P Hayden, T Cummins, C O Gorman, E Sokell, G O Sullivan & JT Costello, *AMIG Spring Meeting 2013, NUI, Maynooth,* March 20th to 21st, 2013.